Morphological Design of Semiconductors During Molecular-Beam Epitaxy and Pulsed-Laser Deposition

by

Davide Del Gaudio

A dissertation submitted in partial fulfillment
of the requirements for the degree of
Doctor of Philosophy
(Materials Science and Engineering)
in the University of Michigan
2020

Doctoral Committee:

Professor Rachel S. Goldman, co-chair
Assistant Professor John T. Heron, co-chair
Professor Roy Clarke
Associate Professor Emmanouil Kioupakis
Professor Robert Ziff

Davide Del Gaudio

ddelgaud@umich.edu

ORCID iD: 0000-0002-0642-0941

Acknowledgements

I would like to thank my advisor, Prof. Rachel Goldman, and my co-advisor, Prof. John Heron, for their support throughout my studies at the University of Michigan, as well as Profs. Roy Clarke, Emmanouil Kioupakis, and Robert Ziff, for their time and guidance as members of my committee.

I would like to thank Prof. Ilan Shalish for his brilliant tutorials on nano-wire growth, Prof. Katsuyo Thornton for her very helpful discussions and suggestions, Prof. Liang Qi for his illuminating tutorial on pair correlation analysis, Dr. Larry Aagesen for his incredibly helpful lessons on phase-field modeling.

I would like to warmly thank the $(MC)^2$ staff for their teaching, mentoring, and mentoring.

I would like to thank Dr. Simon Huang for his patient mentoring, as well as Dr. Jordan Occeña, Dr. Mike Warren, Dr. Sunyeol Jeon, Dr. Myungkoo Kang, Dr. Tim Jen, Dr. Richard Field, Dr. Jenna Walrath, Dr. Tim Chambers.

I would like to thank for the help in my research tasks from Dr. Carl Boone, Tim Johnson, Sneha Yarlagadda, Jim Delaney, Erica Mason, Benjamin Serratos, and Kaitlyn Sallans.

I would like to thank for their friendship and support Caleb Reese, Chris Greenhill, Dr. Juan Lopez, Elaina Reese, Dr. Avi Bregman, Peter Meisenheimer, Steve Novakov, Nguyen Vu, Sieun Chae, Hongling Lu, Julia Trombley, Betty Thomas, Brandi Wooten, Larissa Woryk, Gnendy Indig, Lauren Tatarsky, Allison Sliter, Julien Baker, Margret Wander, George Clarke, and Stefan Babcock. Couldn't have done it without any of you, truly.

I gratefully acknowledge support from the National Science Foundation under Grant Nos. 1610362 and 1507033, the United States – Israel Binational Science Foundation under Grant No. 2015700, the Center for Solar and Thermal Energy Conversion, an Energy Frontier Research Center funded by the U.S. Department of Energy, Office of Science, Basic Energy Sciences, under Award No. DE-SC0000957. I also gratefully acknowledge support from the University of Michigan College of Engineering and CEW+.

Table of Contents

List of Figures

List of Tables

List of Appendices

Abstract

Low-dimensional semiconductors exhibiting quantum confinement are promising for enhanced efficiency in energy-conversion devices, including photovoltaics, thermoelectrics, and light-emission devices. For example, quantum dots (QDs, 0D) and nanowires (NWs, 1D) are expected to exhibit sharp features in the electron density of states, which reduce losses due to carrier recombination and scattering. Additionally, ideal arrays of semiconductor nanostructures enable the formation of well-defined minibands that enhance light absorption. Although nanostructure arrays are often achieved using extrinsic patterning methods, these require multiple fabrication steps that introduce lattice defects. Recently, processes for the spontaneous formation and ordering of both QDs and NWs have emerged, but these are insufficiently mature for full integration into device manufacturing. Indeed, for molecular beam epitaxy (MBE) of InAs QD arrays, the influence of local surface curvature on semiconductor QD positioning after the nucleation stage, i.e. during MBE growth and coarsening, is not well understood. On the other hand, for pulsed-laser deposition (PLD) of In_2O_3:Sn, the relative roles of vapor-solid (VS) and vapor-liquid-solid (VLS) growth modes during the morphological transitions resulting in semiconductor NW formation remain controversial. In the first part of this thesis, we employ a combined experimental-computational approach to quantify the aligned positioning of MBE-grown InAs/(Al)GaAs QDs and the effect of local surface curvature on the evolution of the InAs layer. In the second part of this thesis, we investigate the role of plasma expansion on the VS-VLS growth mode transition during PLD of In_2O_3:Sn.

The influence of surface curvature on the placement of InAs quantum dots (QDs) on (Al)GaAs surfaces is examined using an experimental-computational approach. Using height profiles from atomic-force micrographs, we simulate QD deposition with a 2D phase field model, which describes the time evolution of the InAs layer driven by a chemical potential gradient. Both atomically flat and mounded surfaces, which contain elongated corrugations generated via a surface instability induced by the Ehrlich-Schwoebel barrier, are employed as templates for the subsequent deposition of InAs QDs. For flat surfaces, phase-field simulations result in QD densities comparable to experimental observations following MBE deposition. For mounded surfaces, the simulations reveal QDs preferentially positioned in regions of positive curvature (substrate valleys), e.g., at along the side of surface mounds, consistent with the anisotropic QD placement observed experimentally. We discuss the role of curvature-driven diffusion in the spontaneous ordering of QDs, demonstrating its effect on QD nucleation and placement. This substrate curvature-driven direction of QD placement offers a method for immediate in-plane QD crystals and is extendable to a wide range of groups III-V compounds systems.

Complex oxides such as ITO are widely utilized as transparent conductors in a variety of functional devices. Typically, In_2O_3:Sn fabricated by sputtering, which often requires additional annealing to achieve high transparency and conductivity. Using PLD, both high transparency and high conductivity In_2O_3:Sn has been achieved without annealing, using instead selected gas species and pressures. However, the relative roles of VS and VLS growth modes during morphological transitions remains controversial. Here, we report on PLD of In_2O_3:Sn in an inert-gas environment, identifying the role of plasma plume expansion in the selection of VLS vs. VS growth. For the lowest N_2 pressure, indium-tin droplet formation, followed by self-catalyzed VLS growth, is

observed. With increasing N_2 pressure, a transition from VLS to VS growth is apparent. We hypothesize that oxygen scattering at the lowest N_2 pressure induces a metal-rich plume which leads to metal droplet formation, followed by VLS growth. As the N_2 pressure is increased, the plasma-plume and its metal-rich core are compressed, resulting in a transition to VS growth. This tunable compression of the plasma-plume offers a route to morphological design of a wide range of functional complex oxide devices with tunable optical and electronic performance.

Chapter 1: Introduction

1.1 Overview

Due to the effects of quantum confinement of charge carriers along one or more spatial directions, low-dimensionality nanostructures such as quantum wells (2D), nanowires (1D) and quantum dots (0D) are the object of much interest for the design of enhanced energy conversion devices. Compared to their bulk-crystal counterparts, low-dimensional nanostructures offer unparalleled flexibility in tailoring the bandgap energy, absorption and emission spectrum, and charge carrier wavefunctions. This flexibility is owed to the possibility of precisely tuning the dimensionality, size, shape, composition, and doping of these nanoparticles.[1] In addition to the flexibility in designing nano-scale energy conversion elements, moreover, quantum confinement enables a wide range of charge carrier manipulation phenomena that can be exploited for energy conversion devices. To illustrate the wide variety of beneficial effects of nanostructured arrays in energy conversion devices, this chapter addresses two specific solid state devices: solar cells, and thermoelectrics.

For solar cells, bandgap engineering, achieved by controlling the size of the nanostructures, may be employed to extend the light capture to the entirety of the sunlight spectrum.[2,3,4] Additionally, the low-dimensionality of the nanostructures can be exploited to reduce phonon-mediated charger carrier recombination and enable a phenomenon known as "carrier multiplication," whereby the recombination of a high-energy excited carrier results in the excitation of multiple other carriers.[2,3,5,6,7] Ordered arrays of QDs can be used to form an additional intermediate band

within the bandgap thereby increasing light absorption by adding additional absorption wavelengths.[8]

For thermoelectrics, low-dimensionality nanostructures lead to enhanced electrical conduction due to the large peaks in the density of states (see Fig. 1.1),[9,10] while the energy barriers at the nanostructure/matrix interface can be engineered to select for electrical transport only the high-energy electrons that have a positive contribution to the thermoelectric power.[11,9] Additionally, the incorporated nanostructures feature complicated surfaces and interfaces with their matrices, which help reduce the thermal conductivity through the disruption of phonon transport.[11]

This chapter begins by describing the potential utility of low-dimensionality nanostructured systems for energy conversion devices such as solar cells and thermoelectrics, with a focus on ordered ensembles of 0D QDs and 1D NWs. Subsequently, the specific modes of formation and growth of the InAs/(Al)GaAs QDs and In_2O_3-SnO_2 NW discussed in this dissertation are introduced. The objectives of studying the physical mechanisms determining the spontaneous organization of InAs/(Al)GaAs QDs and the formation of In_2O_3-SnO_2 NWs during pulsed-laser deposition are introduced. The chapter concludes with an outline of the dissertation.

1.2 Organized nanostructures in energy conversion devices

This section gives a brief overview of two major classes of energy conversion devices for which low-dimensionality epitaxial nanostructures are promising active components due to their charge-carrier manipulation and band-engineering capabilities. First, solar cells are discussed, for which nanostructured arrays can enhance both light absorption and current generation. Secondly, thermoelectrics are discussed, for which nanostructured arrays can increase thermopower and reduce recombination losses.

1.2.1 Solar cells

Organized nanostructured arrays have been proposed for designing next generation high-efficiency single-junction solar cells that exceed the efficiency limit[12] of a traditional bulk-crystal single-junction of 30% by enabling the capture of photon energy over a broad spectral range, and a more efficient separation and collection of photo-generated charge carriers.[13,2]

For the extension of the spectral range of photon capture, QD arrays have been suggested as photo-active materials with tunable band-gaps due to the ability to tailor the QD diameter and/or composition, enabling easy fabrication of multi-junction "rainbow" solar cells.[2,14,15,16,17,18,19] However, the colloidal QDs proposed for these applications create problems such as reduced QD/matrix interface charge transfer due to surface trap states. Additionally, the spectrum extension of the photon capture in colloidal QD-sensitized solar cells still requires the design of multiple junctions, due to the necessity of balancing high light absorption (low bandgap) and high open circuit voltage (high bandgap) for the uniform QDs within a single junction solar cells.[2,20]

An alternative approach to enhance light absorption in a solar cell without the need for a multi-junction stack is generate an intermediate band (IB) within the band-gap, enabling the additional absorption of sub-bandgap photons and excitation of charge carriers from the valence band (VB) to the IB and from the IB to the conduction band (CB).[8] A promising way to achieve the formation of the IB is embedding a QD superlattice (QDSL) in a single junction solar cell. Figure 1.2 shows a schematic representation of the QDSL approach to the design of an IB solar cell. In Fig. 1.2(a), an isolated QD is shown with the corresponding ground state of a trapped electron. The electron states within neighboring QDs may experience superposition, as shown in Fig. 1.2(b).

If the QDSL is both highly dense and ordered, as in Fig. 1.2(c), an IB will form within the bandgap of the solar cell, enabling the absorption of sub-bandgap photons.[21,22,23]

However, to retain the maximum effective bandgap, and therefore maximum photon absorption, and to avoid thermal escape of the photogenerated charge carriers, the presence of additional energy levels between the IB and the CB must be avoided. For this purpose, a high density ($> 10^{12}$ cm^{-2}) of small uniform size (< 10 nm diameter), and spherical-shaped QDs is required.[2425] The objective of this dissertation is to examine the evolution of positioning of QDs on spontaneously nanopatterned substrates, studying the effect of local substrate curvature on QD alignment, to understand the mechanisms that can drive the formation of ordered QD arrays.

1.2.2 Thermoelectrics

Thermoelectric materials have the ability to convert thermal energy into electrical energy. In the current technological landscape, more than 80% of world-wide energy production is still fossil fuel-based.[26] Moreover, ≈70% of the fossil-fuel produced energy consumed is actually lost in the form of waste heat through exhaust gases and cooling systems.[27,28] It is therefore appealing to turn to thermoelectrics (TEs) as a noise-less, emission-less, fuel-less, and low-maintenance[29] option for waste heat-energy recovery, enabling at once improved energy efficiency for fossil fuels and an additional power supply. Widespread adoption of TEs is, however, limited by their relatively low efficiency.[30,31]

A commonly used quantity to characterize the usefulness of a thermoelectric material is its dimensionless thermoelectric figure of merit ZT, defined as:

$$ZT := \frac{S^2 \sigma T}{\kappa}, \tag{1.1}$$

where S is the Seebeck coefficient, σ is the electrical conductivity, T is the temperature, and κ is the thermal conductivity.[11,32] It can be shown, that the efficiency of a thermoelectric device depends only on the temperature differential on which it operates and on ZT, and it approaches the Carnot limit for $ZT \gg 1$.[32]

For bulk metals, however, the electrical (σ) and thermal (κ) conductivity are related by the Wiedeman-Franz law, which states that their ratio is proportional to the temperature T:

$$\frac{\kappa}{\sigma} = L(T)T, \tag{1.2}$$

where $L(T)$ is the "Lorenz number."[33,34] Looking back at the figure of merit $ZT = \frac{S^2\sigma T}{\kappa}$ in Eq. (1.1), it is evident thus that controlling S, σ and κ independently poses a significant challenge that cannot be easily overcome in conventional bulk conductors, where thermal conductivity is largely determined by electron transport.[11,32] For semiconductors, on the other hand, the Wiedeman-Franz law does not apply, as the contribution of the lattice vibrations to the thermal conductivity is larger than that of electrons. Semiconductors appear thus to be preferable candidates for thermoelectrics, provided that the mean free path of phonons is minimized.[32]

To improve the efficiency of thermoelectrics, the application of materials engineering is therefore in any case needed, both to reduce thermal conductivity and to enhance electronic transport. Initial approaches concentrated on synthesizing specialized materials with reduced lattice thermal conductivity such as Bi_2Te_3-based alloys[11] consisting of covalently-bonded planes weakly bonded by van der Waals forces along the c-axis,[32] or $CoSb_3$-based alloys[11] containing interstitial sites that can host loosely bonded heavy elements ("rattlers").[32] On the other hand, increasing interest has been directed at exploiting the low-dimensionality of nanostructured materials to obtain enhanced power factors by improving electron conduction.[35,36,37,38,39] High ($\gtrsim 1$) ZT

has in fact been predicted for nanostructured materials such as 2D films super-lattices,[11,37,39] quantum dots super-lattices,[11,35,36] and nanowires.[11,39]

The high performance of nanostructures based TEs has however not been yet demonstrated experimentally because of the complexity, low yield, and high cost of the production techniques involved.[27] For NW, e.g., issues of reliability of electrical contact, structural integrity, and wire alignment are common.[35,40] Simple bottom-up synthesis approaches to the growth and self-organization of two nanostructured thermoelectric materials are thus needed. The objective of this dissertation is to examine the physical mechanisms of formation of nanostructured arrays, namely, of 0D QDs and 1D NWs.

1.3 Synthesis of 0D and 1D nanostructures

In this section, the growth modes of InAs/(Al)GaAs QD and In_2O_3-SnO_2 NWs studied in this dissertation are briefly introduced to aid in the subsequent discussion of the research into the details of formation of these nanostructured arrays.

1.3.1 Stranski-Krastanov quantum dots growth

The Stranski-Krastanov (SK) transition is a common method for synthesizing 0D QDs in semiconductor materials systems, due to its capability of generating coherent nanocrystalline QDs. The SK transition is strain-driven and consists of a transition from layer-by-layer growth to the formation of raised nm-scale structures (the QDs).

The resulting morphology when depositing material A on material B depends on the relative amounts of the surface energy densities γ_{A} and γ_{B}, and interfacial energy density γ^*. Flat, layer-by-layer growth, also called Frank-van der Merwe growth mode, takes place when $\gamma_{\mathrm{A}} +$

$\gamma^* < \gamma_B$, in other words, when it is energetically favorable to cover any exposed B surface. Conversely, islands growth, also called Volmer-Weber growth mode, takes place when $\gamma_A + \gamma^* > \gamma_B$.[41]

For the SK growth mode, which consists first of a few layers of layer-by-layer growth followed by the formation of islands, the switch is caused by the thickness dependence of γ^*. During the formation of the first energetically favored layers, the interfacial energy density γ^* increases due to the accumulating strain energy caused by the misfit between A and B, until the "nucleation barrier" is crossed from $\gamma_A + \gamma^* < \gamma_B$ to $\gamma_A + \gamma^* > \gamma_B$ and islands start to form.[41]

The resulting morphology is a series of 3D islands, the QDs, surrounded by a thin 2D layer termed "wetting layer." The critical thickness t_c at which the formation of 3D islands becomes thermodynamically favored and the growth mode transition is induced is dependent on the material system and the temperature but can be measured experimentally.[42]

Figure 1.3 shows a schematic representation of the evolution of the energy of the epilayer, and the corresponding morphological evolution, of the epilayer during the SK transition. Before reaching the critical thickness, the growth proceeds in a 2D layer-by-layer mode. Upon reaching the critical thickness, the SK transition is onset and the QDs nucleate. Following nucleation, the growth of the QDs proceeds.

1.3.2 Vapor-liquid-solid nano-wires growth

For the synthesis of 1D NW, a commonly employed method is the growth mode commonly known as "vapor-liquid-solid" (VLS), whereby liquid metal droplets act as a catalyst for the precipitation of the compound at the base of the droplets, inducing the growth of high-aspect ratio stems with metal droplets at their tips (the VLS NW).

The VLS growth mode of NW was first described in the case of silicon NW grown with the aid of gold catalyst droplets.[43] However, the inclusion of an external metal catalyst, however, causes the contamination of the NW crystal and issues like impurities, crystal defects, and unintentional doping.[44,45] An alternative to using an external catalyst is to exploit a "self-catalyzed" growth mechanism, for metal-based compounds, whereby the metal(s) included in the compound form the seed droplets needed for VLS growth.

Figure 1.4 shows a schematic representation of the evolution of self-catalyzed VLS metal-oxide (MO) NW. First, the metal condenses in a seed droplet. With continued deposition, oxygen is absorbed into the M droplet until supersaturation is reached, inducing the precipitation of MO, i.e. nucleation of MO nano-crystal. The MO nanocrystals deposit at the base of the droplet. With continued supply of M and oxygen, the continuous precipitation of crystalline MO at the base of the droplet results in the growth of the NW stem, while the metal droplet stays at the tip of the NW.

1.4 Objectives of the dissertation

As outlined in Ch. 1.1, nanostructure arrays are promising for increased performance of a wide range of energy-conversion semiconductor devices. In this dissertation, we focus on two types of nanostructure arrays: chains of 0D QDs and arrays of 1D ITO NWs. The objective of this work is to study the mechanisms governing the spontaneous in-plane organization of the InAs QDs on corrugated (Al)GaAs surfaces and the deposition kinetics which determine the selection of VLS growth ITO NW vs. the vapor-solid (VS) growth of ITO films. Indeed, as both SK and VLS growth modes are in principle random processes, e.g. regarding the placement of the QD nuclei and of the NW seeds, we seek to understand the physical processes that can induce a regular organization of these processes, bridging the gap towards highly ordered, but labor-intensive and defect-inducing

lithography methods. In other words, how do we exploit the "spontaneous" qualities of these processes without suffering from their "random" qualities?

For the QDs, we use molecular-beam epitaxy (MBE) to synthesize (Al)GaAs surfaces that are either kept flat or intentionally nano-patterned exploiting a growth instability[46] that results in elongated surface structures termed "mounds." AlGaAs, with its larger bandgap than GaAs, is considered a promising matrix material for IBSC. A high photocurrent while preserving open-circuit voltage has been predicted for InAs/AlGaAs QD-based IBSC.[47,48] Additionally, suppression of charge carrier recombination has been demonstrated for InAs/AlGaAs QD-based IBSC.[49] The QD growth on flat and mounded surfaces is then both performed via MBE and simulated using a phase-field model (PFM). We present the first PFM QD growth simulation on real, experimentally measured surfaces. This combined experimental-computational approach permits the study of the influence of the local curvature on the evolution of the position of the QDs during growth and the eventual experimentally observed aggregation of those QDs in chains along the sides of the elongated surface mounds. We show that by accessing larger local surface curvatures by generating surface mounds, the curvature-driven diffusion to align quantum dots in chains is exploited. These findings provide insights into the influence of surface structuring on the positioning of QDs following nucleation, which may be utilized immediate first-layer ordering of QDs on a variety of nano-patterned semiconductor surfaces.

For the ITO NW, we use pulsed-laser deposition (PLD) to obtain poly-crystalline ITO films, VLS ITO NW, and mixed VLS NW and polycrystalline film layers. We examine the role of the expansion of the ITO plasma during PLD in the selection of VLS vs. VS growth of ITO and we formulate a kinetic model that explains the surprising formation of InSn droplets, necessary for self-catalyzed ITO growth, during the ablation of oxygen-rich source material. Indeed, with this

model we connect two phenomena previously unrelated in literature: the expansion-driven stoichiometric imbalance of the plasma, and the until now unexplained formation of VLS nanowires during PLD. This tunable compression of the plasma-plume uses an insight into the plasma kinetics of pulsed laser deposition to offer a route to the rational morphological design of a wide range of functional complex oxides with tunable optoelectronic performance.

1.5 Outline of the dissertation

In this chapter, we described the potential for nanostructured arrays in semiconductor devices, introduced the nanostructures that are the focus of this thesis (QDs and NWs), along with their mechanisms of formation, and outlined the physical phenomena inherent to the formation and evolution of these nanostructures that were addressed during the research work presented in this dissertation. Chapter 2 describes the deposition techniques employed for the growth of the nanostructures studied, as well as the various microscopy and spectroscopy tools employed.

Chapter 3 describes the study of the influence of surface curvature of the (Al)GaAs surfaces on the alignment of the InAs QD arrays, and includes a detailed description of the PFM model used for the simulation of the InAs growth. The work described in Chapter 3 was peer-reviewed and published in D. Del Gaudio, L.K. Aagesen, S. Huang, T.M. Johnson, B.D. Faeth, H. Lu, R.M. Ziff, and R.S. Goldman, "Influence of surface nano-patterning on the placement of InAs quantum dots" Journal of Applied Physics **124**, 115307 (2018). Chapter 4 describes the study of the influence of plasma expansion on the selection of VLS vs. VS growth of ITO layers during PLD. The work described in Chapter 4 was peer-reviewed and published in D. Del Gaudio, C.T. Boone, K. Sallans, E. Mason, A.J. Williamson, S. Yarlagadda, Y. Turkulets, J.T. Heron, I. Shalish, and R.S. Goldman, "Morphological design of complex oxides during pulsed-laser deposition: The role of

plasma-plume expansion" Journal of Applied Physics **126**, 184301 (2019). Chapter 5 briefly summarizes the results described in Chs. 3 and 4, shows some preliminary observations made during this work, and contains some suggestions for possible future inquiry, based on preliminary observations and open questions encountered in this work.

This dissertation concludes with a series of appendices containing detailed descriptions of some experimental methods employed in the research described here. Appendix A contains the complete computer code employed for various computations described throughout the dissertation. Appendix B contains a description of the experimental methods developed to measure the electronic transport characteristics of a single NW. Appendix C contains a detailed table listing all the samples prepared during this research work, with the relevant growth conditions.

1.6 Figures

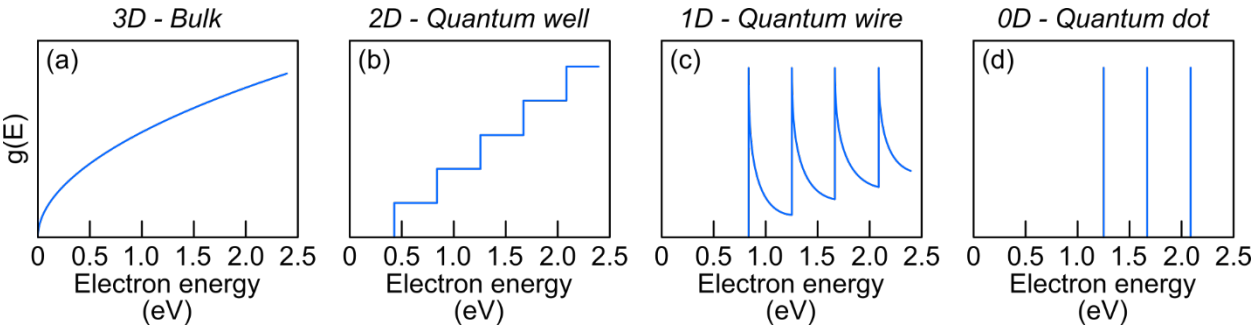

Figure 1.1: electron density of states g as a function of electron energy E for (a) a 3D bulk crystal, (b) a 2D quantum well, (c) a 1D quantum wire, and (d) a 0D quantum dot. The density of states for quantum wires and quantum dots comprises a series of sharp peaks, which may be exploited for enhancing the Seebeck coefficient S.

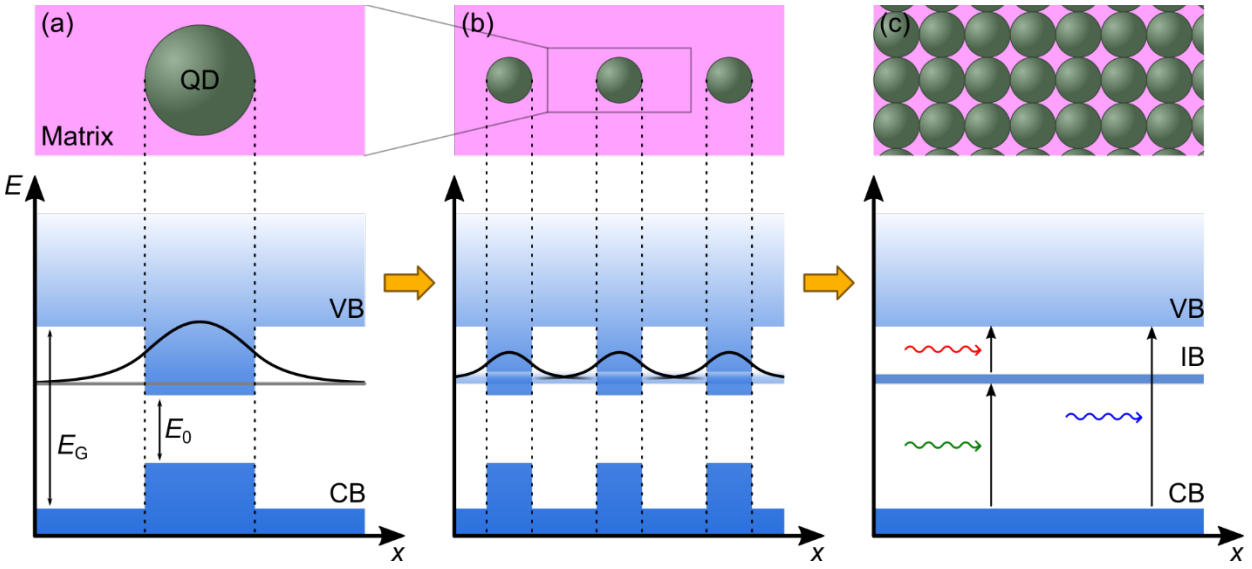

Figure 1.2: schematic representation of the QD superlattice approach to intermediate band solar cells. **(a)** energy well generated by a single QD and corresponding ground state of a trapped electron. **(b)** electron states from neighboring QDs experience superposition. **(c)** a high density regular QD superlattice forms an intermediate band that enables absorption of sub-bandgap photons.

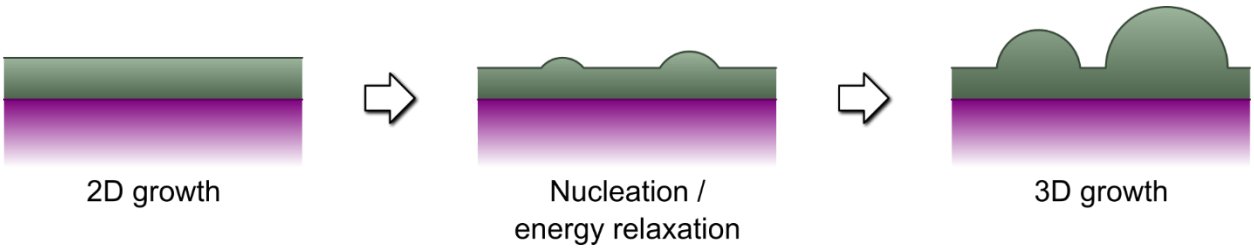

Figure 1.3: schematic representation of the evolution of the morphology of epilayers during the Stranski-Krastanov 2D–3D growth mode transition for heteroepitaxy of mismatched epi-layers in time.

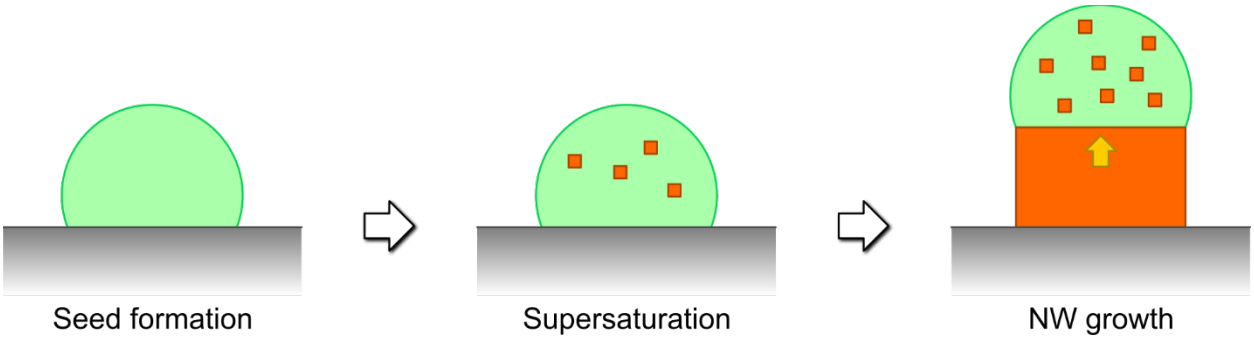

Figure 1.4: schematic representation of the evolution of the vapor-liquid-solid (VLS) growth mode of NW.

1.7 References

[1] A.M. Smith and S. Nie, "Semiconductor nanocrystals: Structure, properties, and band gap engineering" Acc. Chem. Res. **43**, 190 (2010).

[2] G. Chen, J. Seo, C. Yang, and P.N. Prasad, "Nanochemistry and nanomaterials for photovoltaics" Chem. Soc. Rev. **42**, 8304 (2013).

[3] A.M. Smith and S. Nie, "Bright and compact alloyed quantum dots with broadly tunable near-infrared absorption and fluorescence spectra through mercury cation exchange" J. Am. Chem. Soc. **133**, 24 (2011).

[4] E.H. Sargent, "Infrared quantum dots" Adv. Mater. **17**, 515 (2005).

[5] J.W. Luo, A. Franceschetti, and A. Zunger, "Carrier multiplication in semiconductor nanocrystals: theoretical screening of candidate materials based on band-structure effects" Nano Lett. **8**, 3174 (2008).

[6] V.I. Klimov, "Spectral and Dynamical Properties of Multiexcitons in Semiconductor Nanocrystals" Annu. Rev. Phys. Chem. **58**, 635 (2007).

[7] V.I. Klimov, A.A. Mikhailovsky, D.W. McBranch, C.A. Leatherdale, and M.G. Bawendi, "Quantization of multiparticle Auger rates in semiconductor quantum dots" Science **287**, 1011 (2000).

[8] A. Luque and A. Martí, "Increasing the Efficiency of Ideal Solar Cells by Photon Induced Transitions at Intermediate Levels" Phys. Rev. Lett. **78**, 5014 (1997).

[9] J.P. Heremans, "Low-Dimensional Thermoelectricity" Acta Phys. Pol. A **108**, 609 (2005).

[10] M. Cutler and N.F. Mott, "Observation of Anderson Localization in an Electron Gas" Phys. Rev. **181**, 1336 (1969).

[11] M.S. Dresselhaus, G. Chen, M.Y. Tang, R. Yang, H. Lee, D. Wang, Z. Ren, J.-P. Fleurial, and P. Gogna, "New directions for low-dimensional thermoelectric materials" Adv. Mater. **19**, 1043 (2007).

[12] W. Shockley and H.J. Queisser, "Detailed balance limit of efficiency of p-n junction solar cells" J. Appl. Phys. **32**, 510 (1961).

[13] F. Priolo, T. Gregorkiewicz, M. Galli, and T.F. Krauss, "Silicon nanostructures for photonics and photovoltaics" Nat. Nanotechnol. **9**, 19 (2014).

[14] R.S. Selinsky, Q. Ding, M.S. Faber, J.C. Wright, and S. Jin, "Quantum dot nanoscale heterostructures for solar energy conversion" Chem. Soc. Rev. **42**, 2963 (2013).

[15] A.M. Smith and S. Nie, "Bright and compact alloyed quantum dots with broadly tunable near-infrared absorption and fluorescence spectra through mercury cation exchange" J. Am. Chem. Soc. **133**, 24 (2011).

[16] E. Cassette, T. Pons, C. Bouet, M. Helle, L. Bezdetnaya, F. Marchal, and B. Dubertret, "Synthesis and characterization of near-infrared Cu-In-Se/ZnS core/shell quantum dots for in vivo imaging" Chem. Mater. **22**, 6117 (2010).

[17] Y. Yin and A.P. Alivisatos, "Colloidal nanocrystal synthesis and the organic–inorganic interface" Nature **437**, 664 (2005).

[18] E.H. Sargent, "Infrared quantum dots" Adv. Mater. **17**, 515 (2005).

[19] X. Peng, L. Manna, W. Yang, J. Wickham, E. Scher, A. Kadavanich, and A.P. Alivisatos, "Shape control of CdSe nanocrystals" Nature **404**, 59 (2000).

[20] J. Tang and E.H. Sargent, "Infrared colloidal quantum dots for photovoltaics: Fundamentals and recent progress" Adv. Mater. **23**, 12 (2011).

[21] R.P. Raffaelle, S.L. Castro, A.F. Hepp, and S.G. Bailey, "Quantum dot solar cells" Prog. Photovoltaics Res. Appl. **10**, 433 (2002).

[22] A. Martí, L. Cuadra, and A. Luque, "Partial filling of a quantum dot intermediate band for solar cells" IEEE Trans. Electron Devices **48**, 2394 (2001).

[23] M.A. Green, "Potential for low dimensional structures in photovoltaics" Mater. Sci. Eng. B Solid-State Mater. Adv. Technol. **74**, 118 (2000).

[24] A. Mellor, A. Luque, I. Tobías, and A. Martí, "A numerical study into the influence of quantum dot size on the sub-bandgap interband photocurrent in intermediate band solar cells" AIP Adv. **3**, (2013).

[25] A. Luque, A. Martí, E. Antolín, and C. Tablero, "Intermediate bands versus levels in non-radiative recombination" Phys. B Condens. Matter **382**, 320 (2006).

[26] United Nations Department of Economic and Social Affairs, Statistics Division. Energy Production Dashboard. Retrieved October 19, 2019.

[27] L. Yang, Z.-G. Chen, M.S. Dargusch, and J. Zou, "High Performance Thermoelectric Materials: Progress and Their Applications" Adv. Energy Mater. **8**, 1701797 (2018).

[28] K. Koumoto, I. Terasaki, and R. Funahashi, "Complex Oxide Materials for Potential Thermoelectric Applications" MRS Bull. **31**, 206 (2006).

[29] T. Zhu, Y. Liu, C. Fu, J.P. Heremans, J.G. Snyder, X. Zhao, "Compromise and Synergy in High-Efficiency Thermoelectric Materials" Adv. Mater. **29**, 1605884 (2017).

[30] Z.G. Chen, G. Han, L. Yang, L. Cheng, J. Zou, "Nanostructured thermoelectric materials: Current research and future challenge" Prog. Nat. Sci. **22**, 535 (2012).

[31] C. Gayner, K.K. Kar, "High Performance Thermoelectric Materials: Progress and Their Applications" Prog. Mater. Sci. **83**, 330 (2016).

[32] H. J. Goldsmid "Introduction to Thermoelectricity" 2nd ed. Springer (2016)

[33] N. W. Ashcroft, N. D. Mermin, "Solid State Physics" Harcourt College Publishers (1976)

[34] C. Kittel, "Introduction to Solid State Physics" 8th ed. Wiley (2005)

[35] A. Yadav, K.P. Pipe, W. Ye, and R.S. Goldman, "Thermoelectric properties of quantum dot chains" J. Appl. Phys. **105**, (2009).

[36] T. C. Harman, P. J. Taylor, M. P. Walsh, and B. E. LaForge, "Quantum Dot Superlattice Thermoelectric Materials and Devices" Science 297, 2229 (2002).

[37] L. D. Hicks, T. C. Harman, X. Sun, and M. S. Dresselhaus, "Experimental study of the effect of quantum-well structures on the thermoelectric figure of merit" Phys. Rev. B 53, R10493 (1996)

[38] D. A. Broido and T. L. Reinecke, "Effect of superlattice structure on the thermoelectric figure of merit" Phys. Rev. B 51, 13797 (1995)

[39] D. A. Broido and T. L. Reinecke, "Theory of thermoelectric power factor in quantum well and quantum wire superlattices" Phys. Rev. B 64, 045324 (2001)

[40] A. R. Abramson, W. C. Kim, S. T. Huxtable, Y. Haoquan, W. Yiying, A. Majumdar, C. L. Tien, and P. Yang, "Fabrication and characterization of a nanowire/polymer-based nanocomposite for a prototype thermoelectric device" J. Microelectromech. Syst. 13, 505 (2004).

[41] J.A. Venables, "Surface processes in epitaxial growth" in *Introduction to Surface and Thin Film Processes*, Cambridge University Press (2001).

[42] W. Seifert, N. Carlsson, M. Miller, M.-E. Pistol, L. Samuelson, and L.R. Wallenberg, Prog. Cryst. Growth Charact. Mater. **33**, 423 (1996).

[43] R.S. Wagner and W.C. Ellis, "Vapor-liquid-solid mechanism of single crystal growth" Appl. Phys. Lett. **4**, 89 (1964).

[44] A. Bailly, O. Renault, N. Barrett, L.F. Zagonel, P. Gentile, N. Pauc, F. Dhalluin, T. Baron, A. Chabli, J.C. Cezar, and N.B. Brookes, "Direct Quantification of Gold along a Single Si Nanowire" Nano Lett. **8**, 3710 (2008).

[45] E. Koren, G. Elias, A. Boag, E.R. Hemesath, L.J. Lauhon, and Y. Rosenwaks, "Direct Measurement of Individual Deep Traps in Single Silicon Nanowires" Nano Lett. **11**, 2499 (2011).

[46] C. Orme, M.D. Johnson, J.L. Sudijono, K.T. Leung, and B.G. Orr, "Large scale surface structure formed during GaAs (001) homoepitaxy" Appl. Phys. Lett. **64**, 860 (1994).

[47] G. Wei and S.R. Forrest, "Intermediate-Band Solar Cells Employing Quantum Dots Embedded in an Energy Fence Barrier" Nano Lett. 7, 218 (2007).

[48] P.G. Linares, A. Martí, E. Antolín, and A. Luque, "III-V compound semiconductor screening for implementing quantum dot intermediate band solar cells" J. Appl. Phys. 109, (2011).

[49] Í. Ramiro, J. Villa, P. Lam, S. Hatch, J. Wu, E. López, E. Antolín, H. Liu, A. Martí, and A. Luque, "Wide-Bandgap InAs/InGaP Quantum-Dot Intermediate Band Solar Cells" IEEE J. Photovoltaics **5**, 840 (2015).

Chapter 2: Experimental Procedures

2.1 Overview

This chapter describes the experimental procedures employed to synthesize and characterize the quantum dots (QDs) and nanowires (NWs) studied in this work. The molecular-beam epitaxy (MBE) systems used for the QDs growth and the pulsed-laser deposition (PLD) system used for the NW growth are described. Subsequently, the characterization techniques employed in this work are described. Following growth, the QDs were examined by atomic-force microscopy (AFM), while the NWs were examined by scanning-electron microscopy (SEM) and x-ray diffraction (XRD). For the electrical transport characterization of the NW, a focused-ion beam (FIB) was used for both in-situ *I-V* single-NW measurements, and deposition of Pt contacts for ex-situ single-NW measurements circuits. Additional imaging and spectroscopy of the NW were performed in a scanning transmission-electron microscope (TEM) and in a confocal optical microscope.

2.2 Molecular-Beam Epitaxy

2.2.1 Overview

Molecular beam-epitaxy (MBE) is an ultra-high vacuum (UHV) based vapor deposition technique capable of synthesizing films with a high degree of control over composition and doping levels, and with impurity levels below ten parts per billion.[1] During MBE, solid or liquid source materials are heated in UHV so that their sublimation or evaporation generates molecular fluxes that travel through the chamber without scattering (molecular beams) before impinging upon a heated single-crystalline substrate to form crystalline films (epitaxy). The InAs QDs described in

Ch. 3 were deposited in a Riber Compact 21 (C21) MBE system, while additional AlGaAs buffer listed in Appx. D.1 were deposited in a Veeco GENII MBE system.

2.2.2 System details

2.2.2.1 Chambers, substrate exchanges, and vacuum operation

Both the C21 and GENII systems, shown in Figs. 2.1 and 2.2, respectively, comprise a central UHV chamber in which the deposition is performed (the "growth chamber"), connected to a load-lock ("intro") chamber and a buffer chamber, used for air-vacuum substrate exchange and in-vacuum substrate transfer, respectively. The substrates are mounted on molybdenum blocks ("moly-blocks") and loaded onto wheeled racks called "trolleys" before being transferred to the intro chamber. While in vacuum, the trolley runs on rails mounted to the bottom of the intro and buffer chambers and is moved with a chain connected to external knobs in the C21, or with magnets in the GENII. A single moly-block can be transferred from the trolley to the growth chamber with a linear magnetic transfer arm. The air-vacuum port of the intro chamber is a glass window mounted on a UHV flange, while the intro chamber and the buffer chamber, and the buffer chamber and the growth chamber are connected/sealed by two gate valves, which provide an openable seal with a rubber o-ring mounted on a sliding plate (the "gate").

To maintain UHV, the C21 GC is continuously pumped by a Riber ion pump and additionally features a Riber titanium sublimation pump, while the GENII GC is continuously pumped by a Varian ion pump and a CTI cryo-pump both. In addition to continuous pumping, both GCs contain two separate fluid vessels called "cryo-shroud" and "cryo-panel" which are filled with liquid nitrogen during deposition. The cryo-panel is positioned on the flange of the growth chamber to which the effusion cells are mounted and is responsible for the thermal insulation of the effusion

cells. The cryo-shroud, on the other hand, is positioned around and behind the substrate manipulator, close to the chamber walls, in order to reduce re-evaporation from the chamber walls and act as a condensation pump as well. The base pressure in both systems, with flowing liquid nitrogen, is below 5×10^{-9} Torr for the C21 and below 5×10^{-10} Torr for the GENII. The pressure of both chambers is monitored with an ion gauge installed on a port not in sight of the source material effusion cells.

2.2.2.2 Substrate manipulators

To ensure uniformity during growth, the substrate is mounted on a manipulator capable of continuous rotation, called ARM ("azimuthal rotation manipulator"), for the C21, or CAR ("continuous azimuthal rotation") for the GENII. The substrate is rotated around its normal-to-the-surface axis and the rotation speed chosen for the samples in this work was 10 rpm. Additionally, to control the temperature of the substrate, a heating filament and a thermocouple (TC) are installed on the manipulator directly behind the moly-block. To measure the beam equivalent pressure (BEP) of the source material fluxes, an ion gauge, termed the "beam-flux" (BF) gauge, is mounted on the manipulator on the opposite side of the block holder/heater. The manipulator can be flipped from growth position (substrate facing the sources) and BEP-measurement / transfer position (BF gauge facing the sources, block facing the GC-buffer valve.

For growth rate calibration and growth monitoring, both C21 and GENII growth chambers are equipped with reflection high-energy electron diffraction (RHEED) systems, whose setup and use are described in Sec. 2.2.3.

2.2.2.3 Material sources

For the deposition source material, several effusion cells are installed on the "main flange" of the growth chamber, facing the substrate. For this work, solid or liquid source materials housed

in crucibles were used. While arsenic (99.99995%) and silicon (99.9999%) are kept solid and their deposition is accomplished with sublimation, gallium (99.99999%), aluminum (99.99995%), and indium (99.99999%) are kept liquid and evaporated for deposition. With the only exception of arsenic, the elements are contained in pyrolithic boron nitride (pBN, a high temperature-resistant ceramic) crucible-based effusion cells called "K-cells." Arsenic is contained in a "valved cracking effusion cell," described later on. All effusion cells are equipped with a computer-operate physical shutter for precise and rapid initiation and cessation of the deposition of the single element.

The pBN crucibles containing Ga, Al, In, and Si are cone-shaped with a lip around the aperture of the cone where the crucible is placed on the effusion cell. Most effusion cells have a heating filament surrounding the crucible and a thermocouple placed in close proximity of the bottom of the crucible. The cell containing Ga in the C21 has two sets of heating filament and thermocouple, one around the bottom of the crucible, for bulk temperature control, and one around the lip of the crucible, to prevent condensation of Ga droplets on the crucible lip. The material flux is therefore controlled by setting a temperature for the base/bulk of the crucible containing the source material.

The flux density J of the material emitted by the effusion K-cell, measured in molecules $cm^{-2}s^{-1}$, is:[1]

$$J = 4.62 \times 10^{22} \frac{p\, r^2}{L^2 \sqrt{M\, T}}, \tag{2.1}$$

where p is the vapor pressure inside the crucible in mbar, r is the aperture radius of the crucible, L is the distance between the crucible and the substrate, M is the molecular weight of the source material, and T the temperature of the crucible. It is important to note that, while J has a direct $T^{-1/2}$ dependence on T, $p \propto e^{T}$, resulting in an overall quasi-exponential dependence of the flux on crucible temperature.[1]

For the sublimation of arsenic, since the spontaneous sublimate of solid As is As_4 tetramers, a two-stages valved cracking effusion cell is employed. The solid As is placed in a heated perforated stainless steel reservoir called the "bulk zone." The sublimated As_4 passes from the bulk zone, through a pBN valve, to the second heated stage of the cell, the "cracking zone." The pBN valve seals the bulk zone of the As cell to help reduce the background pressure, due to the high vapor pressure of As, when the cell is not in use. Additionally, to avoid the flux instabilities and long waiting times involved in changing the temperature of the large amount of As in the bulk zone, the pBN valve also acts as a BEP regulator. The cracking zone is kept at a considerably higher temperature (~1000 °C) than the bulk zone (~80 – 300 °C), both to prevent condensation of As on the valve, and to achieve the separation of As_4 tetramers into As_2 dimers.

2.2.3 Reflection high-energy electron diffraction

For growth rate calibration and growth monitoring, both C21 and GENII growth chambers are equipped with reflection high-energy electron diffraction (RHEED) systems, both of which comprise a STAIB electron source, a phosphor screen, and a digital camera. The electron source generates a beam of electrons which impinges upon the substrate and is diffracted by the crystalline substrate, while the phosphor screen captures the diffracted electron beam and the digital camera transfers the fluorescence image of the diffracted electrons to a PC for monitoring and analysis.

For RHEED analysis, the e^- beam is accelerated to 12 keV in the C21 and 17 keV in the GENII, and set to impinge onto the substrate at a low (~1°) angle, resulting in a diffraction pattern that, for sufficiently flat surfaces, is chiefly determined by the arrangement of ions on the surface of the substrate (surface reconstruction). The diffraction pattern is rendered into the visible spectrum on a phosphor screen mounted on a port on the growth chamber positioned opposite the e^- beam source.

Since a surface is a 2D object (i.e. it is "missing" a spatial dimension), its resulting diffraction pattern is degenerate. While a 3D lattice results in a diffraction pattern that is composed of a series of spots, when projected onto a screen, the 2D surface results in a series of parallel lines ("streaks"). Indeed, a RHEED diffraction pattern indicative of a smooth and well-formed surface is often said to be "streaky". On the other hand, if the surface of the sample still crystalline but rough, the electron beam, grazing angle notwithstanding, will traverse regions of bulk crystal, resulting in additive 3D lattice-produced diffraction spots. In the case of a rough crystalline surface, the RHEED pattern is often said to be "spotty." Additionally, a surface reconstruction is often of reduced symmetry with respect to the bulk crystal structure, to reduce the surface energy contribution to the free energy of the crystal. This reduce symmetry usually results in a 2D lattice that, while it is repeating just like the underlying bulk 3D lattice, is composed of a repeating cell that is larger, and often a multiple of, that of the bulk lattice.

For the case of the compounds used in this work (GaAs, AlGaAs), while their bulk crystal structure has cubic symmetry, their surface reconstruction at the growth temperature (580 °C) has a rectangular symmetry, with one side of the rectangle (along the $[\bar{1}\ 1\ 0]$ direction) 2 times the length of the side of the bulk unit cell, and the other side (along the $[1\ 1\ 0]$ direction) 4 times the length of the side of the bulk unit cell, resulting in the conventional notation for the surface reconstruction of (2×4). Correspondingly, the diffraction pattern due to the surface reconstruction will present, when viewed along the $[1\ 1\ 0]$ or $[\bar{1}\ 1\ 0]$ direction, 1 or 3 additional streaks between those belonging to the bulk crystal. Therefore, RHEED is a tool that permits the identification of both the thermodynamic and morphological state of the sample surface, offering insights on the surface temperature, V-group or III-group element overpressure, overall roughness. Additionally, the

RHEED is also a tool that allows for the identification of the orientation of the substrate with respect to the chamber and the effusion cells.

2.2.3.1 III-V growth rate calibration

To measure the growth rate of GaAs and AlAs, the phenomenon of intensity oscillation is exploited. The intensity of the central ("mirror-reflected") e^- beam diffraction spot is monitored immediately following the beginning of deposition on a smooth surface. The initial growth happens in a layer-by-layer mode, whereby islands start forming on a smooth layer and grow horizontally until joining together to form the next smooth layer.[2] The intensity of the reflected e^- will be maximum when a single smooth layer is complete (a "perfect mirror"), while it will be minimum when the formation of a layer is half-way complete, corresponding to the maximum roughness of a single incomplete layer (a "hazy mirror"). The growth rate is estimated assuming that one deposition layer corresponds to what we will term throughout this dissertation one "monolayer" (ML), i.e. half of the height of one III-V unit cell $a_0^{\mathrm{iii-v}}$.[2] Given the time in s t_n between n peaks in the intensity oscillation, the growth rate GR, in ML/s, is:

$$GR = \frac{n}{t_n}. \tag{2.2}$$

Consequently, using the material-dependent ML thickness $d_{\mathrm{ML}}^{\mathrm{iii-v}} = a_0^{\mathrm{iii-v}}/2$ measured in nm, the *GR* in nm/s is:

$$GR = d_{\mathrm{ML}}^{\mathrm{iii-v}} \frac{n}{t_n} = \frac{a_0^{\mathrm{iii-v}}}{2} \frac{n}{t_n}, \tag{2.3}$$

thus, in μm/h:

$$GR = 3.6 \frac{a_0^{\mathrm{iii-v}}}{2} \frac{n}{t_n}. \tag{2.4}$$

The growth rate for GaAs used for this work was ~1 μm/h, entertainingly corresponding to ~1 ML/s, since a_0^{GaAs} = 0.565325 nm.[3] For the $Al_{0.3}Ga_{0.7}As$ alloy, since re-evaporation of both Al and Gas at the growth temperature used for this work is nil, leading to additive (i.e. non-competitive) incorporation of the group III elements, the growth rate for Ga and Al can be calibrated separately, and the resulting alloy growth rate will be simply the sum of the two separate growth rates.[2] Consequently, for an overall growth rate of ~1 μm/h, Al and Ga were calibrated to a growth rate of ~0.3 and ~0.7 μm/h, or ~0.3 and ~0.7 ML/s, respectively, with a_0^{AlAs} = 0.56556 nm.[3]

2.2.3.2 Arsenic incorporation calibration

To prevent thermal decomposition of the epilayers from the heated substrate, an As overpressure must be maintained.[1] Indeed, for this work, the As BEP (~10^{-6} Torr) is set to be ~ 10 times that of, say, Ga (~10^{-7} Torr). However, to more quantitatively ensure a sufficient overpressure of As, we perform what we term an "incorporation-rate ratio" calibration.

As mentioned in Sec. 2.2.3, the surface reconstruction of GaAs at 580 °C is (2×4), resulting in a visible additional streak between the main diffraction streaks in the RHEED pattern when orienting the electron beam along (across) the [1 1 0] ([$\bar{1}$ 1 0]) direction. A sufficiently reduced As overpressure (say, closing the As effusion cell shutter) will result in a change in the surface reconstruction, resulting, along that crystal direction, in a change to a Ga-rich "4×" reconstruction, or, 3 additional streaks, with a very faint middle streak. Re-applying the original As overpressure (re-opening the As shutter) will recover the 2× reconstruction once again.

The As incorporation-rate ratio is thus defined as the time between closing the As shutter and the re-appearance of the As-rich reconstruction, divided by the time between re-opening the As shutter and the re-appearance of the As-rich reconstruction.[4,5] A higher number here corresponds in a faster As re-incorporation rate.

In practical terms, the intensity of the 2× is monitored while both As and Ga are being evaporated. At $t = t_1$, the As shutter is closed, leaving the Ga shutter open. Since the change in reconstruction results in a much fainter central streak, the monitored intensity shows a significant decrease. After no more than 5-10 seconds, in order to avoid the formation of Ga droplets, at $t = t_2$, the As shutter is re-opened. The monitored intensity increases again, and $t = t_3$ is identified as the time at which the intensity at $t = t_1$ is once again recovered. The incorporation-rate ratio IRR is therefore:

$$IRR = \frac{t_3 - t_1}{t_2 - t_1}. \tag{2.5}$$

For this work, the As flux was set to correspond to an IRR of 1.3 – 1.8, which typically ensures a smooth surface for both GaAs and AlAs.[6]

2.2.4 Substrate temperature calibration

As mentioned in Sec. 2.2.2.2, the substrate temperature is controlled with a heating filament and a thermocouple, i.e. the measurement of the actual surface temperature of the substrate is always indirect. Consequently, a calibration system must be employed to relate the thermocouple readings to the surface temperature.

For this work, since all the growths took place between 500 °C and 580°C, one calibration point was utilized. New epi-ready substrates, immediately after introduced in vacuum, present a thin layer of amorphous oxide, which must be removed before attempting any deposition. The removal of the oxide layer (oxide desorption) is accomplished simply by heating the newly introduced substrate, while monitoring the surface via the RHEED pattern. Since the oxide layer is amorphous, no coherent diffraction for the e^- beam can happen, resulting in an almost featureless, "hazy" RHEED pattern. It is known that the temperature at which the native oxide begins decomposition, revealing the GaAs surface beneath, is 580 °C.[7] The temperature is slowly raised while

observing the RHEED pattern. Once the oxide desorption has begun, a distinct change in the RHEED pattern from hazy to spotty is detectable. The TC reading of the temperature T_{m} ("manipulator temperature") at the moment of the RHEED pattern change T_{m}^{*} is recorded and is deemed to correspond to a surface temperature T_{s} of 580° C. With this one-point calibration, the surface temperature is considered to be related thus to the manipulator temperature T_{m} with:

$$T_{\mathrm{s}} = T_{\mathrm{m}} + (580 - T_{\mathrm{m}}^{*}). \tag{2.6}$$

2.3 Pulsed-Laser Deposition

2.3.1 Overview

Pulsed laser deposition (PLD) is a laser-ablated vapor deposition technique that has emerged as an attractive technique for the deposition of complex oxides, due to the ability to employ source materials of arbitrarily complex stoichiometry and the possibility of exact stoichiometric transfer from the source to the deposited film.[8] During PLD, a ~20 ns-pulsed laser is focused onto the surface of a solid target containing the source material. The source material is ablated by each laser pulse and travels, in the form of a plasma plume, either in vacuum, or in a pressure-controlled atmosphere of an arbitrary gas, until it impinges upon a heated rotating substrate. The In_2O_3-SnO_2 90-10 wt.% (ITO) layers described in Ch. 4 were deposited onto (0 0 0 1) sapphire in a Neocera PLD system, shown schematically in Fig. 2.3. The following sections describe the details of the PLD system used.

2.3.2 System details

2.3.2.1 In-vacuo mechanical components

The Neocera PLD vacuum system used for this work comprises a smaller load-lock chamber for substrate introduction, attached via a gate valve to a main chamber, containing the substrate manipulator and the target "carousel." The substrates are attached to a 2 in. diameter Inconel platen

with silver paint, after manually polishing the platen with polishing paper to remove residues of previous depositions. The silver paint was subsequently cured at 90°C for 4 minutes. Photographs of the mounted substrates before (after) deposition are shown in Figs. 2.5(a) [2.5(b)]. The platen with the mounted substrate is transferred from the load-lock chamber to the main chamber via a transfer-arm with 2 degrees of freedom (forwards/backwards between the two chambers, and raise/lower), where it is lowered onto the rotating assembly of the substrate manipulator, substrate facing down. A heated-filament substrate heater with a thermocouple is lowered so that it heats the back of the substrate platen. The bottom of the main chamber houses the target "carousel," a rotating circular structure comprising six rotating pillars, each of which can house one source material target. The cylindrical targets are 1 – 2 in. in diameter, ¼ – ½ in. in thickness. During deposition, the carousel is set up so that one target is positioned roughly beneath the substrate. The substrate-target distance is 7 cm.

2.3.2.2 Vacuum operation and gases

The main chamber and the load-lock chamber are separately pumped by a set of Pfeiffer turbo-molecular pump backed by a dry-scroll pump each. The pressure in each chamber is monitored with MKS combination pressure gauges, each including microPirani, hot cathode, and piezo gauges, to cover the entire range of pressure from 1 atm to ~10^{-8} Torr. High purity (99.999%) N_2, O_2, or Ar can be introduced into the chamber in a controlled manner during growth via a mass flow controller (MFC), with the ability to either set a fixed gas flow, or use a PID-based flow-regulation system to maintain a set pressure. The high-purity N_2 also doubles as venting gas for both chambers.

2.3.2.3 Laser path

The PLD system is equipped with a Lambda Physik COMPex 205 KrF excimer UV laser, with a 25 ns pulse width, 248 nm laser light wavelength, and capable of pulse repetition rates of up to 50 Hz and pulse energies of up to 600 mJ per pulse. The pulse energy is indirectly set by regulating the voltage of the excimer gas excitation (18.0 kV – 28.0 kV). Immediately upon exit from the laser shutter, the 9 mm × 24 mm rectangular laser pulse is passed through a 1 cm-diameter circular aperture to obtain a symmetrical laser spot shape and trim the laser diffraction lines. The laser pulse is then passed through a ~2 m long mirror path to disperse the more divergent portion of the pulse in a process termed "homogenization." After the homogenization, the laser pulse is directed through a focusing lens with a focal length of 50 cm. The lens is mounted on a scaled optical rail for repeatable positioning of the lens with respect to the surface of the target for spot size calibration. The laser beam and the axis of the lens are oriented at a 45° angle with respect to the horizontal plane and the surface of the target.

After passing through the lens, the laser pulse traverses a high-UV-transparency, anti-reflection-coated window mounted on the main chamber, to minimize reflection and absorption losses. Additionally, to prevent losses due to build-up of unintentional deposition of ablated material on the vacuum side of the window, the vacuum side of the window is periodically polished with lint-free wipes and silica particulate colloid suspension. By comparing the laser pulse energy measured after the lens, with and without the clean UV-transparent window placed before the laser energy meter, we were able to verify that the clean window exhibits the ideal loss of 2% of pulse energy.

2.3.2.4 Target operation

After traversing the window into the main vacuum chamber, the focused laser pulse finally impinges upon the target, generating a plasma plume. Photographs of representative plasma plumes obtained from ITO targets in various N_2 pressures are shown in Fig. 2.4. The mirrors and lens in the in-air laser path have been set up so that the laser ablation spot on the surface of the target in use is directly underneath the center of the substrate platen, which has been mounted facing down towards the target. Since during deposition the target may experience the impingement of several thousands of laser pulses, a still target will result in the laser pulses carving a hole in the surface of the target, compromising the characteristics of the ablated plasma. Therefore, to avoid excessive repeated impingement of the laser onto the same region, the target carousel movement is set so that the target rotates around its axis, and the center of the target is continuously shifted from side to side. This movement, termed "target rastering," helps continuously shift the recently ablated region of the surface of the target away from the laser spot and results in lobed-curve patterns of ablated spots, which we also term "ablation roses." Care is taken to adjust the rastering movement (chiefly, the maximum extension on both sides of the periodic lateral movement) so that the ablation rose covers almost entirely the surface of the target, to avoid introducing large unevenness in the surface, and so that the laser spot does not encounter the target edges. A photograph of the ablation rose is shown in Fig. 2.5(c). After each deposition, the target is manually polished with polishing paper to maintain a smooth and flat surface for the next deposition.

2.3.3 Laser pulse energy and spot size calibration

Due to its effect on the kinetic energy, spatial energy distribution, and expansion dynamics of the ablated plasma plume, the energy and spot size of the laser pulse are important parameters of the deposition. While, traditionally, the laser pulse characteristics can simply be reported as a

fluence, i.e., the laser energy per unit surface, we found during this work that different laser energies and pulse spot sizes may result in different deposited stoichiometries and morphologies, even while keeping the fluence constant. Therefore, for the present work, careful independent calibration and repeatability of both the laser pulse energy and laser pulse spot size proved necessary.

The laser pulse energy is measured with a computer-controlled Gentec laser energy meter. The energy meter is mounted on a magnetic detachable optical post that can be placed after the focusing lens, immediately before the UV-transparent main chamber window. After setting the excimer gas excitation voltage that is expected to yield the desired laser pulse energy, 500 pulses at 2 Hz are set to impinge upon the laser energy meter, while the laser energy meter software records the measured energy of each pulse and the average energy is recorded. The excimer gas excitation voltage is then adjusted, as needed, until the desired pulse energy is obtained. It is useful to note that this calibration can be performed without venting the main chamber.

To calibrate the laser spot size on the surface of the target, adjustment of the focusing lens – target surface distance is required. The laser spot size is measured by exposing a portion of laser alignment paper, or "burn" paper, to one laser pulse. The burn paper is a black polymer-coated sheet of cellulose, when a laser spot impinges upon the surface of the burn paper, the black polymer is ablated revealing a white mark that is a trace of the laser beam and can be used to measure its cross section. A section of burn paper is taped onto a sacrificial target, and this target is placed on the target carousel in the main chamber, under the substrate, in the focused laser path. It is useful to note here, in contrast with the pulse energy calibration, this calibration requires the venting of the main chamber.

Due to the shape of the initial circular aperture, the transversal cross-section of the laser beam is also expected to be roughly circular, however, since the target surface is tilted at 45° with

respect to the direction of the lens axis and the laser beam, the laser pulse trace on the surface of the target, or on the burn paper, is expected to be roughly elliptical. To measure the spot size, we simply measured the width and height of the roughly elliptical mark left on the burn paper with a caliper. Consequently, the laser pulse fluence can also be calculated as the measured pulse energy divided by the measured spot size.

2.4 Atomic Force Microscopy

The morphology of the InAs/(Al)GaAs QD arrays discussed in Ch. 3 was analyzed using a Veeco Dimension Icon atomic force microscope (AFM), operated in "ScanAsyst" mode, whereby an etched silicon probe with elastic constant k ~ 0.4 N/m, height 3 – 8 μm, and nominal radius 2 nm is mounted on a piezo-electric crystal controller that is modulated in the z (vertical with respect to the surface of the sample) direction at ~ 2 kHz.

Atomic force microscopy is often performed in a variation of "tapping mode," whereby a ~ 10 – 100 μm length, ~10 nm radius single crystal probe is mounted on a ~ 500 μm cantilever and the probe/cantilever system is mounted on a piezo-electric scanning "tube", shown in Fig. 2.6, with the probe tip facing down towards the sample. Via the scanning tube, the probe is set into oscillation along the vertical direction of the surface of the sample. The scanning tube is responsible for the coarse vertical movement and the finer vertical oscillation of the probe and the horizontal x and y movement of the probe (rastering) via the application of a voltage across the electrodes shown in Fig. 2.6.

To monitor the oscillation of the probe, a laser light is shined on the opposite side, with respect to the probe, of the cantilever. The reflected laser light is directed towards a 2 × 2 matrix of photodiodes via an adjustable prism. The photodiode matrix is able to detect both vertical and

horizontal deviations from the steady state of the probe oscillation. A schematic of this operation is represented in Fig. 2.7.

To obtain an AFM image, the probe is moved through a square matrix of equidistant points along the surface of the sample (i.e. "rastered"), which represent the pixel positions in the final image. For each point, the oscillating probe is lowered towards the sample until a variation in the amplitude of the probe oscillation is detected, indicating contact with the sample surface, at which point the local height of the sample $z(x, y)$ is recorded. The final image is a collection of height values z for each (x, y) coordinate.

Since the extension of the piezo-electric tube is not linear, especially at large distances ($\gtrsim$ 1 μm), an arc-like distortion termed "bowing" is introduced[9] into the height profile. To remedy this distortion, in this work, a quadratic-fit background was removed from the height profile using the scanning probe images manipulation software Gwyddion.[10]

2.5 Scanning electron microscopy

The morphology and composition of In_2O_3-SnO_2/sapphire layers discussed in Ch. 4 were analyzed with an FEI XL 30, or a Tescan MIRA 3 scanning electron microscope (SEM), with electron beam acceleration in the range 10 – 30 kV, beam current in the range 40 – 400 pA and nominal spot size in the range 3 – 10 nm.

SEM is a form of scanning probe microscopy/spectroscopy whereby a small probe consisting in a focused beam of accelerated electrons is scanned across the surface of a sample. The collision between the accelerated electron probe and the surface of the sample results mainly in: (1), the emission of secondary (SE) electrons from the excitation of the atoms in the sample, (2) the backscatter of probe electrons (BSE) from their interaction with the positive nuclei in the sample, and (3) the emission of X rays, from the excitation and subsequent relaxation of core electrons

within the sample. The work in this dissertation employs SE for morphological analysis and X-ray energy dispersive spectroscopy (XEDS or EDS) for compositional analysis.

Electron generation in both microscopes is achieved via the use of a field emission gun (FEG), whereby a sharpened tungsten tip facing an anode plate is heated to 1800 K emitting electrons which are accelerated by the anode generating the electron beam. The electron beam travels in the FEG column through a series of electrostatic lenses that serve to focus, center, and correct the astigmatism of the beam. Finally, before the beam exits the column through the objective aperture, the scanning coils periodically deflect the beam to achieve the scanning (raster) movement necessary to obtain images.

The secondary electrons are collected via an Everhart-Thornley detector, which consists of a positively-biased grid, a scintillator, and a photo-multiplier. The positively-biased grid is placed in front of the scintillator, facing the sample. The secondary electrons resulting from the impingement of the electron beam are attracted by the grid and accelerated towards the scintillator. The impingement of the SE onto the scintillator generates light which is detected by the photomultiplier. As the number of electrons detected is largely proportional to the height of the sample surface at a given position, the resulting image is a topography of the sample, with dark (light) areas being at lower (higher) positions.

2.6 X-ray diffraction

X-ray diffraction spectra from the ITO layers were collected on a Rigaku Smartlab using Cu Kα_1 radiation from a rotating Cu anode and a scintillation counter detector. The anode was operated at 40 kV and 44mA. The x-ray beam was monochromatized with a Ge(220)x2 monochromator and focused with parallel-beam configuration optics. The width of the beam was limited

with a 5.0 mm length limiting slit. The vertical divergence of the incident beam was limited with a motorized incident slit with aperture set at 0.05 mm.

The sample was mounted on a stage capable of vertical (z) movement and rocking (ω and χ) movements. The sample height was centered within the incident beam by adjusting the stage z until the intensity of the direct beam was halved. The alignment of the sapphire substrate crystal with respect to the x-ray beam optics was obtained by setting the x-ray source and the detector at $\theta/2\theta = 41.6750°$, which is the Bragg angle corresponding to the 0 0 0 6 reflection of sapphire, and repeatedly adjusting the ω and χ inclination of the stage until the intensity of the 0 0 0 6 is maximized.

The in-plane divergence of the receiving beam was limited with a 5.0° angular aperture parallel-plates Soller slit, while the vertical divergence of the receiving beam was limited by two motorized receiving slits with aperture set at 5 mm. Automatic attenuation of the receiving beam intensity was set to switch on when reaching 400000 cps and off when falling back to 5000 cps.

2.7 Transmission electron microscopy

High resolution transmission-electron microscopy (TEM) imaging of the ITO NW was performed in a Jeol 2100F probe-corrected scanning TEM (STEM) equipped with a two-stage Cs corrector. The electron beam was produced by a zirconated tungsten thermal field emission tip and accelerated to 200 kV.

The probe correction was performed before each imaging session on a standard consisting of ~100 nm Au nanoparticles dispersed on a C film TEM grid. The probe correction was done in two stages: first, manual adjustment of the coma (inclination of the beam) and 2-fold astigmatism, then, computer-assisted Cs correction to obviate 3-fold and 4-fold astigmatism as well as spherical aberration.

For high-resolution scanning TEM imaging, a nominal spot size of ~1 nm was uses, and images were collected in the "bright-field" configuration, i.e. with a CCD detector positioned within the beam path.

2.8 Figures

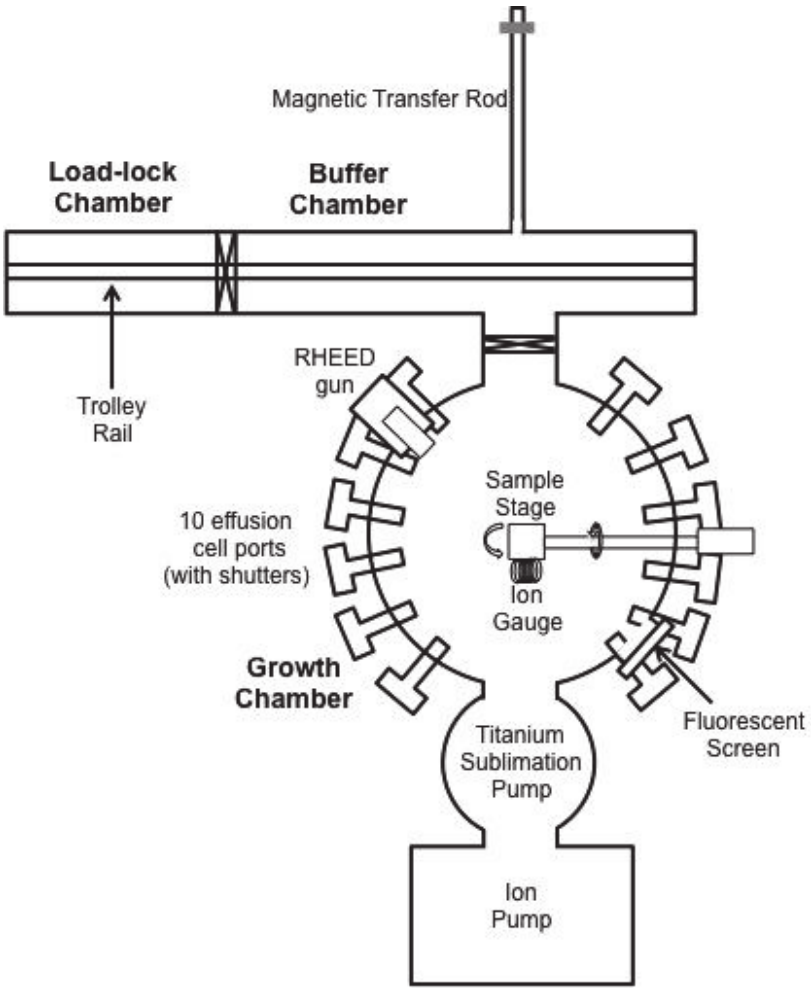

Figure 2.1: Schematic diagram of the Riber C21 MBE used for synthesizing the InAs/AlGaAs QDs.

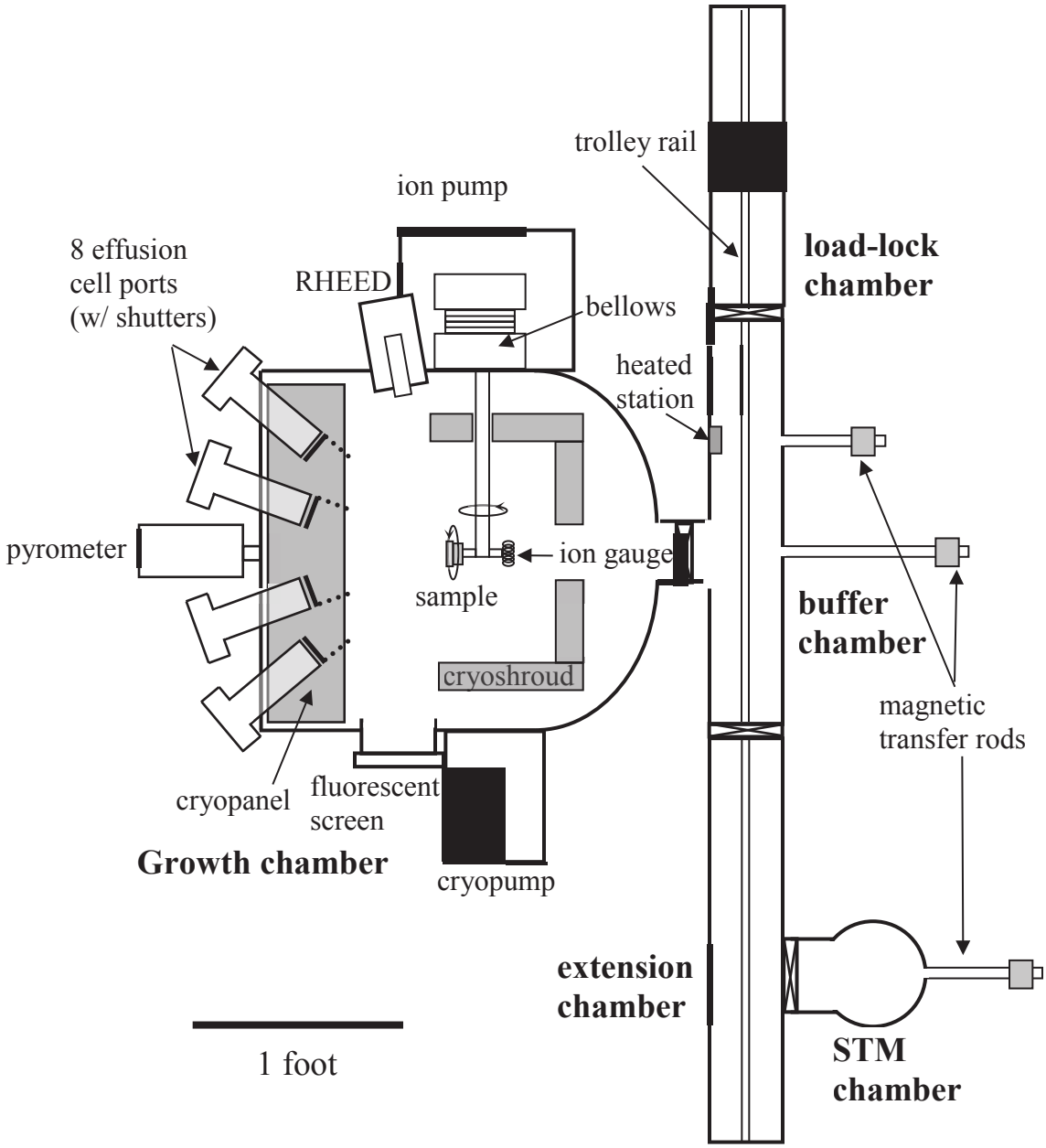

Figure 2.2: Schematic diagram of the Veeco GENII MBE used for synthesizing the AlGaAs buffers.

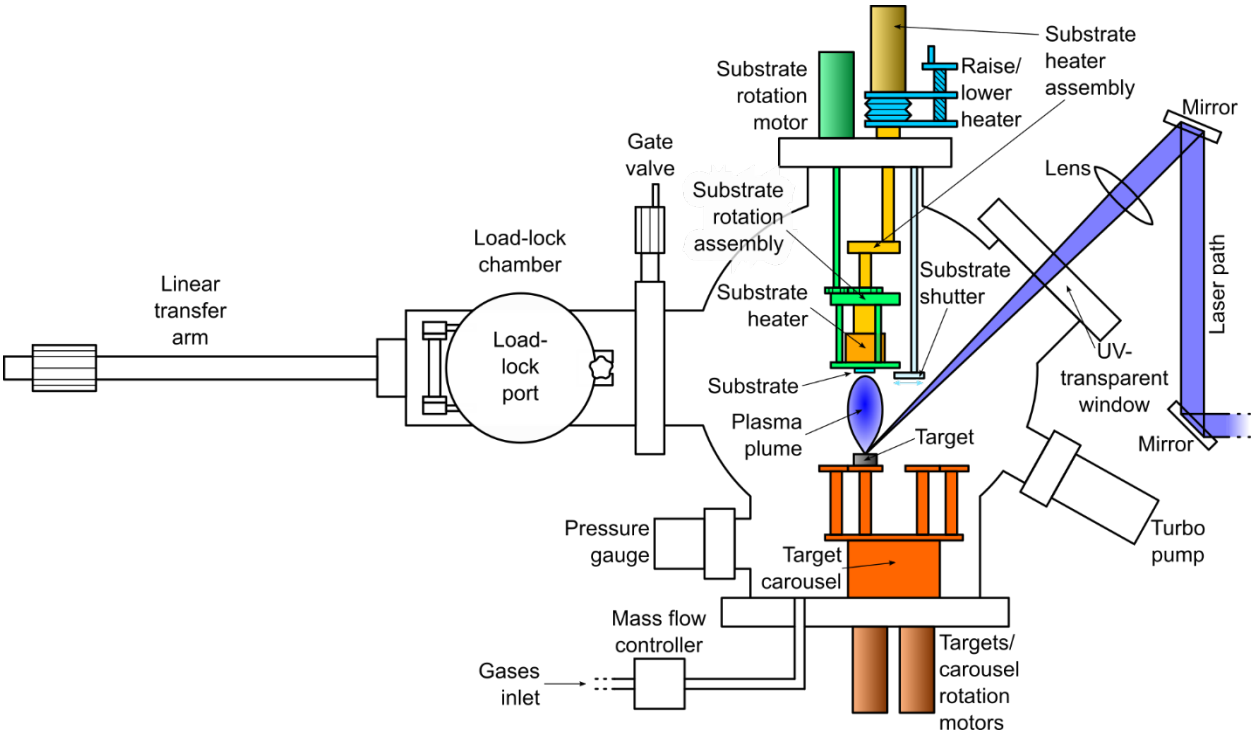

Figure 2.3: schematic drawing of the Neocera pulsed laser deposition system used for synthesizing the indium oxide – tin oxide films.

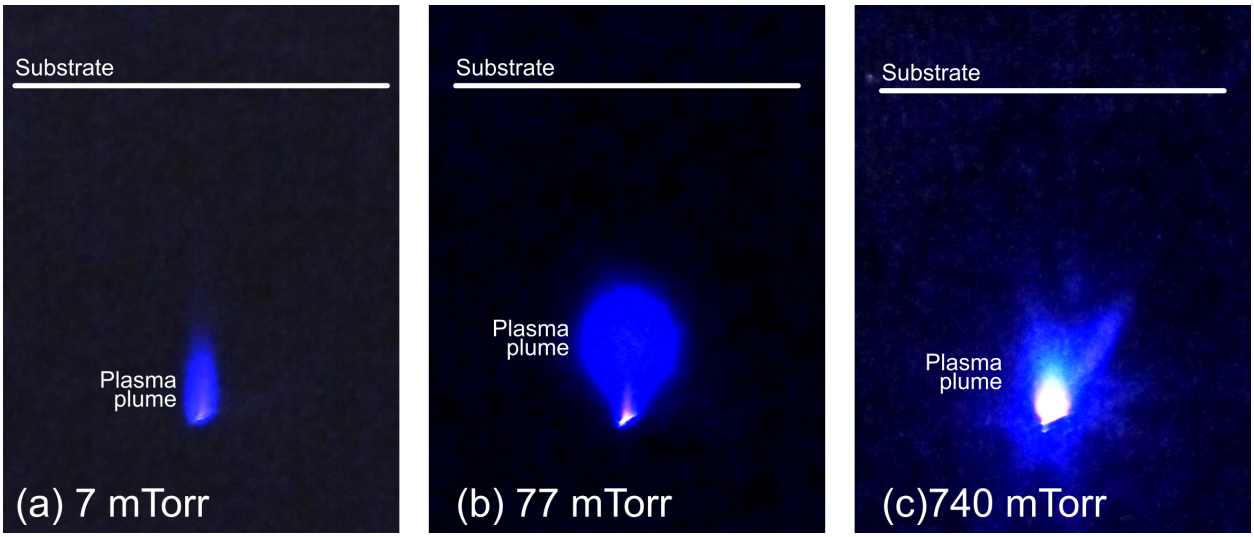

Figure 2.4: visible-light pictures of the plasma plume obtained by ablating the ITO target in increasing N_2 pressure. **(a)** 7 mTorr, **(b)** 77 mTorr, and **(c)** 740 mTorr N_2 pressure. The same ITO target, and the same laser spot energy and size (respectively, ~70 mJ, ~0.09 cm^2) as those employed in the production of the samples discussed in Ch. 4. The pictures were obtained by integrating several (>10) photographs of plasma plumes for each pressure condition, in other words, they likely represent the largest size the plume will be for each pressure condition. The resulting plasma plume lengths appear to be approximately between ⅓ and ½ of the target - substrate distance.

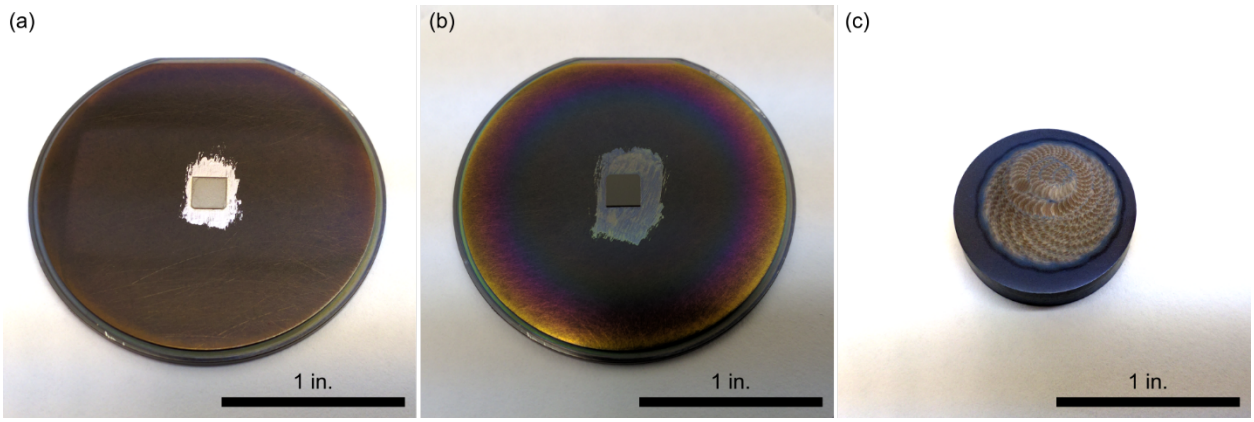

Figure 2.5: photographs of the substrates mounted on PLD substrate holders and a target. **(a)** 5 mm × 5 mm sapphire substrate mounted on the substrate holder with silver paint, before deposition. **(b)** Substrate after deposition. A ~1 in. diameter gray discoloration is apparently covering the center of the substrate holder, indicative of the formation of nanowires. **(c)** ITO target at the end of deposition. The ablation "rose" is visible on the surface of the target.

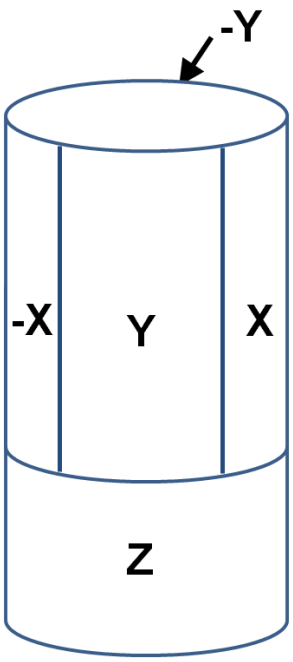

Figure 2.6: schematic drawing of the AFM piezo-electric scanning tube. The drawing indicates the portions that are mutually insulated, independently operated, and are responsible for the three directions x, y, z of movement/oscillations. Reproduced from Dr. Simon Huang's dissertation (University of Michigan, 2015).

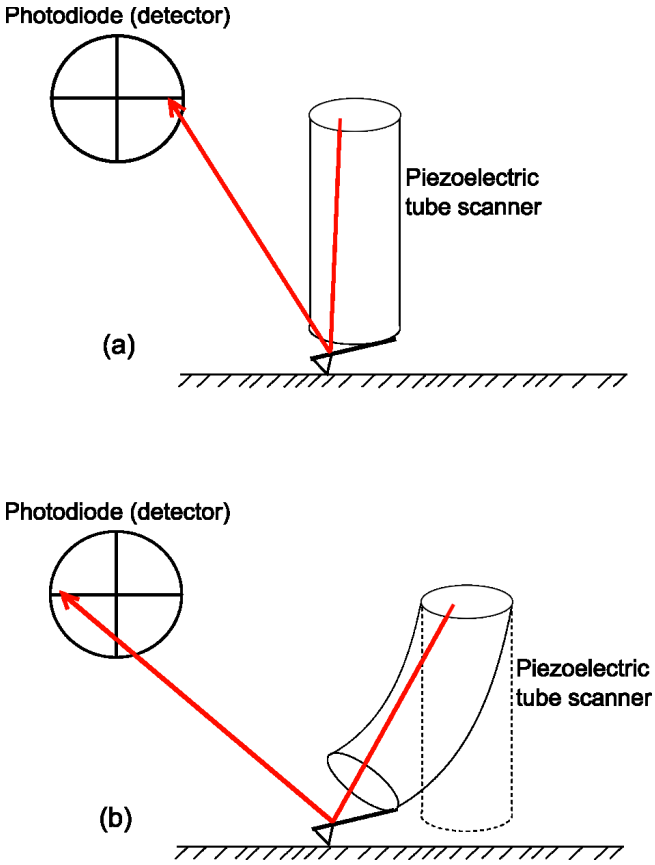

Figure 2.7: schematic representation of the operation of the AFM scanning tube. The laser light is represented by the red arrowed line. The photodiode, as depicted, is composed of four separate quadrants. The deflection of the tube scanner is exaggerated to better show the deflection of the laser light. Reproduced from Dr. Simon Huang's dissertation (University of Michigan, 2015).

2.9 References

[1] R.A. Kubiak, S.M. Newstead, and P. Sullivan, "The Technology and Design of Molecular Beam Epitaxy Systems", in *Molecular Beam Epitaxy: Applications to Key Materials*, edited by R.F.C. Farrow, (Noyes, Park Ridge, New Jersey, 1995), pp. 1–113.

[2] I. V Markov, *Crystal Growth for Beginners* (WORLD SCIENTIFIC, 2003).

[3] I. Vurgaftman, J.R. Meyer, and L.R. Ram-Mohan, "Band parameters for III–V compound semiconductors and their alloys" J. Appl. Phys. **89**, 5815 (2001).

[4] H.Q. Hou and C.W. Tu, "In situ control of As composition in InAsP and InGaAsP grown by gas-source molecular beam epitaxy" Appl. Phys. Lett. **60**, 1872 (1992).

[5] T.P. Chin, B.W. Liang, H.Q. Hou, M.C. Ho, C.E. Chang, and C.W. Tu, "Determination of V/III ratios on phosphide surfaces during gas source molecular beam epitaxy" Appl. Phys. Lett. **58**, 254 (1991).

[6] S.R. Bank, An Introduction to MBE, http://lase.ece.utexas.edu/mbe.php; accessed 29 November 2018.

[7] E.C. Larkins and J.S. Harris Jr., "Molecular Beam Epitaxy of High-Quality GaAs and AlGaAs" in *Molecular Beam Epitaxy: Applications to Key Materials*, edited by R.F.C. Farrow (Noyes, Park Ridge, New Jersey, 1995), pp. 114–274.

[8] D.P. Norton, "Pulsed Laser Deposition of Complex Materials: Progress Towards Applications," in *Pulsed Laser Deposition of Thin Films – Applications-Led Growth of Functional Materials*, edited by R. Eason (John Wiley & Sons, Hoboken, NJ, 2007)

[9] R. Howland and L. Benatar, "A Practical Guide to Scanning Probe Microscopy." (Park Scientific Instruments. 1996).

[10] D. Nečas, P. Klapetek, “Gwyddion: an open-source software for SPM data analysis” Open Phys. **10**(1), 181 (2012).

Chapter 3: Influence of Surface Nano-Patterning on the Placement of InAs Quantum Dots

3.1 Overview

In this chapter, we examine the influence of patterning of (Al)GaAs surfaces on the nucleation and evolution of positioning of InAs quantum dots. The objective of this work is to employ a computational (growth simulation) and experimental (quantum dots positioning pair correlation) approach to identify the influence of substrate curvature on quantum dots positioning, and quantify the degree of alignment of quantum dots with increasing intensity of surface patterning.

The chapter begins with an overview of earlier experimental approaches to ordering of quantum dots, as well as earlier computational methods employed to simulate quantum dots growths. Next, we describe the experimental techniques employed here to obtain the patterned (Al)GaAs surfaces and InAs quantum dots layers. A description of the phase-field model method used to simulate the InAs quantum dot layer growth, and of a polar coordinates-variation of the pair correlation function computation for quantifying quantum dots alignment follow. We find that the presence of surface mounds results in regions of large positive local curvature (valleys), which are preferential positioning sites for quantum dots. The presence of surface mounds also results in earlier quantum dots nucleation and larger mass transfer from wetting layer to quantum dots after nucleation due to curvature-driven surface diffusion. For the intensity of surface patterning, we find no quantum dot alignment on flat surfaces, while the presence of mounds results in chain alignment of quantum dots along the mounds. These findings likely extend to any mounded surface

an enable a detailed understanding of the role of local surface curvature in influencing surface diffusion and quantum dots placement.

The work described this chapter was peer-reviewed and published in D. Del Gaudio, L.K. Aagesen, S. Huang, T.M. Johnson, B.D. Faeth, H. Lu, R.M. Ziff, and R.S. Goldman, "Influence of surface nano-patterning on the placement of InAs quantum dots" Journal of Applied Physics **124**, 115307 (2018).

3.2 Background

The control of lateral ordering of self-assembled semiconductor quantum dots (QDs) is desirable for a wide range of solid-state applications, including lasers, solar cells, and thermoelectrics, as well quantum computing and telecommunication devices.[1,2,3,4,5] Lateral ordering of QDs is often achieved via lithographic patterning with photons, focused-ion-beams, electron beams, or block-co-polymers;[6,7,8] however, these methods require multiple fabrication steps and often introduce lattice defects.[9,10,11] Therefore, bottom-up methods, which do not require extrinsic patterning, have been pursued.[12] For example, deposition kinetics have been exploited to achieve vertical alignment of QD multilayers.[13,14,15] In these cases, the first layer of QDs is typically distributed isotropically; following the deposition of a spacer layer, anisotropic strain accumulation drives the vertical alignment of subsequent layers of QDs.[16,17,18]

Recently, lateral QD alignment has been achieved using surface nano-patterning methods, such as lithography-etched mesas[19] and nano-holes obtained via arsenic-debt epitaxy.[20] Alternatively, in-situ nano-patterned surfaces may be obtained using the step-bunches associated with surface "mounds" induced by the Ehrlich-Schwoebel energy barriers that prevent adatoms from stepping down the edges of surface islands.[21] QDs have been reported to decorate step edges (such

as on the side of mounds) at the nucleation stage,[22,23,24] while fully formed QDs have been observed to align themselves along the base of the mounds.[25] However, the influence of the surface morphology on QD positioning after the nucleation stage, i.e. during growth and coarsening, is not well understood. For free-standing nanocrystals,[26] and those formed on artificially flat[27,28] and patterned surfaces,[29,30,31] the time evolution of the surface has been simulated using phase-field models based upon the Cahn-Hilliard equation, with free energy functionals that account for bulk, interfacial, and (where appropriate) elastic energies. All parameters used in the model were literature-derived physical quantities, with the only exception the deposition rate, which was set to the experimental value. In this work, we perform a phase-field simulation of QD nucleation and growth in two dimensions (growth direction and one perpendicular direction) using the measured substrate surface profile as the initial condition. We use atomic-force micrographs of GaAs surfaces prepared by molecular beam epitaxy, with and without naturally forming elongated surface "mounds," as input into the phase-field simulations. Our combined computational-experimental approach reveals that QDs grown on mounded substrates nucleate earlier than those grown on flat substrates. As the growth progresses beyond the nucleation stage, preferential positioning of QDs at regions of larger positive curvature, such as at the edge of the mounds, is observed. We compute polar-pair correlations of the QD positions from atomic-force micrographs for (Al)GaAs substrates as a function of increasing lateral mound angle, revealing a tendency for QD alignment on mounded surfaces. We discuss the influence of curvature-driven diffusion on the spontaneous ordering of QDs, demonstrating the applicability of this mechanism to (Al)GaAs mounds.

3.3 Experimental Methods

All of the layers were grown on GaAs (001) substrates using solid Ga, As_4, and In sources. Buffers consisting of a series of bilayer height steps, termed "flat buffers," and those containing

elongated “mound”-like features, termed “mounded buffers,” were prepared. After holding the substrates at 600°C for 10 minutes to ensure complete removal of surface oxide, an initial 300 – 500 nm GaAs layer was deposited at 580 °C, using an As_4/Ga beam-equivalent pressure (BEP) ratio of ~30 and a growth rate of 1 μm/h. For the flat GaAs buffers, three subsequent annealing steps were performed: 15 min. at 580 °C, 15 min. at 530 °C with half the original As_4 flux, and finally 10 min. at 370 °C without As_4. We note that in Ref. 15 the flat GaAs buffers were termed “high-low” (HL) buffers, reflecting the growth and annealing temperatures. For the mounded GaAs buffers, an additional 20 nm GaAs layer was deposited at 500 °C, without subsequent annealing. In Ref. 15, the mounded GaAs buffers are termed “low” (L), reflecting the growth temperature of the final GaAs layer. To prepare the mounded AlGaAs buffers, a 50 nm $Al_{0.3}Ga_{0.7}As$ layer was deposited at 580 °C with a V/III BEP ratio in the range of 13 to 27, followed by a 3 min annealing step at 580 °C, without sample rotation. For the growth rate of the $Al_{0.3}Ga_{0.7}As$ layer, the Ga and Al cells were separately calibrated for a growth rate of 0.7 μm/h and 0.3 μm/h, respectively, corresponding to an overall growth rate of 1 μm/h for $Al_{0.3}Ga_{0.7}As$ with simultaneous evaporation of Ga and Al both.

Following buffer growth, the 2D to 3D growth mode transition, indicative of QD formation, was monitored using reflection high-energy electron diffraction. For the GaAs buffers, InAs was deposited at 500°C, using a growth rate of 0.1 ML/s. The total InAs deposition time was 26 s, corresponding to an average InAs layer thickness of 2.6 ML = 0.79 nm. For the AlGaAs buffers, InAs was deposited at 545 °C, using 25 to 29 repeats of 5 s InAs deposition followed by 25 s annealing in As_4. For all AlGaAs buffers, an InAs growth rate of 0.03 ML/s was used, with 125 to 145 s total deposition time, corresponding to 3.75 ML (1.1 nm) to 4.35 ML (1.3 nm) InAs layer thicknesses.

Following growth of both the buffers and QDs, the surface morphology was examined ex-situ with tapping mode AFM, using etched Si probes with ~2nm tip radius. The resulting AFM images were sequentially processed via image-wide 2nd order polynomial background subtraction, line-by-line alignment by median matching, and image-wide planar background subtraction.[32] In Fig. 3.1, AFM topography images are presented for various buffers prior to and following QD deposition. For GaAs buffers prior to QD deposition, Fig. 3.1(a) reveals a relatively flat surface (0.22 nm RMS roughness), with a series of bunched steps,[15] while Fig. 3.1(c) reveals a mounded GaAs surface. For the mounded GaAs surface, line-cuts selected from the image in Fig. 1(c) reveal average mound lengths (~800 nm), widths (~200 nm), and heights (~3 nm), with 1.8° mound inclination angle,[15] consistent with earlier reports.[13,33] For the AlGaAs buffers prior to QD deposition, Fig. 3.1(e) and 3.1(g) reveal, respectively, average mound lengths of 320 nm and 490 nm, widths of 110 nm and 140 nm, and heights of 2.1 nm and 3.5 nm, with (e) 2.7° and (g) 5.1° mound inclination angles.

The morphologies of QDs grown on the flat and mounded (Al)GaAs buffers are captured in the AFM images in Figs. 3.1(b), 3.1(d), 3.1(f), and 3.1(h). It is evident that the QDs grown on the flat surface [Fig. 3.1(b)] have a larger diameter and a lower density than the QDs grown on the mounded surfaces [Figs. 3.1(d), 3.1(f), and 3.1(h)], consistent with earlier reports. To quantify the QD sizes, densities, and relative positions, we use a 3-step algorithm to identify the QDs in several images spanning an area >3 μm^2. First, the Laplacian of the AFM topography image is computed, and clusters of adjacent pixels within the bottom $48\% \pm 6\%$ of the Laplacian values are considered possible QDs. Next, the volume of each pixel cluster is computed as $V_0 - V_{\mathcal{L}}$, where V_0 is the sum of the pixel heights multiplied by the pixel area, and $V_{\mathcal{L}}$ is the volume of the estimated background under the pixel cluster.[34] The background is estimated by solving Laplace's equation

$\nabla^2 f_\ell = 0$ with the heights and slopes of the pixels along the border of the pixel cluster as boundary conditions.[35] We discard those pixel clusters with volume $< 1\% \pm 0.8\%$ of the volume range, as they are most likely due to noise. Finally, we calculate the height of all pixel clusters and define as QDs those with heights $> 8\% \pm 1.7\%$ of the height range. The 2D QD densities and average QD diameters are captured in Table 3.I.

To measure the average lateral mound slope for a given sample, six representative mounds were identified in the AFM topography images for each sample. For each mound, a line-cut was taken across the [110] direction. The mound width was determined as the x-distance between the two local height minima on either side of the mound, while the mound height was determined as the z-height distance between the lower minimum on either side of the mound and the local maximum in the middle of the mound. To measure the lateral mound angle, the portions of the line-cut containing the two lateral slopes of the mound were separately isolated and a linear fit was performed. The acute (< °90) angle of the two linear fit lines was measured and the lateral angle for that mound was taken as the average of the two angles. Appendix D.1.2 shows the mounds statistics for all samples discussed in this dissertation.

To quantify the influence of the mounds on QD clustering, polar pair correlation functions of the QD positions are computed. For each QD, a circularly uniform mass distribution is assumed, and the QD centers of mass are identified as the QD positions. The QD positions are then scaled by the average nearest-neighbor (NN) QD separation.

3.4 Computational Methods

3.4.1 Phase-field model simulation of InAs / GaAs quantum dots

For the 2D phase-field simulations of QD growth, initial surface profiles consisting of [1 1 0]-oriented line-cuts were selected from 1 μm^2, 512 × 512 pixels, AFM images such as those

shown in Figs. 3.1(a) and 3.1(b). Thus, for the flat and mounded GaAs surfaces, the initial surface profiles are represented by the black lines in Figs. 3.2(c) and 3.2(g). For the flat surface in Fig. 3.2(c), the maximum height variation is 0.9 nm, corresponding to ≤ 2 ML. For the mounded surface in Fig. 3.2(g), the maximum height variation is 2.9 nm, corresponding to ≤ 5 ML. In Fig. 3.2(g), three mounds are indicated by highlight, with widths of 130 nm, 120 nm and 140 nm, and heights of 1.3 nm, 2.4 nm and 1.1 nm, which correspond to lateral inclination angles of 1°, 1.5°, and 1.5°, respectively.

The nucleation and growth of InAs QDs on flat and mounded surfaces were simulated using a phase-field model,[16] describing the evolution of the system comprising three physical phases: vapor, InAs layer, and GaAs surface. The phase of the system at each point in the simulation is represented by a set of order parameters, (ϕ_1, ϕ_2, ϕ_3). In the vapor, $(\phi_1, \phi_2, \phi_3) = (1, 0, 0)$; in the InAs, $(\phi_1, \phi_2, \phi_3) = (0, 1, 0)$; and in the GaAs,$(\phi_1, \phi_2, \phi_3) = (0, 0, 1)$, and the order parameters are constrained such that $(\phi_1 + \phi_2 + \phi_3) = 1$. It is assumed that the GaAs phase remains unchanged throughout the deposition, and adatom diffusion is limited to the vapor/InAs layer interface. The time evolution of ϕ_2 is described by the Cahn-Hilliard equation with a source term for deposition:[19,27,26]

$$\frac{\partial \phi_2}{\partial t} = \nabla \cdot [M \nabla \mu] + S, \tag{3.1}$$

where $M = 16 M_S \phi_1^2 (1 - \phi_1)^2$ is the functional form of the In adatom mobility, using In adatom mobility value $M_s = D_s \,/\, (\gamma_{12} \ell_{12})$,[36] and $\nabla \mu$ is the chemical potential gradient for In. $S = dRn_z \phi_1 (1 - \phi_1)$ is the deposition term, where d is the deposition rate, R is a random number ranging from 0.9 to 1.1, which provides noise in the deposition flux, and n_z is the z-component of the surface normal, which accounts for the orientation of the surface in calculating the flux normal

to the surface from the deposition rate. The chemical potential is $\mu = \delta F/\delta\phi_2$, where F is a free energy functional similar to that in Ref. 16:

$$F = \int_V \left[\sum_{i=1}^{3} \sum_{j=i+1}^{3} W_{ij}\phi_i^2\phi_j^2 - \frac{\alpha_{ij}^2}{2}\nabla\phi_i \cdot \nabla\phi_j + f_{el} \right] dV \qquad 3.2$$

where W_{ij} are the free energy barrier heights and α_{ij} are the gradient energy coefficients. The elastic energy density f_{el} is given by[16]

$$f_{el} = \frac{1}{2} \sum_{i,j=1}^{2} \sum_{k,l=1}^{2} C_{ijkl}\big(\epsilon_{ij} - \eta\delta_{ij}\big)(\epsilon_{kl} - \eta\delta_{kl}) \qquad 3.3$$

where C_{ijkl} are the stiffness coefficients, ϵ_{ij} is the strain tensor, δ_{ij} is the Kronecker delta ($\delta_{ij} = 1$ for $i = j$, $\delta_{ij} = 0$ for $i \neq j$), and $\eta = \eta_0 Q(\phi_2)$ where η_0 is the misfit strain of the InAs lattice relative to the GaAs lattice[37] (see Table 3.III), and $Q(\phi_i) = (3\phi_i^2 - 2\phi_i^3)$, which is an interpolation polynomial. The stiffness tensor coefficients are interpolated using $C_{ijkl} = C_{ijkl}^{(1)} + Q(\phi_2)\left(C_{ijkl}^{(2)} - C_{ijkl}^{(1)}\right) + Q(\phi_3)\left(C_{ijkl}^{(3)} - C_{ijkl}^{(1)}\right)$, where $C_{ijkl}^{(p)}$ are the stiffness coefficients for phase p (see Table 3.II). Note that the functional form of misfit leads to misfit between InAs and vapor, as well as InAs and GaAs, but, as will be discussed later, the vapor will be treated as a compliant material with a very small elastic modulus and thus will not alter the results.

For each time step, Cahn-Hilliard equation and the mechanical equilibrium equation $\nabla \cdot \sigma = 0$, where σ is the stress tensor, were solved iteratively, whereby the order parameters ϕ_i resulting from the Cahn-Hilliard equation were used to calculate the stress tensor for the mechanical equilibrium equation, and the displacement field u resulting from the mechanical equilibrium equation was used to compute the elastic energy f_{el} for the Cahn-Hilliard equation in the next iteration. Thus, the InAs layer evolution is described by a generalization of Fick's law that employs

a chemical potential gradient (in lieu of a concentration gradient),[38] which takes into account the elastic energy of the strained InAs layer and the InAs/vapor and InAs/GaAs interfacial energies.[16,26]

The phase-field model was parameterized as follows. The interfacial energy and interfacial thickness between phase i and j are denoted γ_{ij} and ℓ_{ij}, respectively (see Table 3.III). The parameters W_{ij} and α_{ij} in the free energy functional F were determined using the relations $\ell_{ij} = \sqrt{2}\,\alpha_{ij}/\sqrt{W_{ij}}$ and $\gamma_{ij} = \alpha_{ij}\sqrt{W_{ij}}/3$ (see Table 3.III). The stiffness coefficients used for InAs and GaAs are listed in Table 3.II. The vapor phase is treated as an elastically compliant solid with $C_{ijkl}^{(1)} = 10^{-4} C_{ijkl}^{(2)}$. Based on the experimentally set deposition rate of 0.1 ML/s and surface diffusion coefficient D_S = 2.85×10^{-11} cm^2/s,[39,40] the phase-field deposition rate d = 0.00775 s^{-1} and adatom mobility coefficient $M_S = D_s\,/\,(\gamma\, l)$ = 6.19×10^{-25} m^5/(J s) were set in accordance with the analysis of Ref. 41. The governing equations were nondimensionalized using a characteristic energy density scale $E^* = W_{12}$ = 7.64×10^8 J/m^3, length scale for both the x and z direction, L = 78.1 nm and time scale τ = 12.9 s. The Cahn-Hilliard equation is solved using a Crank-Nicolson scheme in which the fourth-order evolution equation for φ_2 (the InAs layer) is split into two second-order equations for φ_2 and μ. The simulation domain is discretized using a dimensionless isotropic grid spacing $\Delta x = \Delta z = 0.025$, corresponding to the horizontal resolution of the AFM line-cuts ($\Delta x\, L = \Delta z\, L$ = 0.025 × 78.1 nm = 1.96 nm). As a result, the z grid spacing is too large to resolve the thickness of the initial experimental wetting layer. Consequently, the simulation results associated with film thickness and time scale of evolution should be interpreted qualitatively, and thus the simulated InAs layer thicknesses and simulation times are reported in their dimensionless form. On the other hand, we provide the results for lateral direction with physical unit (nm), as the features along that direction are well resolved and they arise from the actual substrate surface features.

Though this prevents fully quantitative comparison between simulation and experiment, the trends observed in simulations nonetheless provide important physical insights into QD evolution. The discretized equation for each time step ($\Delta t = 4\times10^{-3}$) is solved using a multi-grid method with Gauss-Seidel iterations.[42] No-flux boundary conditions are imposed in both x and z directions. Mechanical equilibrium is also solved iteratively using a multi-grid method with Gauss-Seidel smoothing,[43] with zero-displacement boundary conditions at the bottom, left and right sides of the computational domain, and a traction-free boundary condition at the top of the domain. The simulation is terminated at 6600 dimensionless time units (dtu).

3.5 Results and Discussion

3.5.1 Phase-field modeled InAs / GaAs QDs

For the flat and mounded surfaces, the simulated InAs layer thicknesses following deposition are shown in Figs. 3.2(a) and 3.2(e), respectively, while the AFM line-cuts used for the simulations are shown in Figs. 3.2(c) and 3.2(g), respectively.

3.5.1.1 Flat surface

For the flat surface, the InAs layer thicknesses following simulated deposition for 0, 4600, and 6600 dimensionless time units (dtu), are shown in Fig. 3.2(a), above the corresponding flat substrate line-cut in Fig. 3.2(c), as dashed, dot-dashed, and continuous lines, respectively. At the start of the simulation, the InAs thickness is set at 1.45 dimensionless length units (dlu). Following 4600 dtu of deposition, the formation of small QD nuclei with a linear density of 1.6×10^{5} cm^{-1} is apparent, marking the onset of the SK transition, at which point the wetting layer (WL) thickness is ~3.8 dlu, while the average QD nuclei height and diameter are respectively 1.3 ± 0.1 dlu and 48 ± 3 nm. The computed NN QD separations range from 51 nm to 76 nm, resulting in a computed

NN QD separation range of 43% of the average NN QD separation. After 6600 dtu, the WL thickness is reduced to ~3 dlu, while the QDs have grown to an average height and diameter of 6.3 ± 0.4 dlu and 46 ± 1 nm. The NN distances have values between 49 nm to 66 nm, resulting in a NN distance range of 30% of the average QD diameter. The reduced range of NN distances suggests the QDs evolved towards a more uniform placement on the flat substrate. The linear density of the QDs remains 1.6×10^5 cm^{-1}, which is similar to but clearly different from the measured average linear density of QDs of 1.0×10^5 cm^{-1}, computed using the average count of QDs crossed by 6 horizontal lines chosen at random positions on each AFM image, shown in Fig. 3.1(c). However, quantitative agreement is not expected in the case of isotropic QDs because the simulations assume a translational symmetry in the third direction (not included in the 2D simulation domain), which is inconsistent with isotropic morphology and distribution of the QDs grown on the flat surface. Therefore, the discussion below will be qualitative in nature.

To examine the details of QD evolution on the flat surface, we focus on four QDs in Fig. 3.2(b), whose position corresponds to the section of substrate shown immediately below in Fig. 3.2(d). In Fig. 3.2(b), solid arrows indicate the positions of QD nuclei, and dashed arrows indicate the height and position of the QD as they evolve following the nucleation at the onset of the SK transition at 4600 dtu. Following nucleation, some QD nuclei shift their position, as exemplified here by the QD nucleus marked by the open square, which appears to have nucleated on the top edge of a surface step, highlighted on the substrate in Fig. 3.2(b); however, by 6600 dtu, the QD (marked by the filled square) has moved towards the right, down the step, as indicated by the dashed arrow.

3.5.1.2 Mounded surface

For the mounded surface [Fig. 3.2(f, h)], the InAs layer thicknesses following simulated deposition for 0, 4400, and 6600 dtu, are shown in Fig. 3.2(e), above the corresponding mounded substrate line-cut in Fig. 3.2(g), as dashed, dot-dashed, and continuous lines, respectively. At the start of the simulation, the InAs layer thickness is again set at 1.45. Following 4400 dtu deposition, the formation of small QD nuclei with a linear density of 2.1×10^5 cm^{-1} marks the SK transition. In this case, the WL is ~4.1 dlu thick, while the average QD nuclei height is 0.28 ± 0.05. The NN distances have values between 14 nm and 59 nm, resulting in a NN distances range of 102% of the average NN distance, which is much larger than that of the QD nuclei on the flat surface (43%), suggesting increased non-uniformity of placement of the QD nuclei. After 6600 dtu, the QDs have grown to average height of 7.9 ± 0.5 dlu, while the WL has thinned to ~3.1 dlu, suggesting a net diffusion of In from the WL to the QDs. The nearest QD neighbor distances have values between 53 nm to 102 nm, resulting in a NN distances range of 72% of the average NN distance, which is again much larger than that of the QDs on the flat surface (30%), again suggesting increased non-uniformity of placement of the QDs. After 6600 dtu, the linear density of the QDs is 1.4×10^5 cm^{-1}, which is in agreement with the measured average linear density of QDs of 1.4×10^5 cm^{-1} shown in Fig. 3.1(d). While the difference between the QD densities at the onset of the SK transition (4600 dtu) and at 6600 dtu on the flat buffer is 0, the difference between QD density at the onset of the SK transition (4400 dtu) and at 6600 dtu on the mounded buffer is 0.7×10^5 cm^{-1}, which can be explained by coarsening, as predicted by established thermodynamic models.[44] Additionally, it is apparent that many QDs [marked by downward arrows in Fig. 3.2(e)] are positioned above substrate valleys [marked by upward arrows in Fig. 3.2(g)]. These valleys are more pronounced on the mounded buffer than those on the flat surface, and often occur on the edges of mounds.

Figure 3.2(f) shows a detail of Fig. 3.2(e), comprising three QDs formed above the substrate region in Fig. 3.2(g) following 6600 dtu of deposition. After nucleation, some of the original QD nuclei (marked by asterisks) disappear due to mass transport to the larger QDs, while other QD nuclei (marked by open triangles) shift their positions, resulting in the QDs marked by the filled triangles. It is apparent that those nuclei that have appeared on top of the lateral slopes of a mound, highlighted in Fig. 3.2(h), shift towards the bottom edge of the mound during growth, where the substrate presents a more pronounced concave curvature (marked by the semi-transparent curves).

3.5.1.3 Time evolution

We now examine the influence of the surface curvature on the length scale of the QDs, on the time evolution of the simulated InAs layer. Figure 3.3 shows the average InAs layer thickness as a function of time, for surface regions with curvatures ranging from -0.002 nm^{-1} to +0.002 nm^{-1} (corresponding to equivalent curvature radius $R \geq 500$ nm). The local substrate curvature κ_{GaAs} is calculated as:

$$\kappa_{\mathrm{GaAs}}(x) = \frac{z''_{\mathrm{GaAs}}(x)}{(1 + z'_{\mathrm{GaAs}}(x)^2)^{\frac{3}{2}}} \qquad 3.4$$

where $z_{\mathrm{GaAs}}(x)$ is the GaAs height profile, and $z'_{\mathrm{GaAs}}(x)$ and $z''_{\mathrm{GaAs}}(x)$ are the first and second derivative of $z_{\mathrm{GaAs}}(x)$. Note that $z''_{\mathrm{GaAs}}(x)$ provides distinction between valleys (positive values) and peaks (negative values). To obtain the local substrate curvature, for each value of x_i and $z_{\mathrm{GaAs}}(x_i)$, we utilize a portion of the substrate profile between $x_i - d\ /\ 2$ and $x_i + d\ /\ 2$, where d = 40 nm is the average diameter of the simulated QDs. This portion of the substrate $z_{\mathrm{GaAs}}([x_i - d/2, x_i + d/2])$ is fitted with a 4th order polynomial. The curvature value $\kappa_{\mathrm{GaAs}}(x_i)$ is then calculated using first and second derivatives algebraically obtained from the polynomial fit.

For the flat surface [Fig. 3.3(a)], the InAs thickness data, subdivided into two 0.002 nm^{-1} wide curvature bins over a curvature range of -0.002 nm^{-1} to +0.002 nm^{-1}, is shown as dashed and dot-dashed curves. The two curvature bins correspond, respectively, to low peaks and shallow valleys. In the earlier instants of the simulation (t < 4600 dtu), the average InAs layer thickness is independent of curvature, as shown by the overlap of the dashed and dot-dashed curves. When the InAs layer reaches the onset of the SK transition at 4600 dtu, which corresponds to 4.5 total average thickness, the lines for the $\kappa = (0,0.002]$ [45] nm^{-1} bin (dashed) and the $\kappa = [-0.002,0]$ nm^{-1} bin (dot-dashed) are no longer overlapping, as the average layer thickness increases (decreases) on regions with positive (negative) curvature. Thus, during the SK transition, there is a migration of In from surface regions with negative curvature (e.g., the apices of peaks) to surface regions with positive curvature (valleys), leading to curvature-driven diffusion.[46,47,48] This curvature-driven diffusion is responsible for inducing the formation of QD nuclei during the SK transition, in the absence of anisotropic surface stress, as In migrates from the WL to the QD. The resulting thinning of the WL above regions with negative curvature (peaks) is consistent with previous PFM simulations, in which the WL is found thinning at the shoulders of artificial mesas. After 6600 dtu, at which the InAs layer has 6.3 dlu total average thickness, the separation between the dashes and the dots-dashes has grown to 2 dlu, indicating that further curvature-driven diffusion has occurred.

For deposition on the mounded surface in Fig. 3.3(b), the InAs thickness data, subdivided into four 0.002 nm^{-1} wide curvature bins over a curvature range of -0.004 nm^{-1} to +0.004 nm^{-1} (corresponding to $R \geq 250$ nm), are represented by dotted, dashed, dot-dashed, and solid curves. The four bins correspond, respectively, to taller peaks, low peaks, shallow valleys and deeper valleys. In the earlier instants of the simulation (t < 4400 dtu), the average InAs layer thickness again is independent of curvature, as shown by the overlap of the dot, dashed, dot-dashed, and solid

curves. When the InAs layer reaches the onset of the SK transition at 4400 time, which corresponds to 4.3 average total thickness, the curves are no longer overlapping, as the average layer thickness increases (decreases) on surface regions with positive (negative) curvature. For the mounded surface, the separation between the dotted and the solid curves, after 6600 dtu deposition, corresponding to an average total thickness of 6.3 dlu, increases to 6.5 dlu, while the separation between the dashed and dot-dashed curves is 2 dlu. Thus, the curvature-driven diffusion is most significant from the highest peaks to the deepest valleys on the mounded surfaces. Interestingly, the onset of the SK transition also occurs earlier (4400 dtu) on the mounded surface in comparison to that of the flat surface (4600 dtu).

3.5.2 Polar pair correlation of InAs/AlGaAs quantum dots

The increase of the curvature-driven diffusion from wetting layer to QDs on the mounded surface provides the motivation to study the influence of the surface morphology on QD clustering. We noted above that regions of positive curvature (i.e. valleys) are predicted to function as preferential sites for QD placement. Since the edge of a mound is a region of positive curvature, we explore alignment of MBE-grown InAs/(Al, Ga)As QDs along mound edges using a 2D polar pair correlation function (PPCF) analysis of QD positions (See Appendix A.1). Taking an experimentally identified QD as the origin of a polar coordinate system, we subdivide the system into annular sections of $\Delta r = 0.1 \cdot d_{NN}$ and $\Delta\theta = \Delta r \,/\, r$, where d_{NN} is the average QD nearest neighbor distance. For each annular section, we count the number of QDs contained therein, and we divide the count by the area of the annular section, obtaining a polar coordinates-dependent local density ("polar density"). The computation of the polar density is repeated for each experimentally identified QD over several AFM images covering an area between 2 and 40 μm^2. The single QD-centered polar densities are all summed up and the result is divided by the total number of QDs,

obtaining an average over all QDs of the polar density. Finally, the average polar density is normalized by the overall average QD density, obtaining the 2D PPCF. A circularly symmetrical PPCF (i.e. independent of θ) suggests no significant alignment of QDs, while the presence of peaks in the PPCF for a given θ indicates a tendency for QDs to align in chains along that direction.

Using the mound lateral inclination angle to represent the "strength" of the mound-induced surface patterning, we compare 2D PPCF for a variety of mounded surfaces. In Fig. 3.4, we show PPCF of QDs on surfaces with mounds whose lateral inclination angle ranges from essentially 0° (flat GaAs surface from Fig. 3.1(c) and an $Al_{0.3}Ga_{0.7}As$ surface) to 5.1° [$Al_{0.3}Ga_{0.7}As$ surface from Fig. 3.1(h)]. The lateral inclination angles of 0.6° ($Al_{0.3}Ga_{0.7}As$ surface), 1.8° [mounded GaAs surface from Fig. 3.1(d)], 2.7° [$Al_{0.3}Ga_{0.7}As$ surface from Fig. 3.1(g)], 3.1° ($Al_{0.3}Ga_{0.7}As$ surface), and 4.9° studied here correspond to average terrace widths of 26 nm, 9 nm, 6 nm, 5 nm, and 3 nm, respectively. The average QD nearest-neighbor distance $\bar{r}_{NN}$ for Figs. 3.4(a, b, c, d, e, f, g) is, respectively, 58 nm, 54 nm, 55 nm, 33 nm, 89 nm, 175 nm, and 38 nm. For the flat GaAs and $Al_{0.3}Ga_{0.7}As$ surfaces in Fig. 3.4(a, b), we observe no dependence of PPCF on θ. For the mounded GaAs surface with lateral inclination angle 1.8° in Fig. 3.4(d), and the $Al_{0.3}Ga_{0.7}As$ surfaces with lateral inclination angle 0.6°, 2.7°, and 3.1°, in Fig. 3.4(c, e, f), the PPCF shows QD alignment for $\theta \approx 90°, 270°$ (vertical direction), consistent with QD chains positioned along the edges of mounds. For the mounded surface with lateral inclination angle 5.1° in Fig. 3.4(g), there appears to be several peaks around the center, with a faint elongation along the 90° and 270°, consistent with dense QD chains, all next to each other [see Fig. 3.1(h)]. Thus, vertical QD alignment appears on mounded surfaces, presumably due to the onset of curvature-driven diffusion from the WL to the QDs.

3.6 Conclusions

In summary, we have studied the influence of surface nano-patterning (mounds) on QD positioning, using a combined computational-experimental approach. For both flat and mounded surfaces, QDs nucleate via the SK transition. However, the SK transition occurs earliest on the mounded surfaces. Furthermore, for the mounded surface, QD growth is assisted by coarsening, with enhanced WL to QD transfer, and vertical alignment, indicating the significant role of curvature-driven diffusion. The surface mounds enable the spontaneous ordering of the QDs via curvature-driven diffusion. This approach is expected to be applicable to a wide variety of mounded surfaces.

3.7 Tables

Substrate	Mound inclination angle (°)	Terrace width (nm)	NN QD separation (nm)	2D QD density (10^{10} cm^{-1})	QD diameter (nm)
GaAs	0		58	2.4 ± 0.1	37 ± 5
AlGaAs	0		54	2.4 ± 0.1	27 ± 3
AlGaAs	0.6	26	55	2.2 ± 0.1	26 ± 4
GaAs	1.8	9	33	6.4 ± 0.2	27 ± 5
AlGaAs	2.7	6	89	0.8 ± 1	31 ± 7
AlGaAs	3.1	5	175	0.2 ± 1	28 ± 7
AlGaAs	5.1	3	38	9.2 ± 0.7	21 ± 6

Table 3.I. Mound inclination angle and relative terrace width, and average NN QD separation, 2D QD density, and QD diameter, for various substrates with varying mound inclination angles.

Parameter	Symbol	InAs ($p = 2$)	GaAs ($p = 3$)	$Al_{0.3}Ga_{0.7}As$
Lattice parameter (Å)	$a_0^{(p)}$	6.0583	5.65325[37]	5.6556[37]
Stiffness coefficients (GPa)	$C_{1111}^{(p)}$	83.3[17]	119[17]	-
	$C_{1122}^{(p)}$	45.3[17]	53.8[17]	-
	$C_{1212}^{(p)}$	39.6[17]	59.4[17]	-

Table 3.II. Materials parameters for GaAs, InAs, and $Al_{0.3}Ga_{0.7}As$.

Parameter	Symbol	vapor – InAs ($p = 1, q = 2$)	vapor – GaAs ($p = 1, q = 3$)	InAs – GaAs ($p = 2, q = 3$)
Interfacial energy (J/m^2)	γ_{pq}	0.704[49]	1.04[50]	0.100[51]
Interfacial thickness (nm)	ℓ_{pq}	3.91	3.91	3.91
Misfit strain (%)	η_0	-	-	7.17
Free energy barriers (J/m^3)	W_{pq}	7.64×10^8	1.13×10^9	1.08×10^8
Energy gradient coefficients (J/m)	α_{pq}^2	5.84×10^{-9}	8.60×10^{-9}	8.28×10^{-10}

Table 3.III. Parameters for phase-field model simulations.

3.8 Figures

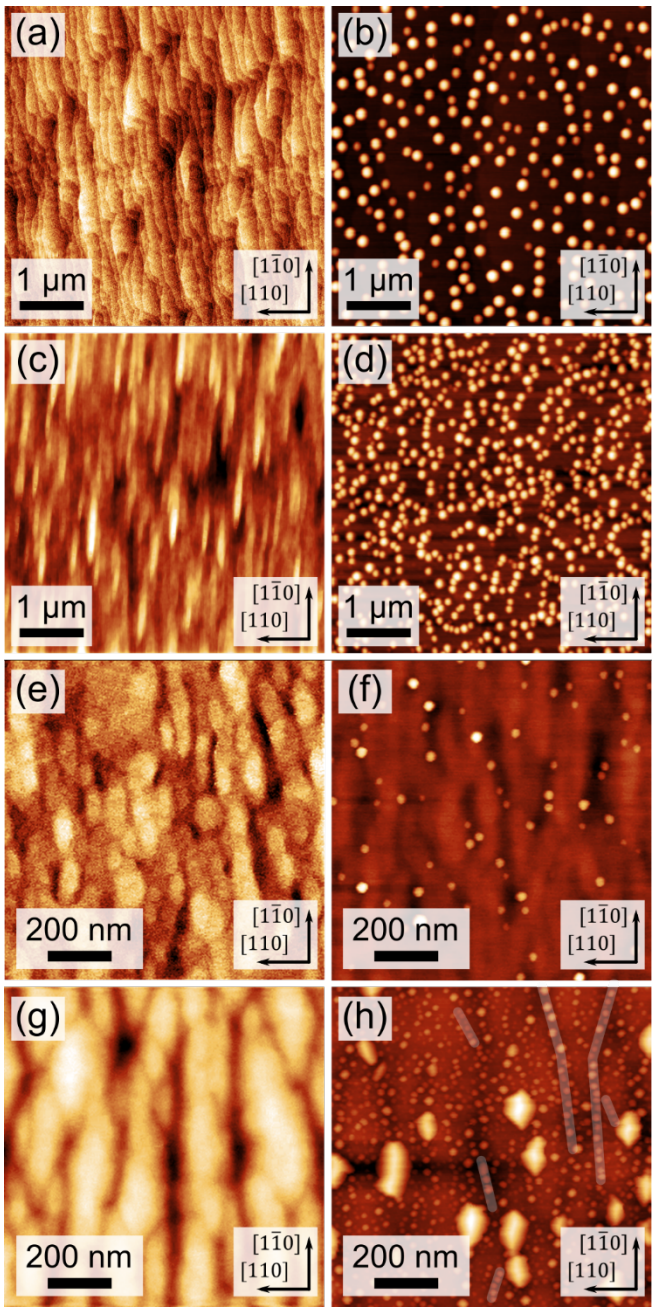

Figure 3.1: AFM topography images of flat and mounded (Al)GaAs buffer surfaces before/after InAs QD growth. (a)/(b) flat GaAs (mound angle = 0°), (c)/(d) GaAs (mound angle = 1.8°), (e)/(f) AlGaAs (mound angle = 2.7°), and (g)/(h) AlGaAs (mound angle = 5.1°). The color-scale ranges

displayed are (a) 2 nm, (b) 10 nm, (c) 6 nm, (d) 6 nm, (e) 4 nm, (f) 12 nm, (g) 10 nm, and (h) 20 nm. Chains of QDs are highlighted by semi-transparent lines.

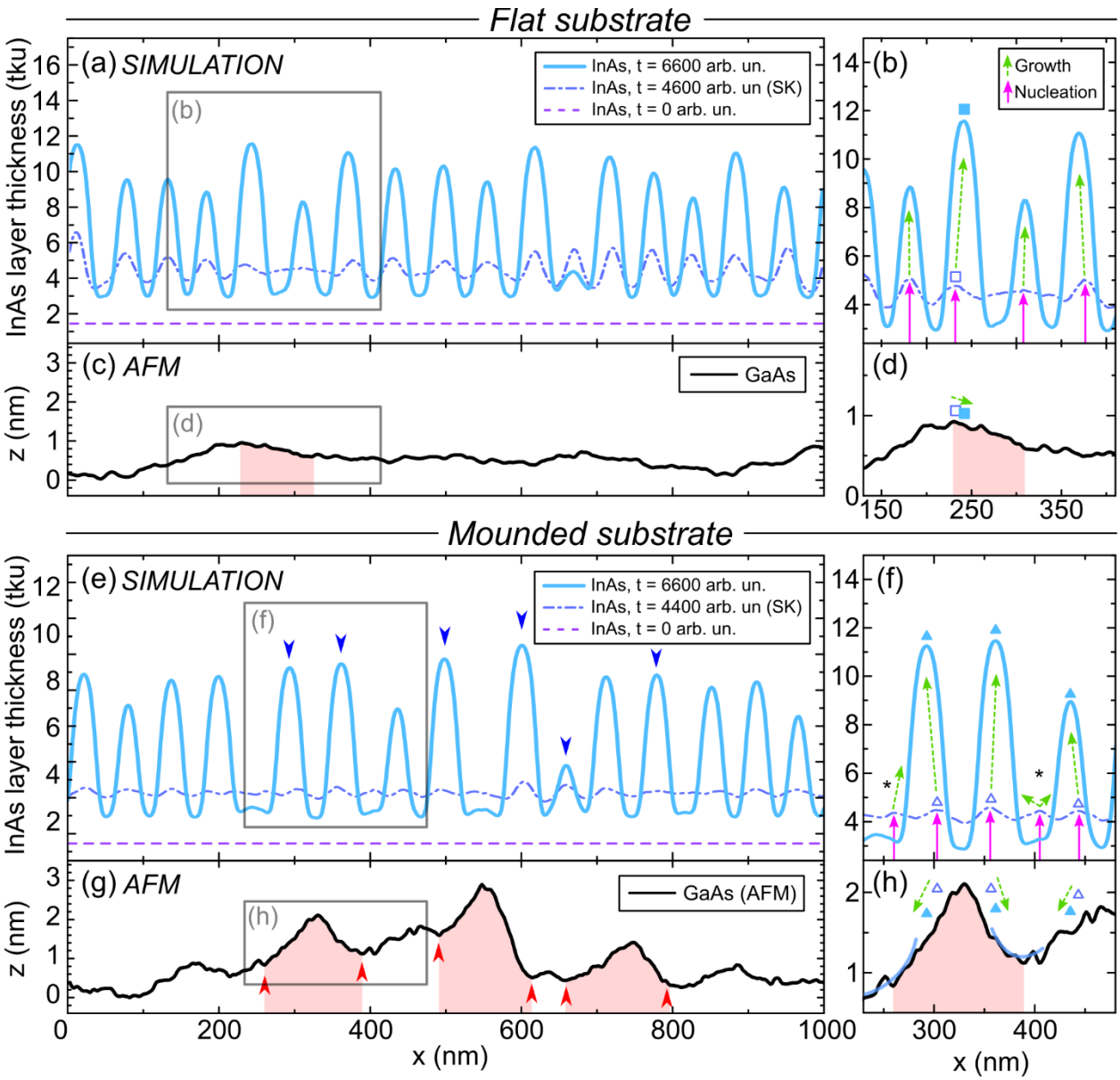

Figure 3.2: PFM-simulated InAs growth over AFM cross-section of flat and mounded GaAs surfaces. (a) Thickness of the InAs layer (above the flat GaAs substrate) from phase-field simulation after 6600 deposition time units (dtu) (solid line), after 4600 dtu (dot-dashed line), corresponding to the onset of the SK transition, and at the start of the simulation (dashed line). (b) A detail of (a), with solid arrows denoting nucleation of QDs at the SK transition, dashed arrows denoting the shift in position of the QDs during further deposition. The open and filled squares indicate the position of, respectively, a QD nucleus and of the QD resulting from the evolution of the QD

nucleus. (c) AFM line-cut of the flat surface. (d) Detail of (c) showing the portion of flat substrate corresponding to the sections of InAs layers in (b), with the shaded portion of the substrate indicating a step, the open square indicating the position of a QD nucleus, the filled square indicating the position to which the QD shifts during deposition, and the dashed arrow indicating the direction of the shift on the substrate. (e) Thickness of the InAs layer (above the mounded GaAs substrate) from phase-field simulation after 6600 dtu (solid line), after 4400 dtu (dot-dashed line), and at the beginning of the simulation (dashed line). Downward arrows mark QDs that end up positioned at the edge of mounds. (f) A detail of (e), with solid arrows denoting nucleation of QDs at the SK transition (open triangles), dashed arrows denoting the shift in position of the QDs during further deposition (filled triangles), and asterisks denoting QD nuclei that disappear due to coarsening. (g) AFM line-cut of the mounded surface, with shaded portions marking the mounds, and upward arrows marking the edges of the mounds. (h) Portion of the mounded surface in (g) corresponding to the sections of InAs layers in 2(f), with the shaded portion marking a mound, and curved lines indicating the positive curvature regions at the edge of the mound. The open and filled triangles mark, respectively, the positions of QD nuclei and the positions of QDs resulting from the evolution of the QD nuclei. The dashed arrows indicate the direction of the QD shift.

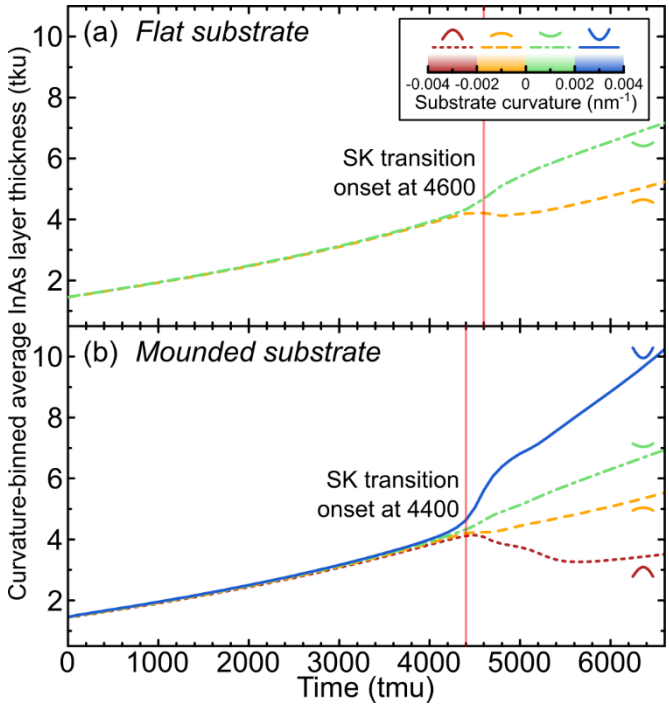

Figure 3.3: Evolution of the PFM-simulated InAs layer thickness in time for different local curvatures of the flat and mounded surface. (a) Evolution of the InAs layer thickness as a function of time for the flat surface, with the dashed line representing the average thickness of the InAs layer above regions of the substrate with curvature between -0.002 nm^{-1} and 0 nm^{-1} (low peaks), and the dot-dashed line representing the average thickness of the InAs layer above regions of the substrate with curvature between 0 nm^{-1} and 0.002 nm^{-1} (shallow valleys). (b) Evolution of the InAs layer thickness as a function of time for the mounded surface, with the dotted line representing the average thickness of the InAs layer above regions of the substrate with curvature between -0.004 nm^{-1} and -0.002 nm^{-1} (higher peaks), the dashed line representing the average thickness of the InAs layer above regions of the substrate with curvature between -0.002 nm^{-1} and 0 nm^{-1} (low peaks), the dot dashed line representing the average thickness of the InAs layer above regions of the substrate with curvature between 0 nm^{-1} and 0.002 nm^{-1} (shallow valleys), and the continuous line

representing the average thickness of the InAs layer above regions of the substrate with curvature between 0.002 nm^{-1} and 0.004 nm^{-1} (deeper valleys).

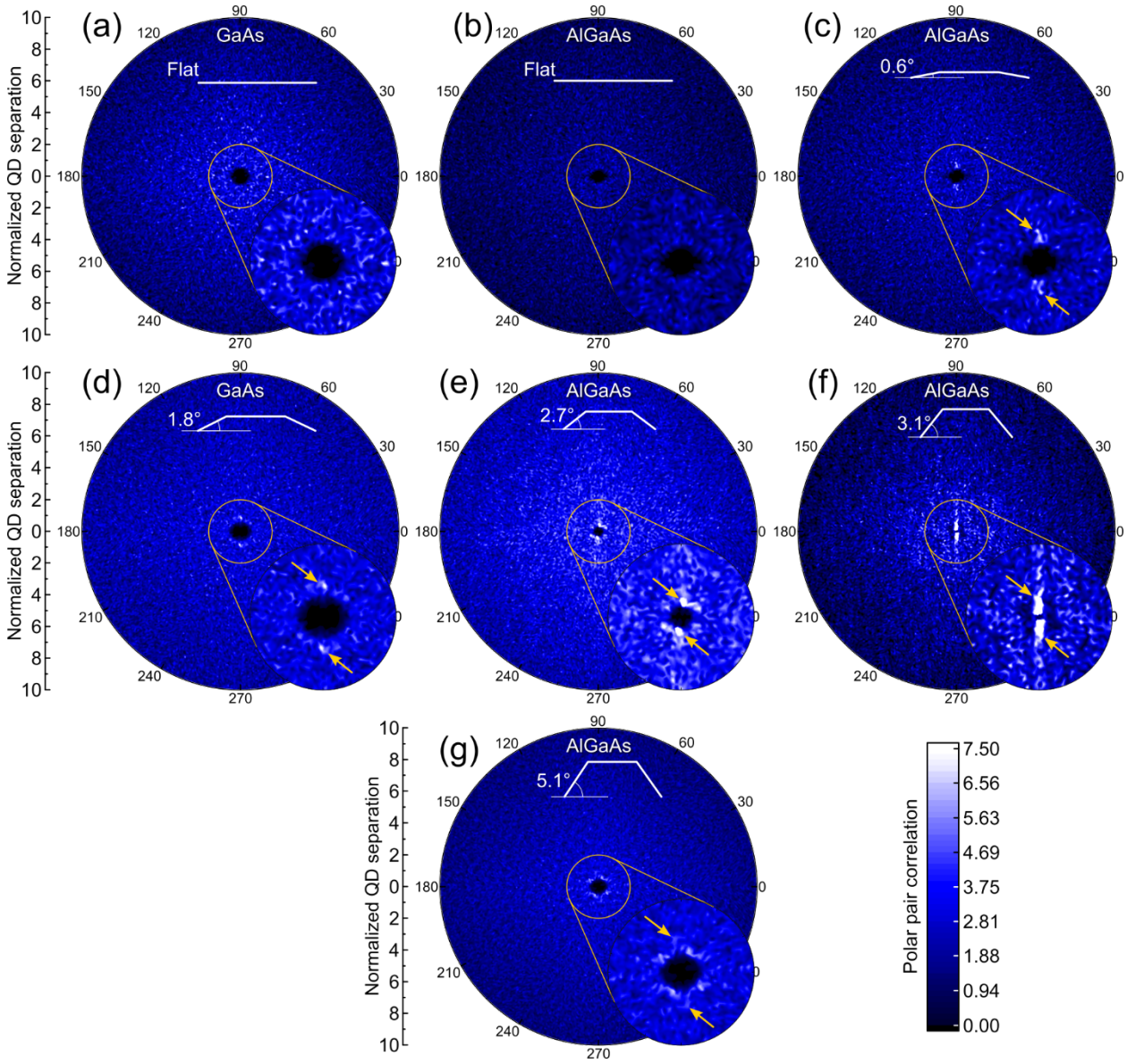

Figure 3.4: Polar pair correlation functions (PPCF) of the positioning of MBE-deposited InAs QDs on nano-patterned surfaces. The PPCF is represented here for QD separation from 0 to $10 \cdot d_{NN}$, with inset detail for QD separation from 0 to $2 \cdot d_{NN}$, for the following surfaces/mound inclination angles: (a) GaAs/flat, (b) $Al_{0.3}Ga_{0.7}As$/flat, (c) $Al_{0.3}Ga_{0.7}As$/0.6°, (d) GaAs/1.8°, (e) $Al_{0.3}Ga_{0.7}A$/2.7°, (f) $Al_{0.3}Ga_{0.7}A$/3.1°, (g) $Al_{0.3}Ga_{0.7}A$/5.1°.

3.9 References

[1] P. Bhattacharya and Z. Mi, "Quantum-Dot Optoelectronic Devices" Proc. IEEE **95**, 1723 (2007).

[2] A.D. Yoffe, "Semiconductor quantum dots and related systems: Electronic, optical, luminescence and related properties of low dimensional systems" Adv. Phys. 50, 1 (2001).

[3] A. Luque, A. Martí, E. Antolín, and C. Tablero, "Intermediate bands versus levels in non-radiative recombination" Physica B: Condensed Matter **382**, 320 (2006).

[4] T.C. Harman, P.J. Taylor, M.P. Walsh, and B.E. LaForge, "Quantum Dot Superlattice Thermoelectric Materials and Devices" Science **297**, 2229 (2002).

[5] N. Sritirawisarn, F.W.M. van Otten, and R. Nötzel, "Ordered 1-D and 2-D InAs/InP quantum dot arrays at telecom wavelength" J. Phys: Conf. Ser. **245**, 012004 (2010).

[6] Y. Lei, W. Cai, and G. Wilde, "Highly ordered nanostructures with tunable size, shape and properties: A new way to surface nano-patterning using ultra-thin alumina masks" Progress in Mat. Sci. **52**, 465 (2007).

[7] A. Karmous, A. Cuenat, A. Ronda, I. Berbezier, S. Atha, and R. Hull, "Ge dot organization on Si substrates patterned by focused ion beam" Appl. Phys. Lett. **85**, 6401 (2004).

[8] P. Atkinson, M.B. Ward, S.P. Bremner, D. Anderson, T. Farrow, G.A.C. Jones, A.J. Shields, and D.A. Ritchie, "Site-Control of InAs Quantum Dots using *Ex-Situ* Electron-Beam Lithographic Patterning of GaAs Substrates" Jpn. J. Appl. Phys. **45**, 2519 (2006).

[9] S.O. Kim, H.H. Solak, M.P. Stoykovich, N.J. Ferrier, J. J. de Pablo, P. F. Nealey, "Epitaxial self-assembly of block copolymers on lithographically defined nanopatterned substrates" Nature **424**, 411 (2003).

[10] J. Mayer, L.A. Giannuzzi, T. Kamino, and J. Michael, "TEM Sample Preparation and FIB-Induced Damage" MRS Bulletin **32**, 400 (2007).

[11] C.R.K. Marrian and D.M. Tennant, "Nanofabrication" J.Vac. Sci. Technol. A **21**, S207 (2003).

[12] K.G. Eyink, L. Grazulis, K. Mahalingam, J. Shoaf, V. Hart, D. Esposito, J. Hoelscher, M. Twyman, and D.H. Tomich, "Nanofabricated quantum dot array formation through annealing of nano-patterned planar InAs" J. Vac. Sci. Technol. B 30, 041806 (2012).

[13] V. Latini, E. Placidi, F. Arciprete, and F. Patella, "In-line correlation and ordering of InAs/GaAs multistacked Quantum Dots structures" J. Cryst. Growth **419**, 138 (2015).

[14] Z.M. Wang, K. Holmes, Y.I. Mazur, and G.J. Salamo, "Fabrication of (In,Ga)As quantum-dot chains on GaAs(100)" Appl. Phys. Lett. **84**, 1931 (2004).

[15] W. Ye, S. Hanson, M. Reason, X. Weng, and R.S. Goldman, "Control of InAs/GaAs quantum dot density and alignment using modified buffer layers" J. Vac. Sci. Technol. B 23, 1736 (2005).

[16] D.J. Seol, S.Y. Hu, Z.K. Liu, L.Q. Chen, S.G. Kim, and K.H. Oh, "Phase-field modeling of stress-induced surface instabilities in heteroepitaxial thin films" J. Appl. Phys. **98**, 044910 (2005).

[17] K.H. Hellwege and O. Madelung, Semiconductors: *Physics of Group IV Elements and III–V Compounds* (Springer-Verlag, 1991).

[18] M.E. Thompson, C.S. Su, and P.W. Voorhees, "The equilibrium shape of a misfitting precipitate" Acta Met. Mater. **42**, 2107 (1994).

[19] B. Yang, F. Liu, and M. G. Lagally, "Local Strain-Mediated Chemical Potential Control of Quantum Dot Self-Organization in Heteroepitaxy" Phys. Rev. Lett. **92**, 025502 (2004).

[20] E. Zallo, P. Atkinson, A. Rastelli, and O. G. Schmidt, "Controlling the formation of quantum dot pairs using nanohole templates" J. Cryst. Growth **338**, 232 (2012).

[21] C. Orme, M.D. Johnson, J.L. Sudijono, K.T. Leung, and B.G. Orr, "Large scale surface structure formed during GaAs (001) homoepitaxy" Appl. Phys. Lett. **64**, 860 (1994).

[22] F. Patella, F. Arciprete, E. Placidi, S. Nufris, M. Fanfoni, A. Sgarlata, D. Schiumarini, and A. Balzarotti, "Morphological instabilities of the InAs/GaAs(001) interface and their effect on the self-assembling of InAs quantum-dot arrays" Appl. Phys. Lett. **81**, 2270 (2002).

[23] F. Arciprete, E. Placidi, R. Magri, M. Fanfoni, A. Balzarotti, and F. Patella, "The Unexpected Role of Arsenic in Driving the Selective Growth of InAs Quantum Dots on GaAs" ACS Nano **7**, 3868 (2013).

[24] F. Arciprete, E. Placidi, R. Magri, D. Del Gaudio, and F. Patella, "Kinetically driven selective growth of InAs quantum dots on GaAs" J. Mat. Res. 28, 3201 (2013).

[25] J.H. Lee, Z.M. Wang, B.L. Liang, K.A. Sablon, N.W. Strom, and G.J. Salamo, "Size and density control of InAs quantum dot ensembles on self-assembled nanostructured templates" Semicond. Sci. Technol. 21, 1547 (2006).

[26] M. Salvalaglio, R. Backofen, R. Bergamaschini, F. Montalenti, and A. Voigt, "Faceting of Equilibrium and Metastable Nanostructures: A Phase-Field Model of Surface Diffusion Tackling Realistic Shapes" Cryst. Growth Design **15**, 2787 (2015).

[27] K.R. Elder, Z.-F. Huang, and N. Provatas, "Amplitude expansion of the binary phase-field-crystal model" Phys. Rev. E **81**, 011602 (2010).

[28] Y. Ni, L.H. He, and A.K. Soh, "Three-dimensional phase field simulation for surface roughening of heteroepitaxial films with elastic anisotropy" J. Cryst. Growth **284**, 281 (2005).

[29] L.K. Lee, L.K. Aagesen, K. Thornton, and P.-C. Ku, "Origin of broad luminescence from site-controlled InGaN nanodots fabricated by selective-area epitaxy" Phys. Status Solidi A **211**, 531 (2014).

[30] L.K. Aagesen, M.E. Coltrin, J. Han, and K. Thornton, "Phase-field simulations of GaN growth by selective area epitaxy from complex mask geometries" J. Appl. Phys. **117**, 194302 (2015).

[31] J.J. Eggleston and P.W. Voorhees, "Ordered growth of nanocrystals via a morphological instability" Appl. Phys. Lett. **80**, 306 (2002).

[32] G. Haugstad, Atomic Force Microscopy, Ch. 8 p. 369 (Wiley, Hoboken NJ, 2012)

[33] M. Ohmori, T. Kawazu, K. Torii, T. Takahashi, and H. Sakaki, "Formation of Ultra-low Density ($\leq 10^4$ cm^{-2}) Self-Organized InAs Quantum Dots on GaAs by a Modified Molecular Beam Epitaxy Method" Appl. Phys. Exp. **1**, 061202 (2008).

[34] D. Nečas, P. Klapetek, "Gwyddion: an open-source software for SPM data analysis" Open Phys. **10**(1), 181 (2012).

[35] J. Jost, Partial Differential Equations, (Springer, New York, 2013)

[36] S.M. Wise, J.S. Lowengrub, J.S. Kim, and W.C. Johnson, "Efficient phase-field simulation of quantum dot formation in a strained heteroepitaxial film" Superlattices and Microstructures **36**, 293 (2004).

[37] I. Vurgaftman, J.R. Meyer, and L.R. Ram-Mohan, "Band parameters for III–V compound semiconductors and their alloys" J. Appl. Phys. **89**, 5815 (2001).

[38] A. G. Lamorgese, D. Molin, and R. Mauri, "Phase Field Approach to Multiphase Flow Modeling" Milan J. Math. **79**, 597 (2011).

[39] J.H. Neave, P.J. Dobson, B.A. Joyce, and J. Zhang, "Reflection high-energy electron diffraction oscillations from vicinal surfaces—a new approach to surface diffusion measurements" Appl. Phys. Lett. **47**, 100 (1985).

[40] H. Toyoshima, T. Shitara, P.N. Fawcett, J. Zhang, J.H. Neave, and B.A. Joyce, "In adatom migration studies by reflection high-energy electron diffraction oscillations on vicinal InAs(001) surfaces" J. Appl. Phys. **73**, 2333 (1993).

[41] S.M. Wise, J.S. Lowengrub, J.S. Kim, and W.C. Johnson, Superlattices and Microstructures **36**, 293 (2004).

[42] G.H Golub and C.F. Van Loan, Matrix Computations (Johns Hopkins University press, 1996).

[43] M. Adams, M. Brezina, J. Hua, and R. Tuminaro, "Parallel multigrid smoothing: polynomial versus Gauss–Seidel" J. Comp. Phys. **188**, 593 (2003).

[44] V. Shchukin, E. Schöll, P. Kratzer, "Thermodynamics and Kinetics of Quantum Dot Growth," in Semiconductor Nanostructures. NanoScience and Technology, edited by D. Bimberg. (Springer, Berlin, Heidelberg 2008) pp 1-39.

[45] Here we employ the conventional notation whereby a round bracket denotes that the adjacent endpoint is excluded from the set, while a square bracket denotes that the adjacent endpoint is included in the set. E.g., $(a, b] = \{x \in R \,|\, a < x \leq b\}$. Thus, those InAs layer thicknesses above zero curvature substrate regions are binned in the low peaks bin (curvature values from -0.002 nm^{-1} to 0 nm^{-1}).

[46] E. Placidi, F. Arciprete, V. Latini, S. Latini, R. Magri, M. Scuderi, G. Nicotra, and F. Patella, "Manipulating surface diffusion and elastic interactions to obtain quantum dot multilayer arrangements over different length scales" Appl. Phys. Lett. **105**, 111905 (2014).

[47] Q. Xie, A. Madhukar, P. Chen, and N.P. Kobayashi, "Vertically Self-Organized InAs Quantum Box Islands on GaAs(100)" Phys. Rev. Lett. **75**, 2542 (1995).

[48] C. Herring, in The Physics of Powder Metallurgy Ch. 8 p. 149 (McGraw-Hill, New York, 1951).

[49] E. Pehlke, N. Moll, A. Kley, and M. Scheffler, "Shape and stability of quantum dots" Appl. Phys. A, **65**, p.525 (1997).

[50] N. Moll, A. Kley, E. Pehlke, and M. Scheffler, "GaAs equilibrium crystal shape from first principles" Phys. Rev. B **54**, 8844 (1996).

[51] M. Ohring, Materials Science of Thin Films: Deposition and Structure (Academic Press, 2002).

Chapter 4: Morphological Design of Complex Oxides During Pulsed-Laser Deposition – the Role of Plasma-Plume Expansion

4.1 Overview

In this chapter, we examine the influence of plasma expansion dynamics on the resulting morphology of indium oxide – tin oxide layers during pulsed-laser deposition. The objective of this work is to identify the influence of plasma dynamics the selection of a film vs. nanowires growth mode. This work highlights a more detailed understanding of the role of plasma dynamics in the formation of vapor-liquid-solid nanowires during pulsed-laser deposition.

We begin the chapter reviewing earlier literature observing the formation of tin-doped indium oxide nanowires during pulsed-laser deposition, noting the current lack of understanding of the mechanisms leading to the selection of nanowires vs. film growth mode. Next, the experimental methods used to obtain tin-doped indium oxide layers during pulsed-laser deposition with varying N_2 atmosphere pressures and laser pulse frequencies are described. For the lowest N_2 pressure, indium-tin droplet formation, followed by self-catalyzed VLS growth, is observed. With increasing N_2 pressure, a transition from VLS to VS growth is apparent. It is hypothesized that oxygen scattering at the lowest N_2 pressure induces a metal-rich plume which leads to metal droplet formation, followed by VLS growth. As the N_2 pressure is increased, the plasma-plume and its metal-rich core are compressed, resulting in a transition to VS growth. This tunable compression of the plasma-plume offers a route to morphological design of a wide range of functional complex oxide devices with tunable optical and electronic performance.

The work described in this chapter was peer-reviewed and published in D. Del Gaudio, C.T. Boone, K. Sallans, E. Mason, A.J. Williamson, S. Yarlagadda, Y. Turkulets, J.T. Heron, I. Shalish, and R.S. Goldman, "Morphological design of complex oxides during pulsed-laser deposition: The role of plasma-plume expansion" Journal of Applied Physics **126**, 184301 (2019).

4.2 Background

Nanometer-scale materials have been identified as promising candidates for thermoelectric (TE) devices with high figure-of-merit, $ZT = \frac{S^2 \sigma T}{\kappa}$, where S is the Seebeck coefficient (thermopower), T is the temperature, and $\sigma(\kappa)$ is the electrical (thermal) conductivity. In the framework of the phonon-glass/electron-crystal concept, ZT can be increased by reducing the dimensionality of materials. Indeed, 1D conductors, in which electrons are restricted to a narrow energy range, are predicted to enable TE energy conversion efficiencies approaching the Carnot limit.

Due to its high transparency and conductivity, tin-doped indium oxide (ITO) has been used as an electrode in solar cells, flat panel displays, Li-ion batteries, and light-emitting diodes (LEDs).[1] The high surface to volume ratios of ITO nanowire (NW) arrays, is expected to lead to enhanced performance of numerous devices including solar cells,[2,3] gas sensors,[4,5] field emitters,[6] photodetectors,[7,8] photo-electrochemical cells,[9] and high-density memory devices.[10] ITO has recently been shown to possess strong non-linear optical properties for near-infrared wavelengths, where its permittivity is vanishingly small (an epsilon-near-zero material).[11] ITO layers are typically prepared by sputtering, but this method requires post-deposition annealing to tailor the transparency and conductivity, which depend strongly on crystallinity and morphology. Using pulsed laser deposition (PLD), both high transparency and high conductivity can be achieved without annealing, thus extending the applicability of ITO to alternative substrates such as polymers and plastic. During PLD, control of the morphology to achieve vapor-liquid-solid (VLS) and vapor-

solid (VS) growth has been reported,[12,13] typically via the selection of inert vs. reactive gas species and/or tuning of the partial pressure. To date, the relative roles of Stranski Krastanow-like and vapor-liquid-solid growth during this morphological transition remains controversial.

Here, we report on PLD of ITO in an inert atmosphere, identifying the role of the plasma-plume expansion in the selection of VLS vs. VS growth. For the lowest N_2 pressure, oxygen scattering yields a metal-rich plume leading to metal droplet formation, which facilitates VLS growth. As the N_2 pressure is increased, the lateral plasma-plume compression is identified as the mechanism leading to a recovery of the oxygen rich stoichiometry, resulting in a transition to VS growth. This approach to morphological design is applicable to a wide range of functional complex oxides.

A further avenue of TE power factor enhancement is the transport of carriers through double barrier hetero-structures such as those in nanowire (NW) super-lattices (SLs), in which thermal transport is suppressed through phonon scattering. Although the growth of NW hetero-structures is well established, the growth of artificial SL NWs has only been demonstrated using tedious methods involving alternating depositions. Here, self-assembly of SLs during NW growth through spontaneous phase separation of In_2O_3 and SnO_2 is pursued by employing indium oxide-tin oxide, or indium-tin mixtures with increasing tin content.

4.3 Methods

Pulsed laser deposition (PLD) was performed using a 248 nm KrF excimer laser with 20 ns pulse width. In preparation for PLD, sapphire substrates were sequentially sonicated in trichloroethylene, acetone, and isopropyl alcohol, followed by drying in N_2 gas. The substrates were subsequently attached to an Inconel platen using silver paint cured on a hot plate for 4 minutes at 90 °C. Following cooling, the substrates were inserted into a load-lock and transferred into the PLD growth chamber with base pressure in the range 5×10^{-7} – 5×10^{-6} Torr. During the pumping

down of the load-lock, targets consisting of 90-10 weight % In_2O_3-SnO_2 (ITO), 46-54 weight % In_2O_3-SnO_2 (hyper-eutectoid ITO), and 52-48 weight % In-Sn (eutectic InSn) were pre-ablated for 5 minutes.

For PLD of ITO (see Appx. D.2.1), we use an inert atmosphere (99.999% pure N_2) and 12,000 laser pulses with energy ~70 mJ and spot size ~0.09 cm^2, resulting in a fluence of ~0.8 J/cm^2, with a target-substrate separation of 7 cm, and substrate temperature of 550 °C, similar to earlier studies,[12,13] several ITO layers were prepared using N_2 gas pressures, p_{N_2}, in the range 7 to 740 mTorr, and pulse frequencies, f_{pulse}, in the range 2.5 to 10 Hz. For these conditions, the plasma plume spans approximately 1/3 to 1/2 of the target-substrate separation. Following deposition, power to the substrate heater was turned off, and the samples were allowed to cool in the N_2 inert atmosphere; in other words, the ITO target is the primary source of oxygen. We refer to those prepared at p_{N_2} < 100 mTorr and p_{N_2} > 100 mTorr as LoP and HiP, respectively. We also refer to those prepared with f_{pulse} < 6 Hz and f_{pulse} > 6 Hz as LoF and HiF, respectively.

For PLD of hyper-eutectoid ITO (see Appx. D.2.3), we use an inert atmosphere (99.999% pure N_2) at 78 mTorr and 24,000 laser pulses with frequency 2.5 Hz with energy 97 mJ and spot size 0.04 cm^2, resulting in a fluence of 2.4 J/cm^2, with a target-substrate separation of 7 cm, and substrate temperature of 600 °C. Following deposition, power to the substrate heater was turned off, and the samples were allowed to cool in the N_2 inert atmosphere.

For PLD of eutectic InSn (see Appx. D.2.4), we use a reactive atmosphere (99.999% pure O_2) at 0.11 mTorr and 12,000 laser pulses with frequency 10 Hz, energy 154 mJ and spot size 0.05 cm^2, resulting in a fluence of 3.1 J/cm^2, with a target-substrate separation of 7 cm, and substrate temperature of 500 °C. Following deposition, power to the substrate heater was turned off, and the samples were allowed to cool in the O_2 reactive atmosphere.

For each set of conditions, multiple samples were prepared. For most samples, the crystallinity and surface morphology were examined using θ-2θ x-ray diffraction (XRD) with Cu Kα_1 radiation, scanning-electron microscopy (SEM) using an FEI XL30 SEM, and atomic-force microscopy (AFM) using a Veeco Dimension Icon AFM.

4.4 Results and Discussion

4.4.1 VLS growth of ITO

Figure 4.1 shows a schematic of the VLS growth mode for the case of the deposition of the 90-10 wt.% In_2O_3-SnO_2 compound, also known as indium-tin oxide (ITO), discussed in this dissertation. Figure 4.1(a) shows the ternary phase diagram for In-Sn-O at 600 °C,[14,15] consistent with the growth temperatures used in this work, which were in the range of 550 – 600 °C for ITO. The three circled numbers indicate the stages of VLS growth of ITO NW and are placed on the phase diagram to reflect the approximate composition of the seed droplet. Figure 4.1(b) shows a morphological schematic of the stages of growth marked on the phase diagram in 4.1(a).

Following the stages outlined in Fig. 4.1, the growth proceeds as follows: ① the initial liquid InSn alloy droplet is formed. The composition of the InSn alloy is 90-10 wt.% In-Sn, representing the same In-Sn ratio as in ITO. ②, with continuing incoming In, Sn, and O fluxes, O begins to dissolve in the InSn droplets and the O content of the droplet increases until the droplet is super-saturated and ITO crystals begin to nucleate.[16] In terms of the ternary phase diagram in 4.1(a), the composition of the droplet has reached the edge of the "In_2O_3 (s) + InSn (l)" phase region. As the saturation of O is further increased, the composition of the droplet completely crosses into the "In_2O_3 (s) + InSn (l)" phase region (stage ③), resulting in the continued formation and precipitation of ITO crystals, which aggregate into a single crystal at the base of the droplet.[17,18]

As long as the supply of In, Sn and O is not interrupted, ITO crystals continue to form within the supersaturated InSn droplet, and they continue to precipitate at the base of the droplet, forming a single crystal ITO column of, in principle, arbitrary length, and diameter comparable to the diameter of the catalyst droplet.

4.4.2 Influence of process gas pressure on ITO morphology

In Fig. 4.2, we show representative (a) x-ray diffraction spectra, corresponding SEM images of (b) LoF + LoP (2.5 Hz, 77 mTorr), (c) HiF + LoP (10 Hz, 7 mTorr), and (d) HiF + HiP (10 Hz, 740 mTorr) samples and AFM images of (f) HiF + HiP (10 Hz, 740 mTorr) samples, in comparison with (e) x-ray diffraction spectra from the ITO target and an ITO reference. For the ITO target [Fig. 4.2(e)], the observed reflections and their relative intensities are similar to those of the ITO reference[19] in Fig. 4.2(e). In both cases, the 2 2 2 reflection has the highest intensity, followed in order of decreasing intensity by 4 0 0 and 4 4 0, and 2 1 1 and 6 2 2.

For the deposited layers, the prominent reflection at $2\theta = 41.675°$ corresponds to the 0 0 0 6 reflection of Al_2O_3, as expected for a c-plane sapphire substrate.[20] In addition, prominent reflections at $2\theta = 17.50°$, 30.56°, 35.43°, 39.78°, and 54.32°, corresponding to the 2 0 0, 2 2 2, 4 0 0, 4 2 0, and 6 0 0 reflections of the ITO reference in Fig. 4.2(e), indicate that crystalline ITO is present in all layers. Since the intensity of the 4 0 0 reflection is considerably higher than that of the 2 2 2 reflection, the layers are preferentially oriented with the [1 0 0] direction normal to the surface of the substrate, consistent with earlier reports.[1,13]

We now consider the SEM images in Figs. 4.2(b) - 4.2(d) and the AFM image in Fig. 4.2(f). In Fig. 4.2(b), arrays of upright nanowires (NWs) (length = 1.0 ± 0.1 μm; diameter = 40 ± 10 nm) with spherical tips, characteristic of VLS growth, are observed. In Fig. 4.2(c), arrays of tapered NWs (length = 700 ± 100 nm; diameter decreasing from 190 ± 10 nm to 80 ± 10 nm) with spherical

tips, are observed. In some samples grown in LoF + LoP conditions, branching of the NW was observed, consistent with earlier reports.[1,12,13] The arrays of tapered NWs also contain a sparse concentration of nanoparticles (NPs), suggesting a contribution of VS growth in that case. Finally, in Figs. 4.2(d) and 4.2(f), arrays of pyramidal grains, 70 to 570 nm in diameter, due to VS growth, are apparent.

To quantify and compare the preferential orientations of the layers, we compute the texture coefficient $P(\boldsymbol{h}_i)$ for each detected reflection (See Appx. A.3). The texture coefficients computed for all observed reflections are shown in Table 4.I. For all layers, the texture coefficients for 2 0 0, 4 0 0, and 6 0 0 reflections exceed 1, while those for all the others are less than 1, indicating a preferential [1 0 0] orientation.

To evaluate the fraction of crystallites with a preferential vertical [1 0 0] orientation, we compute the orientation fraction (See Appx. A.3). For the arrays of straight NWs, tapered NWs, and pyramidal grains, the [1 0 0]-orientation-fractions are 0.40 ± 0.15, 0.55 ± 0.17, and 0.55 ± 0.18, respectively. The similarities in [1 0 0]-orientation-fractions across morphologies might be indicate that orientation selection is determined by the [0 0 0 1]-oriented sapphire substrate. However, the lack of mutually aligned feature edges suggests the absence of ITO/sapphire epitaxy. Instead, the preferred [0 0 1] texture is likely determined by the minimization of interface energy, as supported by reports of preferred texture for NWs grown on Si or glass in Refs. 1, 12 and 13.

4.4.3 Pressure-induced growth mode switching: a model

To explain the morphological evolution of the ITO layers, we consider the dynamics of the plasma-plume, as shown schematically in Fig. 4.3. For the LoP case, shown in Fig. 4.3(a), while the laser-ablated ITO plasma-plume expands, indium (115 amu), tin (119 amu), and oxygen (16 amu) are subject to collisions with the N_2 gas (28 amu). Due to the significant imbalance in masses

between the metals (indium and tin) and the gases (oxygen and N_2), collisions with N_2 yield significant scattering of oxygen but negligible scattering of (the more massive) indium and tin, leading to the formation of a metal-rich plume core.[21,22] Once the plasma-plume reaches the substrate, the excess metal condenses into droplets that act as seeds for VLS NW growth.

For the HiP case shown in Fig. 4.3(b), on the other hand, oxygen dispersion due to collisions with N_2 is hindered by N_2 pressure-induced plume compression, resulting in a decrease in excess metal concentration at the plume core.[23] Interestingly, both lateral plume confinement and high density fronts (shock-waves) have been previously observed within the plasma-plume. However, their potential connection to morphological design has not yet been realized.[24]

The morphology is also influenced by the diffusion of adsorbed metallic species (in this case, indium and tin) on the surface. To examine the effect of the plasma-plume expansion dynamics on the diffusion of adsorbed species, we consider the hydrodynamic model[25] of the evolution of the velocity v_{plume} of the plasma-plume front in time t: $v_{\text{plume}} \propto p^{-1/5} t^{-3/5}$. Thus, with increasing pressure, p, the plasma-plume expansion is slowed. The slower plasma-plume expansion leads to lower kinetic energy for the atoms in the plasma, which induces lower diffusion rates. Thus, at low pressures, higher kinetic energy promotes condensation of metallic droplets, and, consequently, VLS growth. Conversely, at high pressures, the lower diffusion rate promotes crystallization of the ITO, rather than the formation of droplets, consistent with our observations.

Surface diffusion may also be enhanced by an increase in time between laser pulses (i.e. a reduced pulse frequency), or, vice-versa, surface diffusion may be reduced by an increased pulse frequency. For LoF, the adsorbed species enable droplet nucleation and coalescence, followed by

VLS growth. Conversely, for the HiF case, the adsorbed species are unable to coalesce into droplets, while the higher oxygen supply rate favors metal-oxygen reaction and subsequent VS growth.[26]

The combined influences of the plasma-plume expansion and the subsequent diffusion of adsorbed species are illustrated in Fig. 4.4. For LoP + LoF, the metal-rich plasma-plume and low pulse frequency enable the formation of metal droplets, which act as catalysts as they become super-saturated with O, as shown in Fig. 4.4(a). The InSn alloy in the droplets reacts with the O, forming ITO, which precipitates at the nano-droplet/substrate interface, as shown in Fig. 4.4(b). With subsequent laser pulses, the ITO continues to be deposited at the base of the nano-droplets, inducing the formation of a column of high-quality ITO crystal, in the classic VLS growth mode. Indeed, as shown in Fig. 4.4(c), a dense array of high-aspect-ratio NWs, with spherical tips, consistent with the VLS growth mode, is apparent.

For the LoP + HiF case, the plasma-plume is metal-rich but the droplet nuclei are exposed to additional oxygen due to the frequent laser pulses. Consequently, in the early stages, as shown in Fig. 4.4(d), condensation of indium and tin leads to metal nano-droplet formation, while frequent laser pulses lead to local oxygen-environments that promote the nucleation of 3D ITO islands. With subsequent laser pulses, the droplets give rise to VLS growth as in Fig. 4.4(c), and the 3D islands grow to form pyramidal grains in the VS growth mode. Additionally, the onset of VS growth causes additional lateral deposition of ITO on the NW walls, i.e. lower portions of the NW stem (base) are subject to the lateral ITO growth for longer time than later sections of the NW stem (top), leading to the formation of tapered NWs. In Fig. 4.4(f), the formation of tapered NW with spherical tips, and pyramidal grains among the NW are apparent.

For the HiP + HiF case, due to the reduced lateral expansion of the plasma-plume, negligible excess metal is in contact with the sapphire substrate. The local oxygen-rich environment promotes the nucleation of 3D ITO islands, as shown in Fig. 4.4(g). With subsequent laser pulses, the VS growth of islands leads to the characteristic columnar growth that has been previously observed in several metal oxides,[27] as shown in Fig. 4.4(h). Indeed, in the line-cut from the AFM image in Fig. 4.2(f), shown in Fig. 4.4(i), pyramidal grains, consistent with pure VS growth, are apparent. Since the high-pressure-induced local oxygen-rich environment appears to govern the selection of VS vs. VLS growth, similar results are expected for the HiP + LoF case.

4.4.4 Influence of target composition on ITO morphology

In Fig. 4.5 we show (a) x-ray diffraction spectra and corresponding SEM images of NW obtained by (b) deposition of ITO in N_2, (c) deposition of hyper-eutectoid ITO in N_2, and (d) deposition of eutectic InSn in O_2. For all the XRD spectra in Fig. 4.5(a), the prominent reflection at $2\theta = 41.675°$ corresponds to the 0 0 0 6 reflection of Al_2O_3, while the reflections at $2\theta = 30.56°$ and 35.43° correspond to the 2 2 2 and 6 0 0 reflections of ITO (see Fig. 4.2 and Refs. 19 and 20). For the hyper-eutectoid ITO NW, the broadening of the peaks corresponding to the 2 2 2 and 4 0 0 reflections of ITO is presumably attributable to the mis-orientation and crystal defects of the NWs [see Fig. 4.5(c)]. For the eutectic InSn NW, an additional peak at $2\theta = 32.15°$ is present, corresponding to the 1 0 1 reflection of SnO_2, suggesting possible In_2O_3-SnO_2 phase separation.

We now consider the SEM images in Figs. 4.5(b-d). In Fig. 4.5(b) (ITO deposition), the same array of upright NW with spherical tips as in 4.2(b) is shown. In Fig. 4.5(c) (hyper-eutectoid deposition), shrub-like arrays of kinked NW growing at random orientations with varying lengths (1 – 3 μm) and diameters (100 – 200 nm) are observed. In Fig. 4.5(d) (eutectic InSn deposition in

O_2), arrays of high-aspect ratio upright branched NW (trunk length = 1.0 ± 0.2 μm; trunk diameter = 50 ± 20 nm) among smooth lenticular particles (diameter = 200 – 800 nm) are observed.

4.5 Summary and Conclusions

In summary, we have examined the morphological design of complex oxides during PLD in an inert atmosphere, identifying the role of the plasma-plume expansion on VLS vs. VS growth. For the lowest pressure, oxygen scattering induces a metal-rich plasma core, leading to the coalescence of excess metal into droplets for VLS growth. As the pressure is increased, the plasma-plume and its metal core are laterally confined, leading instead to VS growth.

Thus, PLD is shown to afford a means to tune the growth mode of ITO between the direct VS and the liquid-metal-droplet-mediated VLS growth modes. Tuning the growth mode switches the resulting crystalline structure from a 3D polycrystalline film into an array of vertically aligned nanowires. Since the tuning directly corresponds to the compression/expansion of the plasma plume, it can be directly controlled through the frequency and pressure parameters of the PLD growth. The same principle may be applicable to PLD growth of other metal oxides for tailoring various material parameters such as transparency, conductivity, and dielectric constant. The tailoring of VLS vs. VS growth via plasma-plume compression is also likely to be useful for designing nanostructures in a wide variety of complex metal-oxide systems.

For increasing tin content (ITO to hyper-eutectoid ITO), the resulting NW transitioned from smooth and vertically oriented to more irregular shape and orientation, while reactive deposition of an eutectic mixture of indium and tin in oxygen resulted in high aspect ratio branched NW surrounded by lenticular nano-particles and the formation of a SnO_2 phase, suggesting spon-

taneous phase separation of In_2O_3 and SnO_2. The spontaneous phase separation for reactive deposition of alloys is promising for developing an approach to spontaneous phase separation within the NW.

4.6 Tables

Reflection	Straight NW	Tapered NW	Pyramidal Grains
2 0 0	**1.86**	**2.95**	**2.58**
2 1 1	0.00	0.00	0.04
2 2 2	0.02	0.11	0.01
1 2 3	0.23	0.27	0.00
4 0 0	**1.99**	**3.63**	**2.42**
4 1 1	0.00	0.14	0.18
4 2 0	0.72	0.60	1.52
1 3 4	0.00	0.00	0.01
1 2 5	0.00	0.00	0.01
4 4 0	0.00	0.00	0.01
6 0 0	**2.16**	**3.13**	**3.21**
6 2 2	0.00	0.01	0.02
1 3 6	0.00	0.00	0.03
4 4 4	0.03	0.11	0.00

Table 4.I. Texture coefficients, $P(\mathbf{h}_i)$, for the arrays of straight NW, tapered NW, and pyramidal grains. When $P(\boldsymbol{h}_i) > 1$, $[\boldsymbol{h}_i]$ is a preferential orientation; when $P(\boldsymbol{h}_i) < 1$, $[\boldsymbol{h}_i]$ is not a preferential orientation. For clarity, the preferential orientations determined from this quantification, 6 0 0, 4 0 0, and 2 0 0, are shown in bold.

4.7 Figures

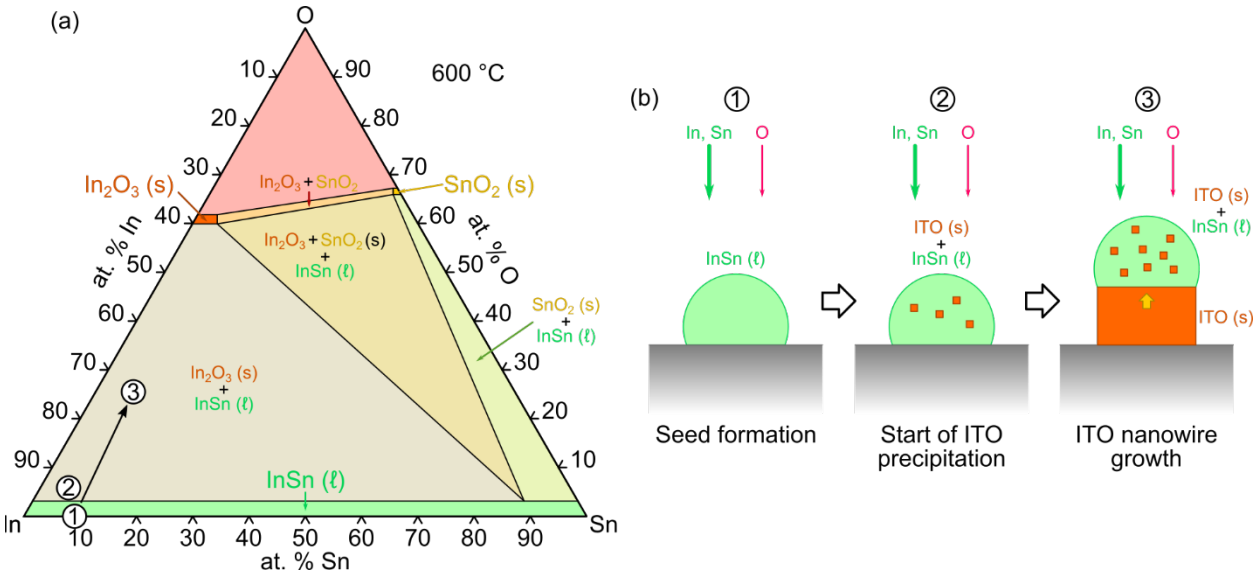

Figure 4.1: schematic representation of the VLS growth mode for 90-10 wt. % In_2O_3 – SnO_2 (ITO) NW. **(a)** Ternary phase diagram for In, Sn, and O, showing the regions for the In_2O_3, SnO_2 solid phases, InSn liquid phase, and the regions for the relative mixed phases. Steps for the VLS growth of ITO NW are indicated with circled numbers. **(b)** Schematic representation of the steps for VLS growth of ITO NW indicated in (a) with the circled numbers: ① initial liquid 90-10 wt. % In-Sn alloy droplets, ② beginning of precipitation of ITO within the droplets, and ③ growth of ITO NW stem at the base of the droplet with continued ITO precipitation.

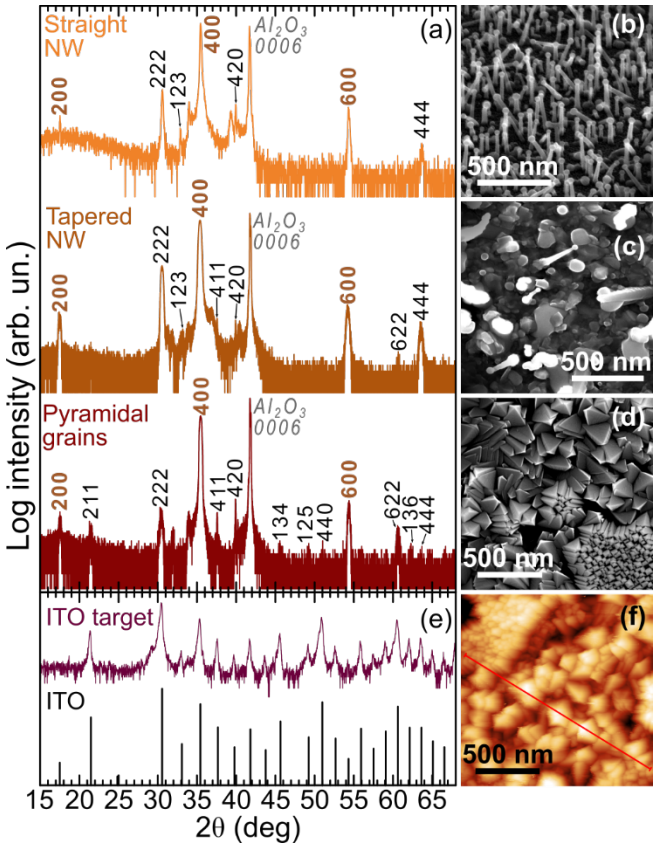

Figure 4.2: X-ray diffraction spectra and scanning electron microscopy images of In_2O_3-SnO_2 90-10 wt.% (ITO) layers. **(a)** Plot of x-ray intensity versus 2θ for θ-2θ x-ray diffraction spectra from layers prepared using pulsed-laser deposition (PLD) with low pressure/low pulse frequency (LoP + LoF - top), low pressure/high pulse frequency (LoP + HiF - middle), and high pressure/high pulse frequency (HiP + HiF - bottom), in comparison with spectra from **(e)** the In_2O_3-SnO_2 90-10 wt.% (ITO) ablation target and the ITO powder reference.[13] Corresponding scanning-electron microscopy (SEM) images, revealing arrays of **(b)** straight smooth NWs, **(c)** tapered NWs, and **(d)** pyramidal grains, are shown on the right. An additional atomic-force micrograph of pyramidal grains is shown in (f), with a line indicating the location of the line-cut shown in Fig. 4.2(i).

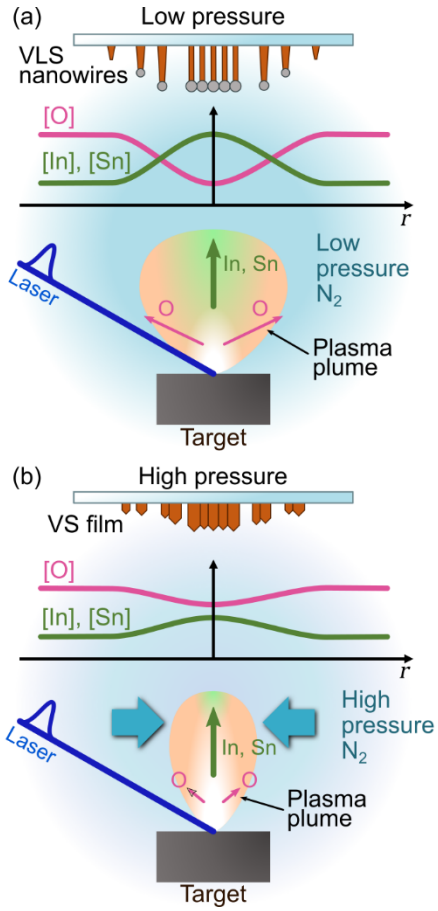

Figure 4.3: Schematic of the plasma-plume expansion and its resulting stoichiometry. (a) For low N_2 pressure, oxygen is strongly scattered, resulting in a metal-rich core, as represented by the radial dependence of the oxygen, indium, and tin concentrations. The excess metal condenses in droplets on the substrate giving rise to VLS growth. (b) For higher N_2 pressure, the plasma-plume expansion is limited by the N_2, reducing the loss of oxygen, resulting in an oxygen rich plasma, as indicated by the radial plot of oxygen, indium and tin density. The oxygen rich plasma is deposited on the substrate giving rise to VS growth.

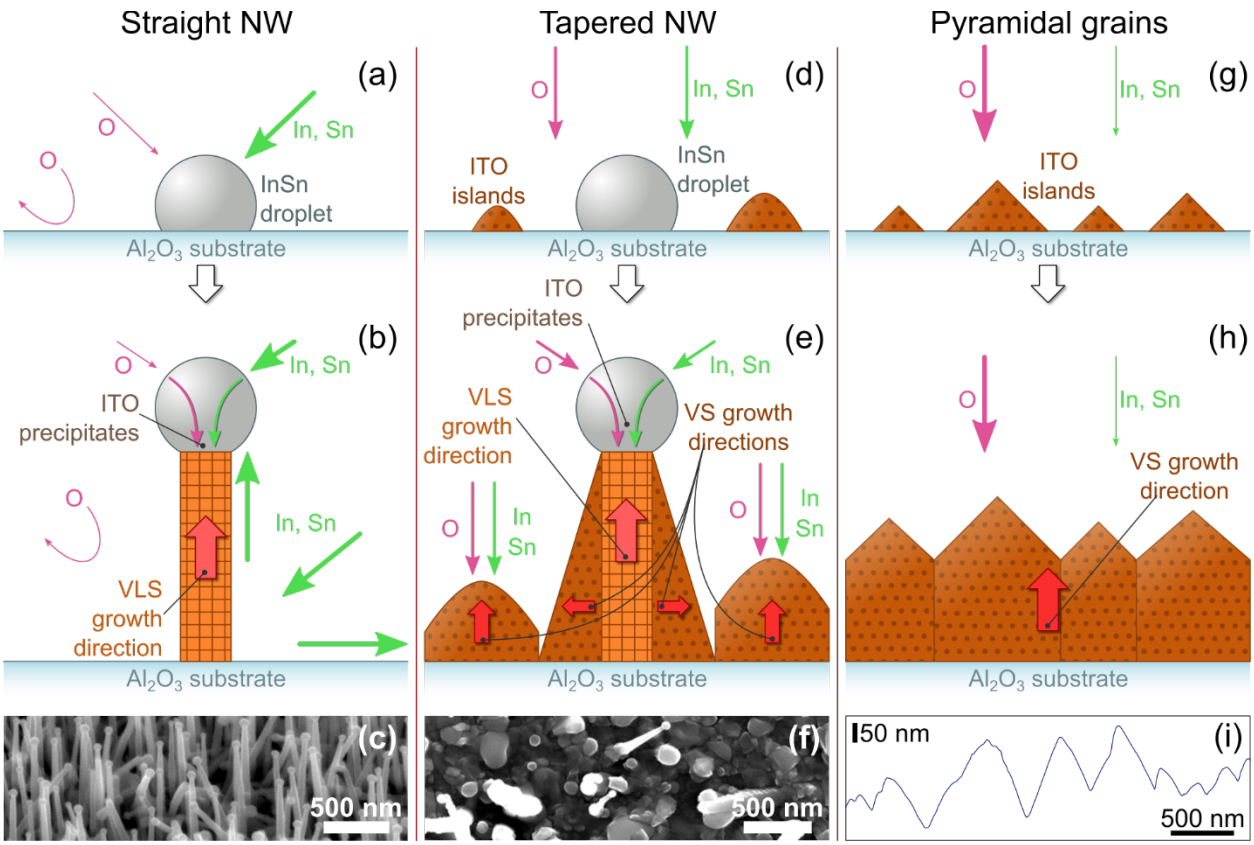

Figure 4.4: Schematic of the growth mechanism for straight smooth NW (VLS growth), tapered NW (VLS + VS), and poly-crystalline film. (a) For the VLS growth mode, metal droplets are formed, then (b) metal droplets act as catalysts for NW growth, resulting in (c) straight NW with spherical tips. (d) For concurrent VLS and VS growth modes, metal droplets and 3D islands nucleate, then (e) metal droplets give rise to NW and VS growth gives rise to polycrystal film among the NW, and overgrowth of film on the NW stems. The growth results in (h) tapered NW with spherical tips, surrounded by nano-particles. (g) For the VS growth mode, only 3D islands form, giving rise to (h) poly-crystalline columnar growth. (i) Line-cut from AFM image of VS ITO film in Fig. 4.2(f), showing the profile of the pyramidal grain tip.

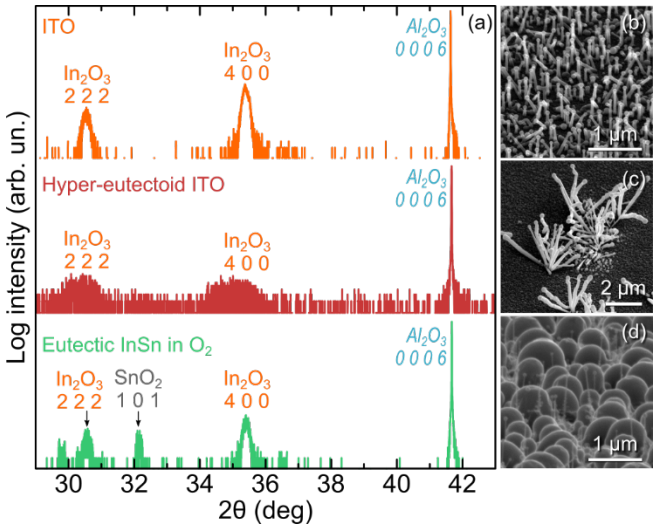

Figure 4.5: X-ray diffraction spectra and scanning electron microscopy images of ITO, hyper-eutectoid ITO, and eutectic InSn layers. **(a)** Plot of x-ray intensity versus 2θ for θ-2θ x-ray diffraction spectra from layers prepared using pulsed-laser deposition (PLD) of ITO in inert N_2 (top, orange), hyper-eutectoid ITO in inert N_2 (middle, red), and eutectic InSn in reactive O_2 (bottom, green). Reflections belonging to the In_2O_3, Al_2O_3 and SnO_2 crystal structures are labeled. **(b)** SEM image of the ITO NW. **(c)** SEM image of the hyper-eutectoid NW. **(d)** SEM image of the eutectic InSn NW.

4.8 References

[1] C. O'Dwyer, M. Szachowicz, G. Visimberga, V. Lavayen, S.B. Newcomb, and C.M.S. Torres, "Bottom-up growth of fully transparent contact layers of indium tin oxide nanowires for light-emitting devices" Nat. Nanotechnol. 4, 239 (2009).

[2] B.L. Williams, A.A. Taylor, B.G. Mendis, L. Phillips, L. Bowen, J.D. Major, and K. Durose, "Core-shell ITO/ZnO/CdS/CdTe nanowire solar cells" Appl. Phys. Lett. **104**, 053907 (2014).

[3] M. Yoshimura, E. Nakai, K. Tomioka, and T. Fukui, "Indium tin oxide and indium phosphide heterojunction nanowire array solar cells" Appl. Phys. Lett. **103**, 243111 (2013).

[4] X.Y. Xue, Y.J. Chen, Y.G. Liu, S.L. Shi, Y.G. Wang, and T.H. Wang, "Synthesis and ethanol sensing properties of indium-doped tin oxide nanowires" Appl. Phys. Lett. **88**, 201907 (2006).

[5] R. Pruna, F. Palacio, M. López, J. Pérez, M. Mir, O. Blázquez, S. Hernández, and B. Garrido, "Electrochemical characterization of organosilane-functionalized nanostructured ITO surfaces" Appl. Phys. Lett. 109, 063109 (2016).

[6] Q. Wan, P. Feng, and T.H. Wang, "Vertically aligned tin-doped indium oxide nanowire arrays: Epitaxial growth and electron field emission properties" Appl. Phys. Lett. **89**, 123102 (2006).

[7] S.-Q. Li, K. Sakoda, J.B. Ketterson, and R.P.H. Chang, "Broadband resonances in indium-tin-oxide nanorod arrays" Appl. Phys. Lett. 107, 031104 (2015).

[8] D.S. Choi, M. Singh, H. Zhou, M. Milchak, and J. Hahm, "Scattering attributes of one-dimensional semiconducting oxide nanomaterials individually probed for varying light-matter interaction angles" Appl. Phys. Lett. 107, 151110 (2015).

[9] J. Hong Noh, B. Ding, H. Soo Han, J. Seong Kim, J. Hoon Park, S. Baek Park, H. Suk Jung, J.-K. Lee, and K. Sun Hong, "Tin doped indium oxide core—TiO2 shell nanowires on stainless steel mesh for flexible photoelectrochemical cells" Appl. Phys. Lett. **100**, 084104 (2012).

[10] Q. Li, F. Yun, Y. Li, W. Ding, and Y. Zhang, "Fabrication and application of indium-tin-oxide nanowire networks by polystyrene-assisted growth" Sci. Rep. **7**, 1600 (2017).

[11] M. Zahirul Alam, I. De Leon, R.W. Boyd. "Large optical nonlinearity of indium tin oxide in its epsilon-near-zero region" Science, 352, 795 (2016).

[12] G.G. Khan, S. Ghosh, A. Sarkar, G. Mandal, G.D. Mukherjee, U. Manju, N. Banu, and B.N. Dev, "Defect engineered d^0 ferromagnetism in tin-doped indium oxide nanostructures and nanocrystalline thin-films" J. Appl. Phys. **118**, 074303 (2015).

[13] E. Joanni, R. Savu, M. de Sousa Góes, P.R. Bueno, J.N. de Freitas, A.F. Nogueira, E. Longo, and J.A. Varela, "Dye-sensitized solar cell architecture based on indium–tin oxide nanowires coated with titanium dioxide" Scr. Mater. **57**, 277 (2007).

[14] ASM Alloy Phase Diagram Database, diagram n. 210203.

[15] G. Grank, L. Brock, H.D. Bausen, "The solubilities of Sn in In_2O_3 and of In in SnO_2 crystals grown from Sn—In melts" J. Cryst. Gr. **36**-1, 179 (1976).

[16] The labeling in Fig. 4.1(a) follows the phase diagram convention of labeling crystal phases with the name of the edge compound to which the crystal phase belongs. Consequently, outside of the external edges of the phase diagram, In_2O_3 (s), SnO_2 (s), and InSn (l) correspond to In_2O_3:Sn in the bixbyite crystal phase, SnO_2:In in the rutile crystal phase, and a liquid InSn phase with O dissolved in it, respectively.

[17] Y.Y. Kee, S.S. Tan, T.K. Yong, C.H. Nee, S.S. Yap, T.Y. Tou, G. Sfrn, Z.E. Horvth, J.P. Moscatello, Y.K. Yap, G. Sáfrán, Z.E. Horváth, J.P. Moscatello, Y.K. Yap, G. Sfrn, Z.E. Horvth, J.P. Moscatello, and Y.K. Yap, "Low-temperature synthesis of indium tin oxide nanowires as the transparent electrodes for organic light emitting devices" Nanotechnology **23**, 025706 (2012).

[18] E. Joanni, R. Savu, M. de Sousa Góes, P.R. Bueno, J.N. de Freitas, A.F. Nogueira, E. Longo, and J.A. Varela, "Dye-sensitized solar cell architecture based on indium–tin oxide nanowires coated with titanium dioxide" Scr. Mater. **57**, 277 (2007).

[19] ICDD PDF record # 01-089-4597.

[20] ICDD PDF record # 00-046-1212.

[21] T.E. Itina, "Stoichiometry distribution of thin films deposited by laser ablation: Monte Carlo simulation" Nucl. Instruments Methods Phys. Res. B 180, 112 (2001).

[22] S. Canulescu, M. Döbeli, X. Yao, T. Lippert, S. Amoruso, and J. Schou, "Nonstoichiometric transfer during laser ablation of metal alloys" Phys. Rev. Mater. 1, 073402 (2017).

[23] R. Eason, "Pulsed Laser Deposition," Wiley-interscience, 2006.

[24] B.N. Masina, S. Lafane, L. Wu, S. Abdelli-Messaci, T. Kerdja, and A. Forbes, "Optimizing the synthesis of vanadium–oxygen nanostructures by plasma plume dynamics using optical imaging" Opt. Eng. **54**, 037106 (2015).

[25] P.L.G. Ventzek, R.M. Gilgenbach, C.H. Ching, and R.A. Lindley, "Schlieren and dye laser resonance absorption photographic investigations of KrF excimer laser-ablated atoms and molecules from polyimide, polyethyleneterephthalate, and aluminum" J. Appl. Phys. **72**, 1696 (1992).

[26] J.M. Warrender and M.J. Aziz, "Effect of deposition rate on morphology evolution of metal-on-insulator films grown by pulsed laser deposition" Phys. Rev. B **76**, 045414 (2007).

[27] S.K. Choi and J.I. Lee, "Effect of film density on electrical properties of indium tin oxide films deposited by dc magnetron reactive sputtering" J. Vac. Sci. Technol. A **19**, 2043 (2001).

Chapter 5: Summary and Suggestions for Future Work

5.1 Summary

In this chapter, we summarize the scientific observations and results discussed in the previous chapters, and we offer some possible avenues for future research work.

In Ch. 3, we used a combined experimental-computational approach to study the effect of local substrate curvature on the evolution of positioning of InAs QDs on nano-patterned (Al)GaAs surfaces. In contrast with existing simulations of QD growth, which are performed on virtually designed substrates,[1,2,3,4,5] we used AFM linecuts of the flat and mounded surface for our PFM simulation. The PFM-simulated InAs/GaAs QD linecuts showed QD positions shifting so that the QDs are directly above substrate valleys, i.e., on the edge of the surface mounds (see Fig. 3.2). In the time evolution of the average thickness InAs layer for different substrate curvature ranges (valleys vs. mountains), the SK transition consists of a migration of material from the mountains to the valleys. Additionally, on the mounded substrates, where deeper valleys are available, the SK transition happens earlier than on the flat substrate, with a larger difference in InAs layer thickness above mountains vs. valleys (see Fig. 3.3), indicating that the presence of mounds, offering a larger range of surface curvatures, encourages the formation of QDs. Using a polar pair-correlation function (PPCF) approach (see Appx. A.1), we measured the anisotropy of relative positioning of QDs in the AlGaAs substrates with varying mounds lateral angle (see Fig. 3.4). The resulting PPCF plots quantitatively showed a tendency for the QDs to organize in chains on the edges of the

mounds. This curvature-driven diffusion approach to spontaneous organization of QD arrays is likely extendable to a variety of mounded surfaces.

In Ch. 4, we examined the effect of plasma plume expansion on the morphology of In_2O_3-SnO_2 films deposited on sapphire during pulsed-laser deposition. For increasing N2 pressure, we observed a growth mode switch from vapor-liquid-solid (VLS) growth of NW to vapor-solid (VS) growth of films. We hypothesize that the main physical mechanism directing the selection of the VLS vs. VS growth mode is the kinetics of plasma plume expansion. For low N_2 pressure, while high velocity In and Sn impinge upon the substrate, the lighter O is scattered away, resulting in the formation of the liquid InSn droplets which are responsible for the VLS growth of NW. Conversely, for high N_2 pressure, the lateral compression of the plasma plume results in a higher concentration of oxygen, preventing the initial formation of the InSn droplets necessary for VLS, and resulting instead in the formation of ITO islands (see Figs. 4.3 and 4.4). The observation of the selection of VLS vs. VS growth mode as a result of the plasma plume expansion dynamics is a precious tool for PLD growth of metal oxides, enabling the tailoring a wide variety of material parameters such as transparency, conductivity, and dielectric constant, in addition to the design of complex nanostructures. Due to the difference in atomic weight between the In and Sn, and O causing the phenomenon, this approach is likely extendable to the PLD of any metal-oxide or metal-nitride materials system.

5.2 Quantum Dot Superlattices on Mounded Surfaces

5.2.1 Multi-layer 3D QD superlattice

In this dissertation, we have shown that the surface mounds formed due to the Ehrlich-Schwoebel adatom diffusion barrier constitute exceptional drivers of QD positioning due to the wider range of surface curvature introduced, while retaining the advantageous characteristic of

being relatively unobtrusive features ($\lesssim$ 7 nm high). By growing QDs on those mounded surfaces, we have achieved spontaneous alignment of QDs in chains along the sides of the mounds.

The natural next step in this work studying the kinetic mechanisms that determine the spontaneous organization of SK QDs into regular superlattices is extending this approach to multiple layers to obtain a regular 3D superlattice (QDSL). In previous approaches to building 3D QDSLs, anisotropic strain accumulation from the underlying QD layers was exploited to drive the vertical alignment of QDs, while the first layer was typically distributed isotropically.[6,7,8] In our approach, on the other hand, by exploiting the presence of mounds and driving the alignment of QDs in chains, considerable ordering is already imparted on the QDs in the first layer, which is likely to aid in the formation of a regular 3D cubic QDSL.

Figure 5.1 shows a schematic representation of the process to obtain a 3D QDSL by stacking multiple layers of mound-templated QD chains. The resulting QDSLs are likely promising for a number of devices based on high-density, ordered 3D QDSLs, such as intermediate band solar cells,[9,10,11,12,13] next-generation thermoelectrics,[14,15,16,17,18] infra-red detectors,[19,20,21] and quantum computing.[22]

5.2.2 Mechanisms of mound formation

The formation and geometry of surface mounds during MBE of III-V compounds due to the Ehrlich-Schwoebel barrier are highly dependent on temperature.[23] Additionally, earlier reports suggest that the mound formation is initiated by high roughness of the starting surface,[24,25] likely caused by pitting resulting from the oxide desorption step.[26] The pitting caused by the oxide desorption is, in turn, highly dependent on substrate temperature itself.[26] It is evident that precise control on the growth temperature needed to achieve precise control over the resulting lateral mound slope. It is therefore suggested that the formation of AlGaAs mounds is investigated while

employing a more accurate substrate temperature measurement and calibration method. A powerful option for improved temperature measurements is band-edge thermometry, which uses the temperature dependence of the onset of radiation absorption of semiconductors for absolute temperature measurements.[27]

5.2.3 Improved temperature control on the Riber C21 MBE

A preliminary plan was devised to implement band-edge thermometry on the Riber C21 MBE machine. The "BandiT" (k-Space Associates) is a temperature measurement tool that includes both band-edge thermometry and full-spectrum black body emission monitoring, and as such is well suited for low temperature measurements (< 200 ~ 400 °C) and is not influenced by stray light, or IR from the substrate heater or reflected IR from the source material cells.

In its most effective configuration, the BandiT system consists of a light source and a detector, to be installed on separate ports facing the substrate holder. With assistance from k-Space Associates, the suitable ports on the Riber C21 were identified and are shown in Fig. 5.2. The parts of the system suitable for the thermometry needs of the lab were identified as well.[28]

5.3 Longitudinal Superlattice In_2O_3-SnO_2 Nanowires

This section contains suggestions for methods to induce spontaneous phase separation of indium oxide and tin oxide with nanowires, in order to obtain the spontaneous self-assembly of regular longitudinal superlattice NW. These superlattice NW contain a repeating energy well band structure and a series of interfaces between two different crystal structures. Both the energy wells and the crystal heterointerfaces are expected to lead to a high thermoelectric figure of merit. The series of energy wells causes the contribution to electrical conductivity of only the higher energy

electrons which positively contribute to the Seebeck coefficient, resulting in higher thermopower.[29] The heterointerfaces, in turn, act as phonon scattering sites, reducing the thermal conductivity and thereby increasing the thermoelectric figure of merit.[29]

5.3.1 Pulsed-Laser Deposition of ultra-Sn-rich In_2O_3-SnO_2

In Ch. 4.4.4 we described the PLD of a hyper-eutectoid ITO target in inert N_2 and of a eutectic InSn target in reactive O_2, performed with the goal of obtaining spontaneous In_2O_3-SnO_2 longitudinal phase separation within the NW for increased thermo-power (see Ch. 4.2). For the hyper-eutectoid ITO, x-ray diffraction spectra did not reveal the formation of a SnO_2 phase, while for the eutectic InSn, x-ray diffraction spectra did reveal the formation of a SnO_2 phase, indicating possible In_2O_3-SnO_2 phase separation, as sought by the choice of the Sn-rich targets. The 46-54 wt. % In_2O_3-SnO_2 composition of the hyper-eutectoid ITO target was chosen to yield the same In/Sn ratio of 1.08 as in the eutectic InSn alloy composition of 52-48 wt. % In-Sn. Both were chosen to possibly encourage a spontaneous lamellar In-Sn phase separation within the seeds of the VLS NW, which in turn would result in a phase separation within the NW stem.

Figure 5.3 shows the ternary phase diagram of the In-Sn-O system at 600°C. On the bottom axis, which constitutes the O-free In-Sn alloy range of compositions, the In-Sn content of the various targets employed in this research are reported, namely, 91-9 at. % In-Sn for a "traditional" ITO target, and 52-48 at. % In-Sn for the hyper-eutectoid ITO and the eutectic InSn targets. For each of those targets, the reported In-Sn content is likely to be the In-Sn content of the VLS seed droplets during PLD, due to the very similar atomic weight of In and Sn (115 and 119 g/mol, respectively). Once the In-Sn droplets start incorporating the oxygen that leads to the VLS growth of NW, the In-Sn-O composition of the NW seeds falls along the dotted arrows starting from each

target metal composition. For the traditional ITO target, the precipitate caused by oxygen super-saturation is expected to be In_2O_3:Sn (ITO). For the hyper-eutectoid ITO and the eutectic InSn targets, the oxygen supersaturation is expected to cause the precipitation of both In_2O_3 and SnO_2. However, for these two targets, it is evident from the ternary phase diagram that there is a large swath of oxygen concentration for which the thermodynamics dictate the precipitation of In_2O_3 alone, before reaching the phase region where the formation of In2O3 and SnO2 both is expected. Since VLS is achieved in oxygen poor conditions, this initial preferential precipitation of In_2O_3 alone may be responsible for the absence or relative scarcity of SnO_2 observed in the resulting NW.

The phase diagram in Fig. 5.3 offers a possible solution to this difficulty: ultra-Sn-rich droplets with a 10-90 at. % In-Sn composition are not expected to cross a region where only In_2O_3 precipitates, instead, they are expected to immediately precipitate In_2O_3 and SnO_2 both. The composition of the corresponding ultra-Sn-rich ITO target is 8-92 wt. % In_2O_3-SnO_2. It is therefore suggested that the PLD of an ultra-Sn-rich ITO target be performed in order to obtain this "forced" In_2O_3 and SnO_2 phase separation within the VLS NW seeds, possibly resulting in In_2O_3-SnO_2 phase separation within the NW stem.

5.3.2 Reactive Pulsed-Laser Deposition of InSn alloy

As shown in Ch. 4.4.4, we achieved the formation of high aspect-ratio, branched ITO NW along with lenticular μm-size nanostructures with PLD of a eutectic InSn. X-ray diffraction spectra performed on the NW obtained suggested the presence of a SnO_2 phase. On the other hand, energy dispersive spectroscopy performed resulted a In/Sn content ratio of 1.3 and metal/oxygen ratio of 1.4 for the NW, and an In/Sn ratio of 0.9, and a metal/oxygen ratio of 3.2 for the micrometer-sized

droplets. These measurements indicate In-rich NW and Sn-rich micro-droplets, suggesting that the majority of the Sn content resides within the micro-droplets.

The laser ablation of the eutectic InSn target for PLD of the ITO NW discussed was performed in 0.1 mTorr O_2, with laser pulse frequency of 10 Hz, and a substrate temperature of 500 °C, which are comparable conditions to the ablation of the ITO target that resulted in ITO NW. The laser fluence employed for the eutectic InSn target was, on the other hand, 3 J/cm^2, which is much larger that the fluence employed for ITO ablation of 0.7 – 1 J/cm^2. The higher fluence was chosen to make up for the higher reflectivity of the pure-metal target compared to the ceramic ITO targets. However, the high laser fluence resulted in the formation of craters on the surface of the soft InSn target, which may have resulted in the presence of InSn clusters within the ablated plasma and be responsible for the formation of the micro-droplets. Consequently, it is suggested to perform PLD of the eutectic InSn target at lower laser frequencies, to reduce the formation of the micro-droplets and possibly reduce the segregation of Sn out of the NW.

5.3.3 Alternating Pulsed-Laser Deposition of In_2O_3 and SnO_2

An entirely alternative approach to the fabrication of longitudinal superlattice NW is to perform alternating-target pulsed laser deposition. In this approach, an In_2O_3:Sn and a SnO_2:In target are repeatedly sequentially ablated, thereby possibly inducing the supersaturation of the seed droplets with In or Sn, alternatingly, and the resulting alternating precipitation of In_2O_3:Sn and SnO_2 within the NW stem.

The technical challenge inherent to this approach lies in achieving the kinetic growth conditions that would result in the VLS of both In_2O_3 and SnO_2 NW. We suggest therefore that PLD of SnO_2 NW is performed first, in order to find the conditions that are yield both In_2O_3 and SnO_2 at the same time. This approach is straying somewhat from the goal of directing the spontaneous

self-organization of nanostructured arrays, but it is a natural extension and continuation of the research into the kinetics of PLD that govern VLS vs. VS growth mode started in this dissertation work.

5.3.4 Improved growth monitoring on the Neocera PLD

Reflection high-energy electron diffraction is an extremely important tool for growth calibrations, growth monitoring, and many other uses, for MBE. The implementation of a traditional RHEED system requires an ultra-high vacuum. However, there is the possibility to implement a high-pressure compatible, differentially pumped RHEED system, where the electron gun resides in the second of two differential pumping stages, each pumped by a turbo pump backed by a dry-scroll pump, and the electron beam travels through the differentially pumped stages and exits into the main chamber via a small, shuttered orifice. In this configuration, a differentially pumped RHEED system would be an extremely useful addition to the existing Neocera PLD chamber.

5.4 Single NW circuits and transfer

After the fabrication of longitudinal superlattice NW is achieved, the next challenge is naturally the characterization of the electronic and thermal transport of the NW, to evaluate the effect of the presence of the superlattice on the thermoelectric figure of merit. Appendix B details several approaches that were developed in the course of this dissertation work towards repeatable measuring of the conductivity of single NW.

5.4.1 Focused-ion beam-deposited circuits of drop-cast nanowires

One approach to measure the electrical conductivity of a single NW consists of realizing a macroscopic electrical circuit around an isolated nanowire that has been removed from its growth substrate by scraping and deposited (drop-cast) onto an insulating substrate with pre-patterned gold leads. The single NW is connected to the gold leads with macroscopic contact pads via focused-

ion beam (FIB)-deposited platinum contacts (see Appx. B.2 and Figs. B.1 and B.2). The advantage of this approach is that the circuits obtained are robust and durable, and it is trivial to identify the same NW for subsequent measurements, as it is electrically connected to macroscopic gold contact pads. The disadvantage of this approach is that it requires destroying (scraping) the growth sample.

Additionally, the difficulty encountered during the development of this approach is that the platinum deposition for the leads connecting the NW to the pre-patterned gold leads appears to result in unwanted platinum deposition around the leads and the NW, resulting essentially in a short that bypasses conduction through the NW. It is suggested therefore that the following procedure is performed using focused-ion beam deposition: (1) cover the NW in a thin layer of insulating SiO_2, (2) perforate the insulating layer in correspondence with the ends of the NW with ion milling, (3) deposit thick platinum leads connecting the ends of the NW to the gold leads (4) "clean up" the excess Pt deposition by gently ion-milling the entire area, being careful not to completely remove the Pt leads or the SiO_2 protection of the NW.

5.4.2 In-situ dual nano-manipulator single-nanowire I-V characteristics measurement

Another approach to measure the electrical conductivity of a single NW consists of using nano-manipulators within a focused-ion beam microscope for in-situ, direct measurements of NW on their growth substrate (see Appx. B.3 and Figs. B.3 and B.4). The advantage of this approach is that it is not destructive. The disadvantage of this approach is that the repeated identification of the same NW on its growth substrate is less trivial than for a NW drop-cast on a numbered grid, due to the high density of NW on the growth substrate. Another disadvantage of this technique is that it requires a conductive "wetting layer" around the as-grown NW, because it is used as the "ground" of the measuring circuit. Finally, the "nano-surgery" nature of this approach, while not especially time-consuming, requires some practice and trial-and-error. It is therefore suggested

that this technique may be useful for preliminary characterization of a NW sample, before choosing to move onto more labor intensive or destructive characterization approaches.

5.4.3 Single NW transfer

A third approach for NW transport characteristics measurement that combines the stability and repeatability of the drop-cast NW circuits and the non-destructivity of the in-situ measurements is nano-manipulator single NW transfer to a separate substrate. Figure 5.4 shows a schematic diagram for the process of the single-NW lift-out performed within a FIB-SEM equipped with a nano-manipulator and Pt electron-beam deposition.

The single-NW lift-out procedure is as follows. First, a suitable NW is identified (non-vertical if possible, > 750 μm long) [Fig. 5.4(a)]. An ideal NW is oriented closer to parallel to the surface of the sample because in this orientation it can lay across the nano-manipulator needle instead of parallel to it as seen from the electron beam, rendering the e-beam welding of the NW to the nano-manipulator easier. Once the tip of the nano-manipulator needle is sharpened to a length of 6 ~ 8 μm and a diameter of < 1 μm [Fig. 5.4(b)], the sharpened needle is placed immediately touching beneath the NW and the two are welded together using e-beam Pt deposition [Fig. 5.4(c)]. Once welded, if the nano-manipulator needle is slowly lifted, the NW should cleanly break off of the substrate and be lifted-out with the nano-manipulator needle [Fig. 5.4(d)]. After the lift-out, the base of the welded NW is brought into contact with the side of the post of a copper transmission-electron microscope (TEM) grid. If the welded NW is not too flexible or brittle, a portion of the base of the NW may be pushed inside the copper post to increase the stability of the NW on the post and ease the release of the NW from the nano-manipulator needle. Once the NW is touching/inserted into the TEM grid post, the NW is welded to the TEM grid post with e-beam Pt deposition and the nano-manipulator needle is retracted [Fig. 5.4(d)]. Once the NW is mounted on the

TEM grid post, it is ready for repeatable high-resolution imaging and electron-beam diffraction within a TEM and for I-V characteristics measurements within a FIB equipped with a nano-manipulator.

5.5 NW fluorescence

The high conductivity of ITO is due to the oxygen vacancies induced by the high density of tin acting as electron donors.[30] Light spectroscopy can probe the variously ionized oxygen vacancy defects, as well as Sn substitutional defects, therefore giving insight in the conduction mechanisms within the ITO. For example, photo-luminescence spectroscopy reveals oxygen-vacancy emission states with 420 nm and 436 nm wavelengths, and Sn defect emission states with 390 nm and 496 nm wavelengths.[31]

Confocal fluoresce microscopy offers an exciting possibility to probe the emission states of ITO defects and, at the same time, resolve the relative positioning of these defects with spectral imaging, e.g. within the stem vs. within the tips of the NW. During confocal microscopy, a focused laser beam with fixed wavelength is scanned across the surface of the sample. The fixed wavelength light excites the fluorescence emission states of the sample. Emission spectra can then be captured integrating across the entire scanning field for a given image, or separate fluorescence emission spectrum can be capture for each pixel within the image, allowing the capture of a spectrally-resolved image. Fig. 5.6 shows a schematic representation of the confocal microscopy process.

The resolution of a confocal microscope is close to the size of the ITO NW studied in this dissertation. It is therefore suggested that, for this purpose, longer NW are grown. It would likely be advantageous to disperse these longer NW onto a featureless substrate such as a Si or SiO_2

wafer, in order to obtain isolated NW, parallel to the imaging plane, in order to facilitate the spectral imaging.

5.6 Figures

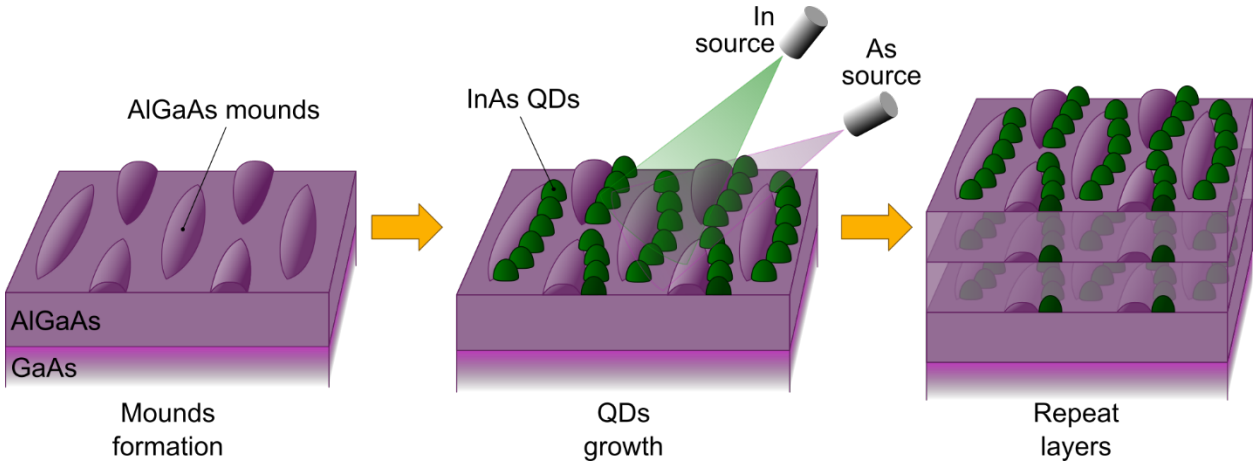

Figure 5.1: Schematic representation of the process to achieve a regular 3D QD superlattice from mounds-templated first-layer QD chains.

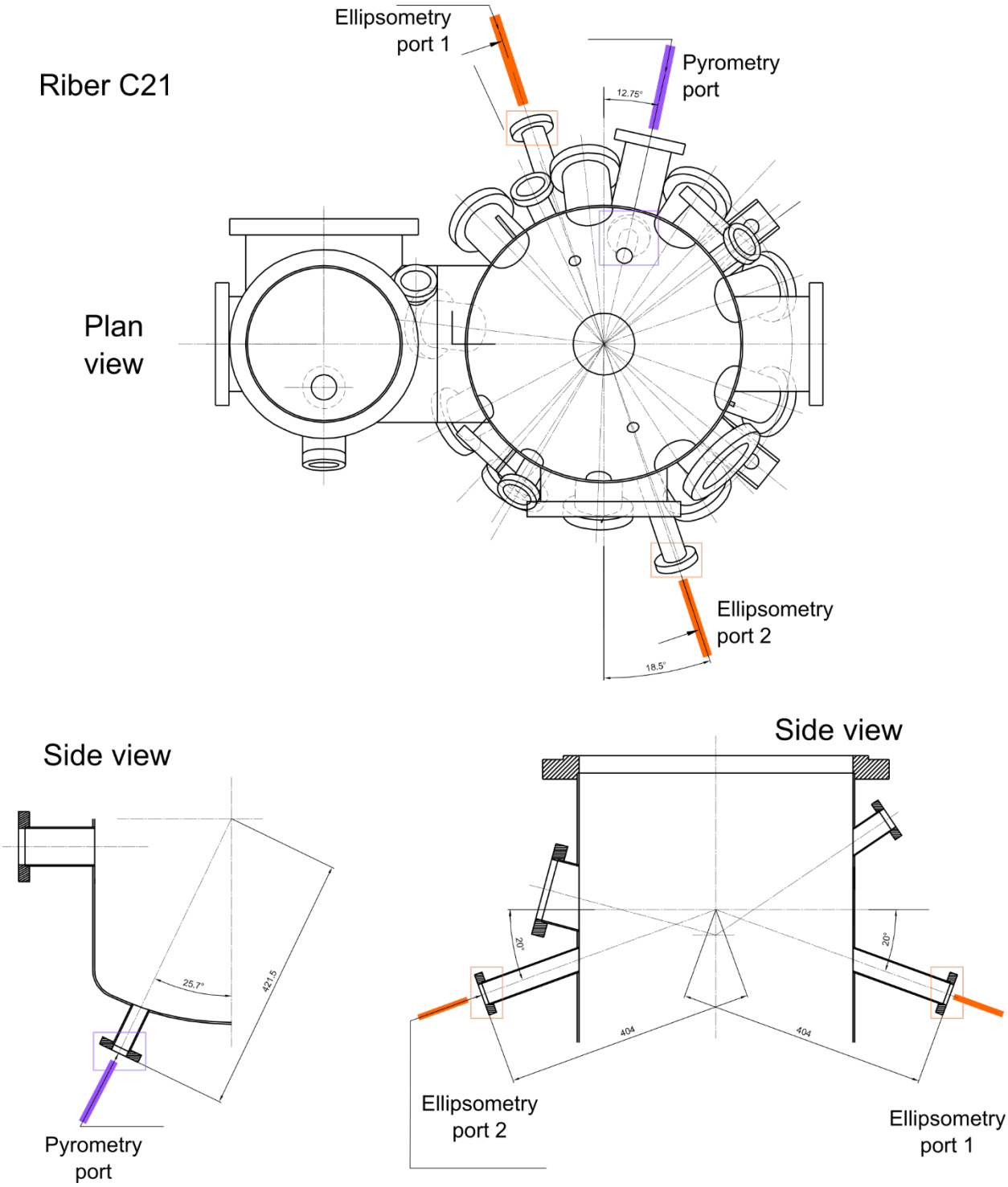

Figure 5.2: Diagram of the ports available on the Riber C21 MBE for installation of a band-edge thermometry tool, with both the option for single-port and two-ports configuration.

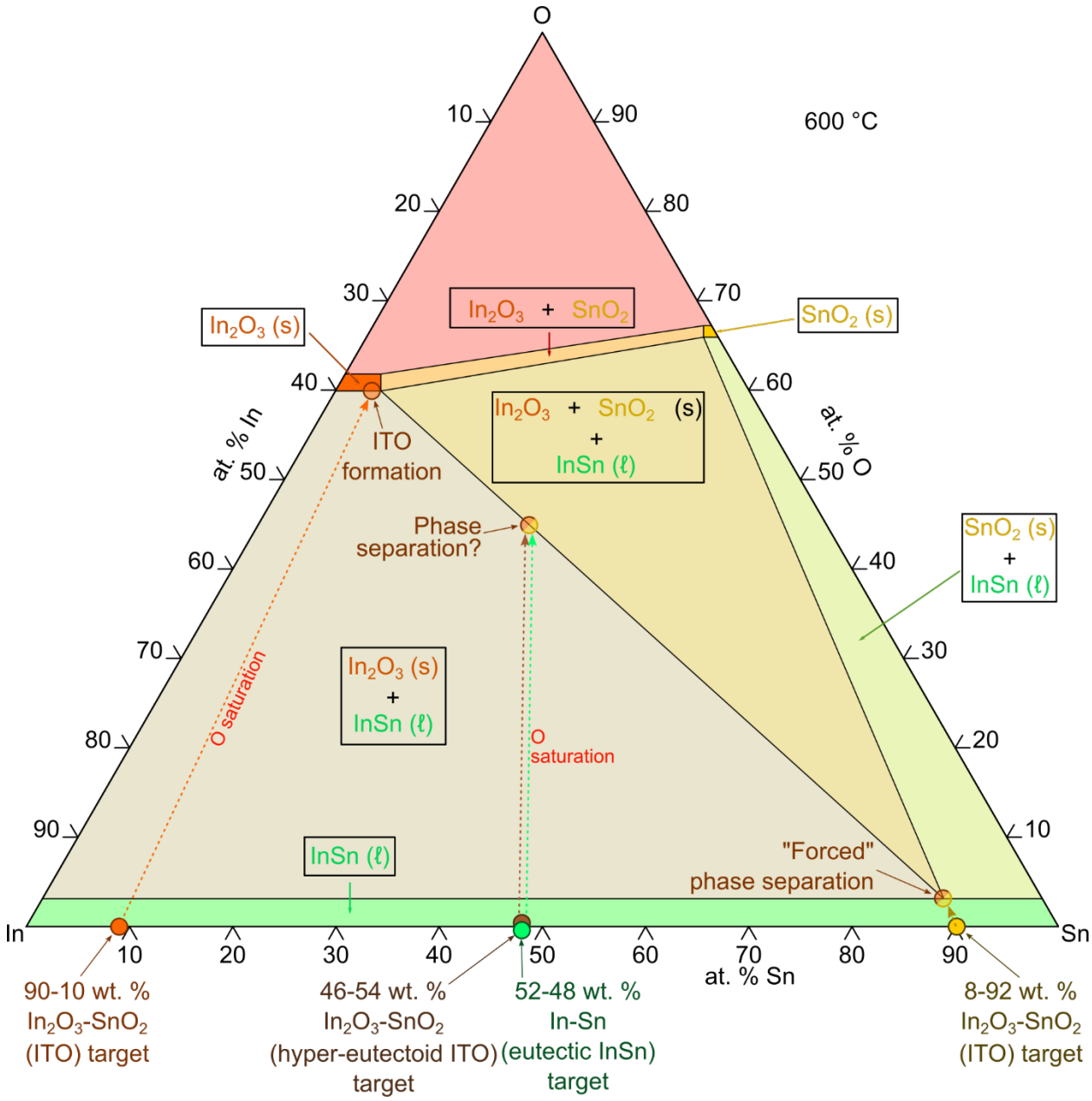

Figure 5.3: ternary phase diagram for the In-Sn-O system at 600°C, indicating the targets employed in this research and the proposed Sn-rich target for future investigation.

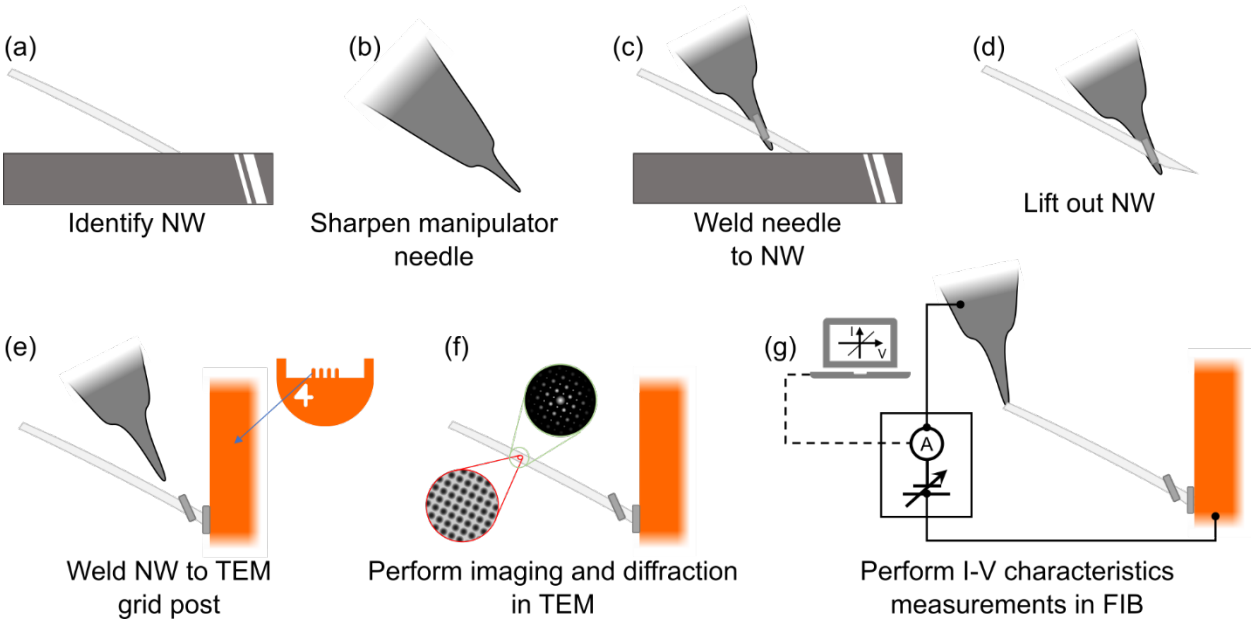

Figure 5.4: schematic representation of the method for lift-out of a single NW for repeatable TEM and I-V characteristics measurements. **(a)** A suitable NW is identified. **(b)** The W needle mounted on a linear nano-manipulator arm is sharpened using FIB ion-milling. **(c)** The nano-manipulator needle is welded to the NW via electron-beam platinum deposition. **(d)** The NW is lifted out. **(e)** The NW is welded at the base to the post of a TEM grid and the nano-manipulator needle is removed. At this point, the NW mounted on the TEM grid is ready for repeated imaging and electron diffraction in a TEM **(f)** and for I-V characteristics measurements within a FIB-SEM **(g)**.

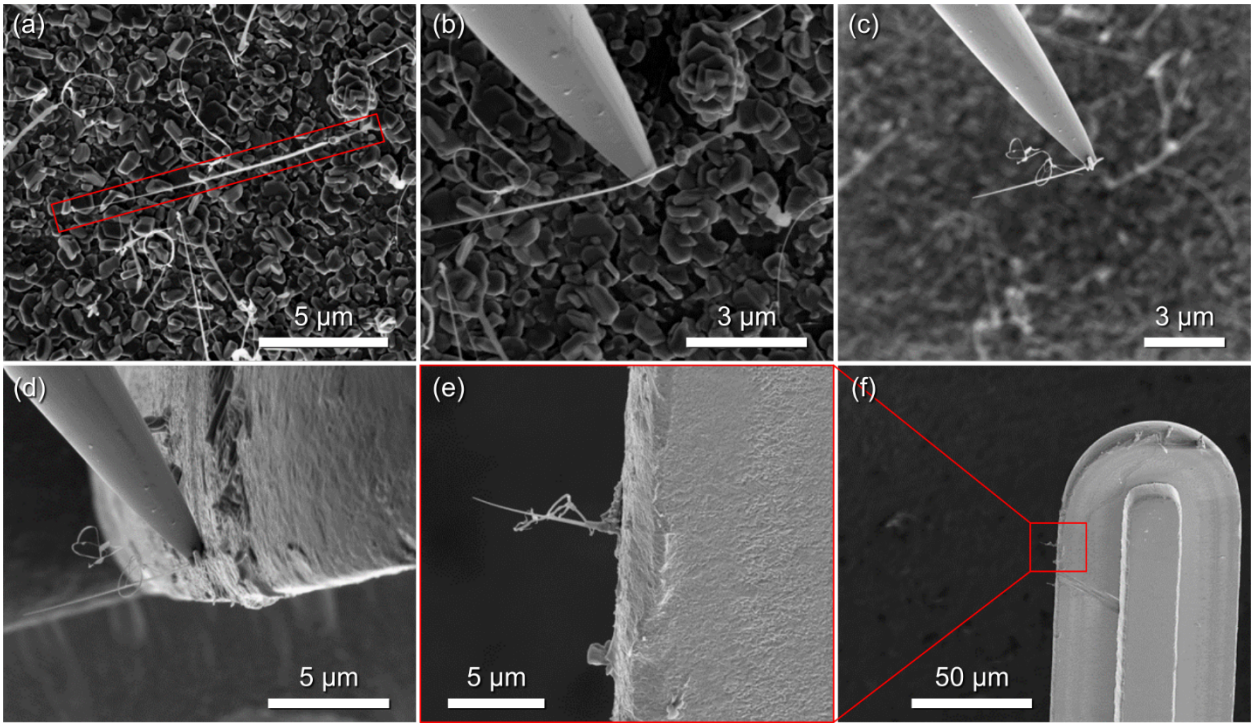

Figure 5.5: SEM micrographs of the single NW lift-out and mounting process. **(a)** A suitable NW is identified. **(b)** the sharpened needle of a nano-manipulator is approached to the NW and welded to the NW with electron-beam Pt deposition. **(c)** The NW is lifted out with the nano-manipulator. **(d)** The NW is approached to the post of a TEM grid. **(e)** The NW is welded to the TEM grid post and the nano-manipulator needle is retracted. **(f)** Lower-magnification view of the TEM grid post with the mounted NW.

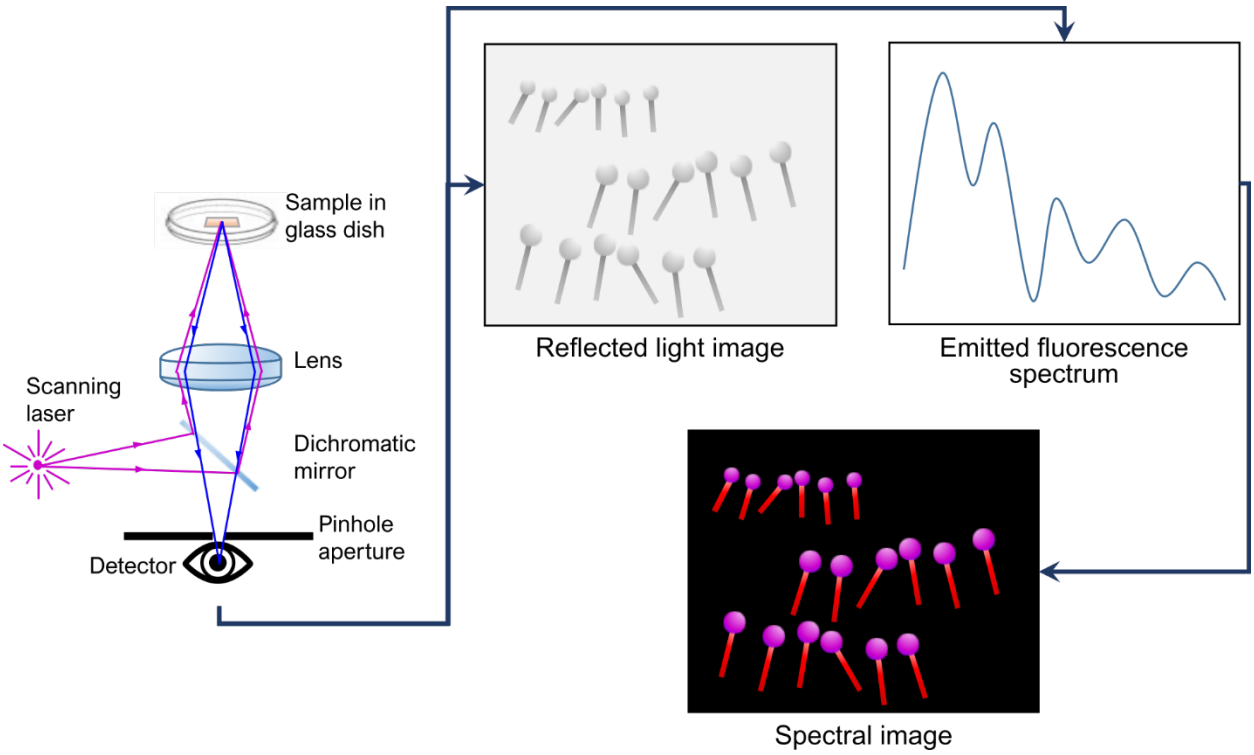

Figure 5.6: schematic representation of the visible light, fluorescence spectroscopy, and fluorescence spectral imaging of VLS NW within a confocal microscope.

5.7 References

[1] K.R. Elder, Z.-F. Huang, and N. Provatas, "Amplitude expansion of the binary phase-field-crystal model" Phys. Rev. E **81**, 011602 (2010).

[2] Y. Ni, L.H. He, and A.K. Soh, "Three-dimensional phase field simulation for surface roughening of heteroepitaxial films with elastic anisotropy" J. Cryst. Growth **284**, 281 (2005).

[3] L.K. Lee, L.K. Aagesen, K. Thornton, and P.-C. Ku, "Origin of broad luminescence from site-controlled InGaN nanodots fabricated by selective-area epitaxy" Phys. Status Solidi A **211**, 531 (2014).

[4] L.K. Aagesen, M.E. Coltrin, J. Han, and K. Thornton, "Phase-field simulations of GaN growth by selective area epitaxy from complex mask geometries" J. Appl. Phys. **117**, 194302 (2015).

[5] J.J. Eggleston and P.W. Voorhees, "Ordered growth of nanocrystals via a morphological instability" Appl. Phys. Lett. **80**, 306 (2002).

[6] V. Latini, E. Placidi, F. Arciprete, and F. Patella, "In-line correlation and ordering of InAs/GaAs multistacked Quantum Dots structures" J. Cryst. Growth **419**, 138 (2015).

[7] Z.M. Wang, K. Holmes, Y.I. Mazur, and G.J. Salamo, "Fabrication of (In,Ga)As quantum-dot chains on GaAs(100)" Appl. Phys. Lett. **84**, 1931 (2004).

[8] W. Ye, S. Hanson, M. Reason, X. Weng, and R.S. Goldman, "Control of InAs/GaAs quantum dot density and alignment using modified buffer layers" J. Vac. Sci. Technol. B 23, 1736 (2005).

[9] V. Mlinar, Nanotechnology **24**, "Engineered nanomaterials for solar energy conversion" Nanotechnology 24 042001 (2013).

[10] S. Rodríguez-Bolívar, F.M. Gómez-Campos, A. Luque-Rodríguez, J.A. López-Villanueva, J.A. Jiménez-Tejada, and J.E. Carceller, "Miniband structure and photon absorption in regimented quantum dot systems" J. Appl. Phys. **109**, (2011).

[11] V. Popescu, G. Bester, M.C. Hanna, A.G. Norman, and A. Zunger, "Theoretical and experimental examination of the intermediate-band concept for strain-balanced (In,Ga)As/Ga(As,P) quantum dot solar cells" Phys. Rev. B - Condens. Matter Mater. Phys. **78**, 1 (2008).

[12] Q. Shao, A.A. Balandin, A.I. Fedoseyev, and M. Turowski, "Intermediate-band solar cells based on quantum dot supracrystals" Appl. Phys. Lett. **91**, 2005 (2007).

[13] A. Luque, A. Martí, E. Antolín, and C. Tablero, "Intermediate bands versus levels in non-radiative recombination" Phys. B Condens. Matter **382**, 320 (2006).

[14] V.M. Fomin and P. Kratzer, "Thermoelectric transport in periodic one-dimensional stacks of InAs/GaAs quantum dots" Phys. Rev. B - Condens. Matter Mater. Phys. **82**, 045318 (2010).

[15] A. Yadav, K.P. Pipe, W. Ye, and R.S. Goldman, "Thermoelectric properties of quantum dot chains" J. Appl. Phys. **105**, (2009).

[16] A.A. Balandin and O.L. Lazarenkova, "Mechanism for thermoelectric figure-of-merit enhancement in regimented quantum dot superlattices" Appl. Phys. Lett. **82**, 415 (2003).

[17] O.L. Lazarenkova and A.A. Balandin, "Miniband formation in a quantum dot crystal" J. Appl. Phys. **89**, 5509 (2001).

[18] A. Khitun, A. Balandin, J.L. Liu, and K.L. Wang, "In-plane lattice thermal conductivity of a quantum-dot superlattice" J. Appl. Phys. **88**, 696 (2000).

[19] W.-G. Wu, J.-L. Liu, G. Jin, and K.L. Wang, "Mid-infrared absorption in self-assembled Ge quantum dots grown on Si substrate" Silicon-Based Optoelectron. **3630**, 98 (1999).

[20] J.L. Liu, W.G. Wu, A. Balandin, G.L. Jin, and K.L. Wang, "Intersubband absorption in boron-doped multiple Ge quantum dots" Appl. Phys. Lett. **74**, 185 (1999).

[21] J.L. Liu, W.G. Wu, A. Balandin, G. Jin, Y.H. Luo, S.G. Thomas, Y. Lu, and K.L. Wang, "Observation of inter-sub-level transitions in modulation-doped Ge quantum dots" Appl. Phys. Lett. **75**, 1745 (1999).

[22] T. Ohshima, H.Z. Song, Y. Okada, K. Akahane, T. Miyazawa, M. Kawabe, and N. Yokoyama, "Precisely ordered quantum dot array formed using AFM lithography for all-optical electron spin quantum computers" Phys. Status Solidi C Conf. **1367**, 1364 (2003).

[23] C.-F. Lin, H.-C. Kan, S. Kanakaraju, C. Richardson, and R. Phaneuf, "Directed Kinetic Self-Assembly of Mounds on Patterned GaAs (001): Tunable Arrangement, Pattern Amplification and Self-Limiting Growth" Nanomaterials **4**, 344 (2014).

[24] A. Ballestad, B.J. Ruck, M. Adamcyk, T. Pinnington, and T. Tiedje, "Evidence from the Surface Morphology for Nonlinear Growth of Epitaxial GaAs Films" Phys. Rev. Lett. **86**, 2377 (2001).

[25] V. Coluci, M. Cotta, C. Mendonça, K. I.-Landers, and M. de Carvalho, "Surface morphologies in GaAs homoepitaxy: Mound formation and evolution" Phys. Rev. B - Condens. Matter Mater. Phys. **58**, 1947 (1998).

[26] F. Bastiman, R. Hogg, M. Skolnick, A.G. Cullis, and M. Hopkinson, "Temperature dependence of Ga-assisted oxide desorption on GaAs(001)" J. Phys. Conf. Ser. **209**, (2010).

[27] S. Johnson, C.H. Kuo, M. Boonzaayer, W. Braun, U. Koelle, Y.H. Zhang, and J. Roth, "In situ temperature control of molecular beam epitaxy growth using band-edgethermometry" J. Vac. Sci. Technol. B Microelectron. Nanom. Struct. **16**, 1502 (1998).

[28] "NIR (870-1670nm) Temperature Monitor" (p.n. B-NIR-MBE-1670), "Laser-based Rotational Triggering System" (p.n. KSA-TRG), "Trigger/Home Pulse Signal Conditioner for kSA 400 Control Computer" (p.n. K4SIGC), "Trigger Cable" (p.n. K30FW-T).

[29] M.S. Dresselhaus, G. Chen, M.Y. Tang, R. Yang, H. Lee, D. Wang, Z. Ren, J.-P. Fleurial, and P. Gogna, "New directions for low-dimensional thermoelectric materials" Adv. Mater. **19**, 1043 (2007).

[30] S. Ishibashi, Y. Higuchi, Y. Ota, and K. Nakamura, "Low resistivity indium-tin oxide transparent conductive films. II. Effect of sputtering voltage on electrical property of films." J. Vac. Sci. Technol. A **8** 1403 (1990).

[31] G.G. Khan, S. Ghosh, A. Sarkar, G. Mandal, G.D. Mukherjee, U. Manju, N. Banu, and B.N. Dev, "Defect engineered d_0 ferromagnetism in tin-doped indium oxide nanostructures and nanocrystalline thin-films" J. Appl. Phys. **118**, 074303 (2015).

Appendix A Computer Programs

A.1 Polar pair correlation function

A.1.1 Introduction

This appendix describes the technique used to quantitatively determine the chain-alignment of InAs quantum dots (QDs) on mounded (Al)GaAs surfaces described in Ch. 3. The analysis was performed using the scanning probe microscopy image analyzer Gwyddion (v. 2.51),[1] Python (v. 3.7.0), and OriginLab Origin 2016. In this section we define the (radial/polar) pair correlation function for collections of particles distributed on a plane, then we explain it usefulness in determining whether QDs are aligned in chains.

A.1.1.1 Pair Correlation Functions

The Pair Correlation Function (PCF) is a widely used measure of the deviation of the experimental space distribution of a set of particles from a random, unconstrained distribution.[2,3,4] We term the probability distribution of the distances r between pairs of particles the pair distribution function (PDF) $N(r)$. Given the measured PDF of the experimental distribution of particles $N_{\mathrm{xpt}}(r)$ and the corresponding PDF for a random distribution of particles $N_{\mathrm{rnd}}(r)$, the PCF is calculated, as a function of the particle separation r, as follows:

$$C(r) = \frac{N_{\mathrm{xpt}}(r)}{N_{\mathrm{rnd}}(r)}. \qquad \text{A.1}$$

Thus, $C(r) > 1$ or $C(r) < 1$ indicates a higher or lower, respectively, probability of finding particles sitting at separation r than in a random distribution. In other words, the PCF detects preferential (i.e. > 1) arrangements of particles in the system. The PCF may therefore be useful for the goal of the present work of quantifying the preferential alignment of QDs along the sides of surface mounds (i.e. a deviation from a random distribution of QDs).

The form of the PCF in Eq. A.1, presents, however, both conceptual and practical implementation issues for the current work. The conceptual issue is that, as we set out to quantify the anisotropy of QD placement (i.e. chain alignment), the PCF cannot depend exclusively on the QD pair separation r, but it will have to include a dependence on the relative orientation of the QD pair separation with respect to the direction of elongation of the mounds. Here, we obtain the orientation-dependence by measuring the PDFs as a function of the polar coordinates (r, θ), resulting in a polar pair correlation function (PPCF). As the mound elongation in the AFM images we will be using for calculating the PCF is "vertical" (i.e. bottom to top of image), the relevant orientations will thus be $\theta = 90°$ and $\theta = 270°$.[5]

For the practical implementation of Eq. A.1, we must remember that we are working with both finite-size QDs (as opposed to point-like particles) and finite-size images in which to identify these particles. For the finite size of the QD, the consequence is that, when generating a random distribution of QDs, the randomly generated positions cannot be infinitely close (overlapping QDs). This requires either to force the randomly generated QDs to be at least one average diameter apart, which is unrealistic because QDs do have a size distribution, or calculate a size distribution for the generated QDs and randomly generate both size and position for each QDs, making sure there is no overlap. Additionally, we found the algorithm for the generation of random QDs when

avoiding QD overlap is prone to failure, especially for higher densities (i.e. "unable to find a place for the next QD anywhere").[6]

The finite size of the AFM images, on the other hand, means that the count of QD pairs at a given separation r is always underestimated due to the absence of the QDs outside of the image. Correcting this underestimation requires either calculating the exact area of each ring section of radius r comprised within the image used for the count and using a density instead, or applying an approximated count correction whereby the count is increased by the fraction of the circumference of the ring that falls outside of the image.

In this work, we are quantifying the chain alignment of QDs, which, in terms of angle- and distance-dependent "density," is expected to result in peaks at low r (the nearest neighbor in a chain) for only two diametrically opposed values of θ (one nearest neighbor on each side along a linear chain). Since we are interested primarily in the θ-anisotropy of the PCF at low r, thus, we choose here to simply approximate the $N_{\mathrm{rnd}}(r)$ with the average density of QDs $\bar{\rho}$.

A.1.2 Method

In this section, we describe in detail the method employed to measure the PPCF C_{p} formally discussed in the previous section. Taking an experimentally identified QD q in an image I as the origin of a polar coordinate system, we subdivide the system into annular sections of $\Delta r = 0.1 \cdot d^I_{\mathrm{NN}}$ and $\Delta\theta = \Delta r \,/\, r$, where d^I_{NN} is the average QD nearest neighbor distance in the image I, and we count the QDs comprised within each annular section. We then divide the count $N_{q,I}(r,\theta)$ by the area of the annular section $A_{\Delta r,\Delta\theta}(r) = \Delta r(2r + \Delta r)\Delta\theta/2$, obtaining the "polar density:"

$$\rho_{q,I}(r,\theta) = \frac{N_{q,I}(r,\theta)}{A_{\Delta r,\Delta\theta}(r)}. \qquad \text{A.2}$$

This process is repeated for each QD q in image I, then the average over the N_I QDs in image I is computed:

$$\rho_I(r,\theta) = \sum_{q=1}^{N_I} \frac{N_{q,I}(r,\theta)}{A_{\Delta r,\Delta\theta}(r)}. \tag{A.3}$$

Finally, the average over the M images available is computed:

$$\rho(r,\theta) = \sum_{I=1}^{M} \rho_I(r,\theta). \tag{A.4}$$

At the same time, the average density of QDs is computed for each image I of lateral size ℓ_I, then averaged over the M images available:

$$\bar{\rho} = \sum_{I=1}^{M} \frac{N_I}{\ell_I^2}. \tag{A.5}$$

The PPCF is thus computed as:

$$C_p(r,\theta) = \frac{\rho(r,\theta)}{\bar{\rho}} = \sum_{I=1}^{M}\sum_{q=1}^{N_I} \frac{N_{q,I}(r,\theta)}{A_{\Delta r,\Delta\theta}(r)} \left(\sum_{I=1}^{M} \frac{N_I}{\ell_I^2}\right)^{-1}. \tag{A.6}$$

A.1.3 Python code

In this section, we present the python code used to compute the PPCF for the work illustrated in Ch. 3. The code takes the QDs positions as input and returns the values of the PPCF in polar coordinates in an Origin-friendly file format.

A.1.3.1 Main Python script

polar_pfc_main_18-05-16.py

```
1  import general_qds_manipulation as gqd
2  import polar_pfc as ppfc
3
4  # Run parameters
5  #home = "C:\\Users\\GoldmanGroup\\" # Gerstacker B121 desktop
6  home = "C:\\Users\\david\\" # Mario, Bimmy
7
8  input_dir = home + "Box\\data\\PFM\\pair_correlation_function\\qd_input_data\\"
```

```
output_dir = home + "Box\\data\\PFM\\pair_correlation_function\\python_output\\"

input_file_path = input_dir + "file_list.18-05-11.txt"

dr_multiplier = 0.1

#%%

image_files_dict = gqd.load_images_info(input_file_path)
samples_dict = gqd.generate_samples_dict(image_files_dict)
gqd.load_qds_positions (input_dir, samples_dict)
gqd.compute_samples_separations_list(samples_dict)

#for sample_n_str in samples_dict:
#    sample_dict = samples_dict[sample_n_str]
#    ppfc.compute_sample_polar_pfc(sample_dict, dr_multiplier)
#    ppfc.save_sample_polar_pcf_to_file(sample_dict, output_dir, dr_multiplier)

sample_dict = samples_dict["RMBE237"]
ppfc.compute_sample_polar_pfc(sample_dict, dr_multiplier)
ppfc.save_sample_polar_pcf_to_file(sample_dict, output_dir, dr_multiplier)
```

A.1.3.2 Functions library for calculating the PPCF

polar_pcf.py

```
# -*- coding: utf-8 -*-
"""
Created on Wed May 16 12:25:34 2018

@author: Davide Del Gaudio
"""

from math import sqrt, atan2, ceil, pi, floor
from general_qds_manipulation import _tab, _newl

def compute_sample_polar_pfc (sample_dict, dr_multiplier):
    """Computes sample-wise radial pair correlation function"""
    compute_sample_polar_bins (sample_dict, dr_multiplier)
    n_of_r_bins = sample_dict["n_of_r_bins"]
    n_of_theta_bins_r = sample_dict["n_of_theta_bins_r"]
    sample_qd_density = sample_dict["sample_qd_density"]
    sample_n_of_qds = sample_dict["sample_n_of_qds"]

    sample_polar_pfc = []
    sample_polar_pfc_var = []
    sample_polar_pfc_std = []
    sample_polar_pfc_stderr = []
    for r_bin_idx in range(n_of_r_bins):
        sample_polar_pfc.append([])
        sample_polar_pfc_var.append([])
        sample_polar_pfc_std.append([])
        sample_polar_pfc_stderr.append([])
```

```
        for theta_bin_idx in range(n_of_theta_bins_r[r_bin_idx]):
            sample_polar_pfc[r_bin_idx].append(0)
            sample_polar_pfc_var[r_bin_idx].append(0)
            sample_polar_pfc_std[r_bin_idx].append(0)
            sample_polar_pfc_stderr[r_bin_idx].append(0)

    for image_dict in sample_dict["images_list"]:
        image_dict["image_single_qd_pfcs"] = []
        qds_list = image_dict["qds_list"]
        for center_qd_idx in range(len(qds_list)):
            compute_single_qd_polar_pfc (sample_dict, image_dict, center_qd_idx)
            this_qd_polar_pfc = image_dict["image_single_qd_pfcs"][center_qd_idx]
            for r_bin_idx in range(n_of_r_bins):
                for theta_bin_idx in range(n_of_theta_bins_r[r_bin_idx]):
                    sample_polar_pfc[r_bin_idx][theta_bin_idx] +=
this_qd_polar_pfc[r_bin_idx][theta_bin_idx]

    for r_bin_idx in range(n_of_r_bins):
        for theta_bin_idx in range(n_of_theta_bins_r[r_bin_idx]):
            sample_polar_pfc[r_bin_idx][theta_bin_idx] =
sample_polar_pfc[r_bin_idx][theta_bin_idx] / (n_of_r_bins * sample_qd_density)
    sample_dict["sample_polar_pfc"] = sample_polar_pfc

    for image_dict in sample_dict["images_list"]:
        qds_list = image_dict["qds_list"]
        for center_qd_idx in range(len(qds_list)):
            this_qd_polar_pfc = image_dict["image_single_qd_pfcs"][center_qd_idx]
            for r_bin_idx in range(n_of_r_bins):
                for theta_bin_idx in range(n_of_theta_bins_r[r_bin_idx]):
                    sample_polar_pfc_var[r_bin_idx][theta_bin_idx] +=\
                        (\
                            (this_qd_polar_pfc[r_bin_idx][theta_bin_idx] /
sample_qd_density) -\
                            sample_polar_pfc[r_bin_idx][theta_bin_idx]\
                         )**2
    for r_bin_idx in range(n_of_r_bins):
        for theta_bin_idx in range(n_of_theta_bins_r[r_bin_idx]):
            sample_polar_pfc_var[r_bin_idx][theta_bin_idx] =
sample_polar_pfc_var[r_bin_idx][theta_bin_idx] / (sample_n_of_qds - 1)
            sample_polar_pfc_std[r_bin_idx][theta_bin_idx] =
sqrt(sample_polar_pfc_var[r_bin_idx][theta_bin_idx])
            sample_polar_pfc_stderr[r_bin_idx][theta_bin_idx] =
sample_polar_pfc_std[r_bin_idx][theta_bin_idx] / sqrt(sample_n_of_qds)
    sample_dict["sample_polar_pfc_var"] = sample_polar_pfc_var
    sample_dict["sample_polar_pfc_std"] = sample_polar_pfc_std
    sample_dict["sample_polar_pfc_stderr"] = sample_polar_pfc_stderr

def compute_single_qd_polar_pfc (sample_dict, image_dict, center_qd_idx):
    qds_list = image_dict["qds_list"]
    dr = sample_dict["dr"]
    n_of_r_bins = sample_dict["n_of_r_bins"]
    n_of_theta_bins_r = sample_dict["n_of_theta_bins_r"]

    bins_area_used = []

```

```
    qd_counts = []
    qd_polar_bin_areas = []
    for r_bin_idx in range(n_of_r_bins):
        qd_counts.append([])
        qd_polar_bin_areas.append([])
        for theta_bin_idx in range(n_of_theta_bins_r[r_bin_idx]):
            qd_counts[r_bin_idx].append(0)
            qd_polar_bin_areas[r_bin_idx].append(0)

    for other_qd_idx in range(len(qds_list)):
        if center_qd_idx != other_qd_idx:
            x_center = qds_list[center_qd_idx]["x"]
            y_center = qds_list[center_qd_idx]["y"]
            x_other = qds_list[other_qd_idx]["x"]
            y_other = qds_list[other_qd_idx]["y"]

            Dx = x_other - x_center
            Dy = y_other - y_center

            r = sqrt(Dx**2 + Dy**2)
            theta = atan2(Dy, Dx)
            if theta == 2*pi:
                theta = 0

            r_bin_idx = floor(r / dr)
            n_of_theta_bins = sample_dict["n_of_theta_bins_r"][r_bin_idx]
            dtheta = 2 * pi / n_of_theta_bins
            theta_bin_idx = floor(theta / dtheta)

            qd_counts[r_bin_idx][theta_bin_idx] += 1
            if [r_bin_idx, theta_bin_idx] not in bins_area_used:
                this_bin_area = compute_polar_bin_area(sample_dict, center_qd_idx,
other_qd_idx, r_bin_idx, theta_bin_idx)
                qd_polar_bin_areas[r_bin_idx][theta_bin_idx] += this_bin_area
                bins_area_used.append([r_bin_idx, theta_bin_idx])

    qd_pfc = []
    for r_bin_idx in range(n_of_r_bins):
        qd_pfc.append([])
        for theta_bin_idx in range(n_of_theta_bins_r[r_bin_idx]):
            qd_counts_r_theta = qd_counts[r_bin_idx][theta_bin_idx]
            qd_polar_bin_areas_r_theta = qd_polar_bin_areas[r_bin_idx][theta_bin_idx]
            if qd_counts_r_theta != 0:
                qd_pfc[r_bin_idx].append(qd_counts_r_theta / qd_polar_bin_areas_r_theta)
            else:
                qd_pfc[r_bin_idx].append(0)
    image_dict["image_single_qd_pfcs"].append(qd_pfc)

def compute_sample_polar_bins (sample_dict, dr_multiplier):
    sample_avg_NN_distance = sample_dict["sample_avg_NN_distance"]
    sample_max_separation = sample_dict["sample_max_separation"]
    dr = dr_multiplier * sample_avg_NN_distance
    sample_dict["dr"] = dr
    n_of_r_bins = ceil(sample_max_separation / dr) + 1
    sample_dict["n_of_r_bins"] = n_of_r_bins
```

```
133
134     r_bins_inner_val = []
135     r_bins_center_val = []
136     r_bins_outer_val = []
137     nr_bins_inner_val = []
138     nr_bins_center_val = []
139     nr_bins_outer_val = []
140     for r_bin_idx in range(n_of_r_bins):
141         r_inner_val = r_bin_idx * dr
142         r_bins_inner_val.append(r_inner_val)
143         r_center_val = r_inner_val + dr/2
144         r_bins_center_val.append(r_center_val)
145         r_outer_val = r_center_val + dr/2
146         r_bins_outer_val.append(r_outer_val)
147         nr_bins_inner_val.append(r_inner_val / sample_avg_NN_distance)
148         nr_bins_center_val.append(r_center_val / sample_avg_NN_distance)
149         nr_bins_outer_val.append(r_outer_val / sample_avg_NN_distance)
150     sample_dict["r_bins_inner_val"] = r_bins_inner_val
151     sample_dict["r_bins_center_val"] = r_bins_center_val
152     sample_dict["r_bins_outer_val"] = r_bins_outer_val
153     sample_dict["nr_bins_inner_val"] = nr_bins_inner_val
154     sample_dict["nr_bins_center_val"] = nr_bins_center_val
155     sample_dict["nr_bins_outer_val"] = nr_bins_outer_val
156
157     theta_bins_cw_val_r = []
158     theta_bins_center_val_r = []
159     theta_bins_ccw_val_r = []
160     dtheta_r = []
161     n_of_theta_bins_r = []
162     for r_bin_idx in range(n_of_r_bins):
163         theta_bins_cw_val_r.append([])
164         theta_bins_center_val_r.append([])
165         theta_bins_ccw_val_r.append([])
166         r = r_bins_outer_val[r_bin_idx]
167         dtheta_approx = dr / r
168         n_of_theta_bins = int(2 * pi / dtheta_approx)
169         n_of_theta_bins_r.append(n_of_theta_bins)
170         dtheta = 2 * pi / n_of_theta_bins
171         dtheta_r.append(dtheta)
172         for theta_bin_idx in range(n_of_theta_bins_r[r_bin_idx]):
173             theta_bins_cw_val_r[r_bin_idx].append(theta_bin_idx * dtheta)
174
    theta_bins_center_val_r[r_bin_idx].append(theta_bins_cw_val_r[r_bin_idx][theta_bin_idx] +
    dtheta/2)
175
    theta_bins_ccw_val_r[r_bin_idx].append(theta_bins_center_val_r[r_bin_idx][theta_bin_idx]
    + dtheta/2)
176     sample_dict["theta_bins_cw_val_r"] = theta_bins_cw_val_r
177     sample_dict["theta_bins_center_val_r"] = theta_bins_center_val_r
178     sample_dict["theta_bins_ccw_val_r"] = theta_bins_ccw_val_r
179     sample_dict["dtheta_r"] = dtheta_r
180     sample_dict["n_of_theta_bins_r"] = n_of_theta_bins_r
181     r_theta_bin_is_used = []
182     for image_idx in range(len(sample_dict["images_list"])):
183         r_theta_bin_is_used.append([])
```

```
184         for r_bin_idx in range(n_of_r_bins):
185             r_theta_bin_is_used[image_idx].append([])
186             for theta_bin_idx in range(n_of_theta_bins_r[r_bin_idx]):
187                 r_theta_bin_is_used[image_idx][r_bin_idx].append(False)
188     sample_dict["r_theta_bin_is_used"] = r_theta_bin_is_used
189 
190 def compute_polar_bin_area (sample_dict, center_qd_idx, other_qd_idx, r_bin_idx,
    theta_bin_idx):
191     r_bins_inner_val = sample_dict["r_bins_inner_val"]
192     inner_r = r_bins_inner_val[r_bin_idx]
193     r_bins_outer_val = sample_dict["r_bins_outer_val"]
194     outer_r = r_bins_outer_val[r_bin_idx]
195     n_of_theta_bins = sample_dict["n_of_theta_bins_r"][r_bin_idx]
196     dtheta = 2 * pi / n_of_theta_bins
197 
198     annulus_sector_area = (outer_r**2 - inner_r**2) * (dtheta / 2)
199 
200     return annulus_sector_area
201 
202 def save_sample_polar_separations_to_file (sample_dict, output_dir):
203     sample_n_str = sample_dict["sample_n_str"]
204     output_filename = "{}.polar_sep.dat".format(sample_n_str)
205     sample_avg_NN_distance = sample_dict["sample_avg_NN_distance"]
206     file_ID = open(output_dir + output_filename, 'w')
207 
208     # header lines
209     SH_lines_char_skip = 23
210     SH_lines_n = 4
211     file_ID.write("# MH SH_lines_char_skip: {0:d}".format(SH_lines_char_skip))
212     file_ID.write(_newl)
213     file_ID.write("# MH SH_lines_n: {0:d}".format(SH_lines_n))
214     file_ID.write(_newl)
215     # short names
216     file_ID.write("# SH short_names:".ljust(SH_lines_char_skip))
217     file_ID.write("r" + _tab)
218     file_ID.write("nr" + _tab)
219     file_ID.write("theta" + _tab)
220     file_ID.write("thetaDeg")
221     file_ID.write(_newl)
222     # Long names
223     file_ID.write("# SH long_names:".ljust(SH_lines_char_skip))
224     file_ID.write("QD separation r" + _tab)
225     file_ID.write("Normalized QD separation" + _tab)
226     file_ID.write("QD separation \g(t)" + _tab)
227     file_ID.write("QD separation \g(t)")
228     file_ID.write(_newl)
229     # units
230     file_ID.write("# SH units:".ljust(SH_lines_char_skip))
231     file_ID.write("nm" + _tab)
232     file_ID.write("-" + _tab)
233     file_ID.write("rad" + _tab)
234     file_ID.write("deg")
235     file_ID.write(_newl)
236     # User variable: sample number
237     file_ID.write("# SH usr_var sample_n:".ljust(SH_lines_char_skip))
```

```
238     file_ID.write(sample_n_str + _tab)
239     file_ID.write(sample_n_str + _tab)
240     file_ID.write(sample_n_str + _tab)
241     file_ID.write(sample_n_str)
242     file_ID.write(_newl)
243     # VALUES
244     for image_dict in sample_dict["images_list"]:
245         qds_list = image_dict["qds_list"]
246         for center_qd_idx in range(len(qds_list)):
247             for other_qd_idx in range(len(qds_list)):
248                 if center_qd_idx != other_qd_idx:
249                     x_center = qds_list[center_qd_idx]["x"]
250                     y_center = qds_list[center_qd_idx]["y"]
251                     x_other = qds_list[other_qd_idx]["x"]
252                     y_other = qds_list[other_qd_idx]["y"]
253 
254                     Dx = x_other - x_center
255                     Dy = y_other - y_center
256 
257                     r = sqrt(Dx**2 + Dy**2)
258                     nr = r / sample_avg_NN_distance
259                     theta = atan2(Dy, Dx)
260                     if theta == 2*pi:
261                         theta = 0
262                     theta_deg = 180 * theta / pi
263                     file_ID.write("{}".format(r) + _tab)
264                     file_ID.write("{}".format(nr) + _tab)
265                     file_ID.write("{}".format(theta) + _tab)
266                     file_ID.write("{}".format(theta_deg))
267                     file_ID.write(_newl)
268     file_ID.close()
269 
270 def save_sample_polar_pcf_to_file (sample_dict, output_dir, dr_multiplier):
271     sample_n_str = sample_dict["sample_n_str"]
272 #     dr_multiplier = sample_dict["dr_multiplier"]
273     sample_avg_NN_distance = sample_dict["sample_avg_NN_distance"]
274     sample_n_of_qds = sample_dict["sample_n_of_qds"]
275     sample_qd_density = sample_dict["sample_qd_density"]
276     r_bins_center_val = sample_dict["r_bins_center_val"]
277     nr_bins_center_val = sample_dict["nr_bins_center_val"]
278     theta_bins_center_val_r = sample_dict["theta_bins_center_val_r"]
279     sample_polar_pfc = sample_dict["sample_polar_pfc"]
280     sample_polar_pfc_var = sample_dict["sample_polar_pfc_var"]
281     sample_polar_pfc_std = sample_dict["sample_polar_pfc_std"]
282     sample_polar_pfc_stderr = sample_dict["sample_polar_pfc_stderr"]
283 
284     output_filename = "{0}_drm{1:.2f}.ppfc.dat".format(sample_n_str, dr_multiplier)
285     output_file_path = output_dir + output_filename
286 
287     file_ID = open(output_file_path, 'w')
288 
289     # header lines
290     SH_lines_char_skip = 23
291     SH_lines_n = 11
292     file_ID.write("# MH SH_lines_char_skip: {0:d}".format(SH_lines_char_skip))
```

```
293     file_ID.write(_newl)
294     file_ID.write("# MH SH_lines_n: {0:d}".format(SH_lines_n))
295     file_ID.write(_newl)
296     # short names
297     file_ID.write("# SH short_names:".ljust(SH_lines_char_skip))
298     file_ID.write("rM{0:.2f}".format(dr_multiplier) + _tab)
299     file_ID.write("nrM{0:.2f}".format(dr_multiplier) + _tab)
300     file_ID.write("thM{0:.2f}".format(dr_multiplier) + _tab)
301     file_ID.write("degthM{0:.2f}".format(dr_multiplier) + _tab)
302     file_ID.write("ppcfM{0:.2f}".format(dr_multiplier) + _tab)
303     file_ID.write("ppcfvarM{0:.2f}".format(dr_multiplier) + _tab)
304     file_ID.write("ppcfstdM{0:.2f}".format(dr_multiplier) + _tab)
305     file_ID.write("ppcfsterrM{0:.2f}".format(dr_multiplier))
306     file_ID.write(_newl)
307     # Long names
308     file_ID.write("# SH long_names:".ljust(SH_lines_char_skip))
309     file_ID.write("QD separation" + _tab)
310     file_ID.write("Normalized QD separation" + _tab)
311     file_ID.write("Polar angle" + _tab)
312     file_ID.write("Polar angle" + _tab)
313     file_ID.write("Polar PCF" + _tab)
314     file_ID.write("Polar PCF variance" + _tab)
315     file_ID.write("Polar PCF standard deviation" + _tab)
316     file_ID.write("Polar PCF standard error")
317     file_ID.write(_newl)
318     # units
319     file_ID.write("# SH units:".ljust(SH_lines_char_skip))
320     file_ID.write("nm" + _tab)
321     file_ID.write("-" + _tab)
322     file_ID.write("rad" + _tab)
323     file_ID.write("deg" + _tab)
324     file_ID.write("-" + _tab)
325     file_ID.write("-" + _tab)
326     file_ID.write("-" + _tab)
327     file_ID.write("-")
328     file_ID.write(_newl)
329     # Comments
330     file_ID.write("# SH comments:".ljust(SH_lines_char_skip))
331     file_ID.write("-" + _tab)
332     file_ID.write("-" + _tab)
333     file_ID.write("-" + _tab)
334     file_ID.write("-" + _tab)
335     file_ID.write("-" + _tab)
336     file_ID.write("-" + _tab)
337     file_ID.write("-" + _tab)
338     file_ID.write("-")
339     file_ID.write(_newl)
340     # User variable: sample number
341     file_ID.write("# SH usr_var sample_n:".ljust(SH_lines_char_skip))
342     file_ID.write("-" + _tab)
343     file_ID.write(sample_n_str + _tab)
344     file_ID.write("-" + _tab)
345     file_ID.write(sample_n_str + _tab)
346     file_ID.write(sample_n_str + _tab)
347     file_ID.write(sample_n_str + _tab)
```

```
348     file_ID.write(sample_n_str + _tab)
349     file_ID.write(sample_n_str)
350     file_ID.write(_newl)
351     # User variable: average dNN
352     file_ID.write("# SH usr_var avg_dNN:".ljust(SH_lines_char_skip))
353     file_ID.write("-" + _tab)
354     file_ID.write("{0:.2f} nm".format(sample_avg_NN_distance) + _tab)
355     file_ID.write("-" + _tab)
356     file_ID.write("-" + _tab)
357     file_ID.write("{0:.2f} nm".format(sample_avg_NN_distance) + _tab)
358     file_ID.write("{0:.2f} nm".format(sample_avg_NN_distance) + _tab)
359     file_ID.write("{0:.2f} nm".format(sample_avg_NN_distance) + _tab)
360     file_ID.write("{0:.2f} nm".format(sample_avg_NN_distance))
361     file_ID.write(_newl)
362     # User variable: dNN multiplier
363     file_ID.write("# SH usr_var dNN_mult:".ljust(SH_lines_char_skip))
364     file_ID.write("-" + _tab)
365     file_ID.write("{0:.2f}".format(dr_multiplier) + _tab)
366     file_ID.write("-" + _tab)
367     file_ID.write("-" + _tab)
368     file_ID.write("{0:.2f}".format(dr_multiplier) + _tab)
369     file_ID.write("{0:.2f}".format(dr_multiplier) + _tab)
370     file_ID.write("{0:.2f}".format(dr_multiplier) + _tab)
371     file_ID.write("{0:.2f}".format(dr_multiplier))
372     file_ID.write(_newl)
373     # User variable: n. of QDs
374     file_ID.write("# SH usr_var n_of_QDs:".ljust(SH_lines_char_skip))
375     file_ID.write("-" + _tab)
376     file_ID.write("-" + _tab)
377     file_ID.write("-" + _tab)
378     file_ID.write("-" + _tab)
379     file_ID.write("{0:d}".format(sample_n_of_qds) + _tab)
380     file_ID.write("{0:d}".format(sample_n_of_qds) + _tab)
381     file_ID.write("{0:d}".format(sample_n_of_qds) + _tab)
382     file_ID.write("{0:d}".format(sample_n_of_qds))
383     file_ID.write(_newl)
384     # User variable: density in nm-2
385     file_ID.write("# SH usr_var img_dens:".ljust(SH_lines_char_skip))
386     file_ID.write("-" + _tab)
387     file_ID.write("-" + _tab)
388     file_ID.write("-" + _tab)
389     file_ID.write("-" + _tab)
390     file_ID.write("{0:1.2e} nm-2".format(sample_qd_density) + _tab)
391     file_ID.write("{0:1.2e} nm-2".format(sample_qd_density) + _tab)
392     file_ID.write("{0:1.2e} nm-2".format(sample_qd_density) + _tab)
393     file_ID.write("{0:1.2e} nm-2".format(sample_qd_density))
394     file_ID.write(_newl)
395     # User variable: maximum
396     file_ID.write("# SH usr_var max:".ljust(SH_lines_char_skip))
397     file_ID.write("-" + _tab)
398     file_ID.write("-" + _tab)
399     file_ID.write("-" + _tab)
400     file_ID.write("-" + _tab)
401     file_ID.write("{0:.2f}".format(max(max(sample_polar_pfc))) + _tab)
402     file_ID.write("{0:.2f}".format(max(max(sample_polar_pfc_var))) + _tab)
```

```
403     file_ID.write("{0:.2f}".format(max(max(sample_polar_pfc_std))) + _tab)
404     file_ID.write("{0:.2f}".format(max(max(sample_polar_pfc_stderr))))
405     file_ID.write(_newl)
406     # User variable: minimum
407     file_ID.write("# SH usr_var min:".ljust(SH_lines_char_skip))
408     file_ID.write("-" + _tab)
409     file_ID.write("-" + _tab)
410     file_ID.write("-" + _tab)
411     file_ID.write("-" + _tab)
412     file_ID.write("{0:.2f}".format(min(min(sample_polar_pfc))) + _tab)
413     file_ID.write("{0:.2f}".format(min(min(sample_polar_pfc_var))) + _tab)
414     file_ID.write("{0:.2f}".format(min(min(sample_polar_pfc_std))) + _tab)
415     file_ID.write("{0:.2f}".format(min(min(sample_polar_pfc_stderr))))
416     file_ID.write(_newl)
417 
418     #values
419     for r_value_idx in range(len(r_bins_center_val)):
        for theta_value_idx in range(len(theta_bins_center_val_r[r_value_idx])):
420             curr_datapoint_r_value = r_bins_center_val[r_value_idx]
421             curr_datapoint_nr_value = nr_bins_center_val[r_value_idx]
422             curr_datapoint_theta_value =
    theta_bins_center_val_r[r_value_idx][theta_value_idx]
423             curr_datapoint_deg_theta_value = 180 * curr_datapoint_theta_value / pi
424             curr_datapoint_pfc_value = sample_polar_pfc[r_value_idx][theta_value_idx]
425             curr_datapoint_pfc_var_value =
    sample_polar_pfc_var[r_value_idx][theta_value_idx]
426             curr_datapoint_pfc_std_value =
    sample_polar_pfc_std[r_value_idx][theta_value_idx]
427             curr_datapoint_pfc_stderr_value =
    sample_polar_pfc_stderr[r_value_idx][theta_value_idx]
428 
429             file_ID.write("{0}".format(curr_datapoint_r_value) + _tab)
430             file_ID.write("{0}".format(curr_datapoint_nr_value) + _tab)
431             file_ID.write("{0}".format(curr_datapoint_theta_value) + _tab)
432             file_ID.write("{0}".format(curr_datapoint_deg_theta_value) + _tab)
433             file_ID.write("{0}".format(curr_datapoint_pfc_value) + _tab)
434             file_ID.write("{0}".format(curr_datapoint_pfc_var_value) + _tab)
435             file_ID.write("{0}".format(curr_datapoint_pfc_std_value) + _tab)
436             file_ID.write("{0}".format(curr_datapoint_pfc_stderr_value))
437             file_ID.write(_newl)
438 
439     file_ID.close()
```

A.1.3.3 Functions library for reading and processing QD positions data

general_qds_manipulation.py

```
1  from math import sqrt
2 
3  _verbose = True
4  _save_separations_to_file = True
5 
6  _tab = "\t"
7  _newl = "\n"
```

```
 8
 9  def load_images_info (input_file_path):
10      if _verbose: print("â—‹ Loading images info...")
11      image_files_dict = {}
12      file_ID = open(input_file_path, 'r')
13      line_n = 1
14      for line in file_ID:
15          line = line.strip()
16          line = line.split("\t")
17          if line_n == 1:
18              for element in line:
19                  image_files_dict[element] = {}
20                  image_files_dict[element]["values"] = []
21          elif line_n == 2:
22              j = 0
23              for column in image_files_dict:
24                  image_files_dict[column]["units"] = line[j]
25                  j += 1
26          else:
27              j = 0
28              for column in image_files_dict:
29                  image_files_dict[column]["values"].append(line[j])
30                  j += 1
31          line_n += 1
32      file_ID.close()
33      if _verbose: print("● Done loading images info.")
34      return image_files_dict
35
36  def generate_samples_dict (image_files_dict):
37      if _verbose: print("○ Generating samples dictionary...")
38      samples_dict = {}
39      for image_idx in range(len(image_files_dict["sample_n_str"]["values"])):
40          sample_n_str = image_files_dict["sample_n_str"]["values"][image_idx]
41          if sample_n_str not in samples_dict:
42              # first time encountering sample "sample_n_str"
43              # create the relevant single sample_dict and its images_list
44              samples_dict[sample_n_str] = {}
45              samples_dict[sample_n_str]["sample_n_str"] = sample_n_str
46              samples_dict[sample_n_str]["images_list"] = []
47              samples_dict[sample_n_str]["n_of_images"] = 0
48              samples_dict[sample_n_str]["images_total_area"] = 0
49              # add the new image to the images_list
50              image_dict = {}
51              # add here other keys from image_files_dict as needed, remember to
52              # add them below in the else too though
53              image_dict["min_qd_diam"] =\
54                  image_files_dict["min_qd_diam"]["values"][image_idx]
55              image_dict["image_size_str"] =\
56                  image_files_dict["image_size"]["values"][image_idx]
57              image_dict["image_side_size"] = \
58                  1e3*float(image_files_dict["image_size"]["values"][image_idx])
59              image_dict["image_area_size"] =\
60                  image_dict["image_side_size"]**2 # nm²
61              image_dict["image_n_str"] =\
62                  image_files_dict["image_n"]["values"][image_idx]
```

```
63              samples_dict[sample_n_str]["n_of_images"] =\
64                  samples_dict[sample_n_str]["n_of_images"] + 1
65              samples_dict[sample_n_str]["images_list"].append(image_dict)
66              samples_dict[sample_n_str]["images_total_area"] +=
                    image_dict["image_area_size"]
67          else:
68              image_dict = {}
69              # add here other keys from image_files_dict as needed
70              samples_dict[sample_n_str]["sample_n_str"] = sample_n_str
71              image_dict["min_qd_diam"] =\
72                  image_files_dict["min_qd_diam"]["values"][image_idx]
73              image_dict["image_size_str"] =\
74                  image_files_dict["image_size"]["values"][image_idx]
75              image_dict["image_side_size"] =\
76                  1e3*float(image_files_dict["image_size"]["values"][image_idx]) # nm
77              image_dict["image_area_size"] =\
78                  image_dict["image_side_size"]**2 # nm²
79              image_dict["image_n_str"] =\
80                  image_files_dict["image_n"]["values"][image_idx]
81              samples_dict[sample_n_str]["n_of_images"] =\
82                  samples_dict[sample_n_str]["n_of_images"] + 1
83              samples_dict[sample_n_str]["images_list"].append(image_dict)
84              samples_dict[sample_n_str]["images_total_area"] +=
                    image_dict["image_area_size"]
85      if _verbose: print("â—  Done generating samples dictionary.")
86      return samples_dict
87
88  def load_qds_positions (input_dir, samples_dict):
89      if _verbose: print("â—‹ Loading qds positions...")
90      for sample_n_str in samples_dict:
91          sample_dict = samples_dict[sample_n_str]
92          sample_n_of_qds = 0
93          for image_dict in sample_dict["images_list"]:
94              image_n_of_qds = 0
95              image_dict["qds_list"] = []
96              image_n = image_dict["image_n_str"]
97              image_size_str = image_dict["image_size_str"]
98              filename = sample_n_str + "_" + image_size_str + "um." + image_n + ".xy.dat"
99              input_path = input_dir + filename
100             # load the QDs xy positions
101             file = open(input_path, 'r')
102             for line in file:
103                 line = line.strip()
104                 line = line.split("\t")
105                 image_dict["qds_list"].append({"x": float(line[0]), "y":float(line[1])})
106                 image_n_of_qds = image_n_of_qds + 1
107             file.close()
108             image_dict["n_of_qds"] = image_n_of_qds
109             sample_n_of_qds += image_n_of_qds
110             compute_image_max_separation(image_dict)
111             compute_image_min_separation(image_dict)
112         compute_sample_max_separation(sample_dict)
113         compute_sample_min_separation(sample_dict)
114         samples_dict[sample_n_str]["sample_n_of_qds"] = sample_n_of_qds
115         samples_dict[sample_n_str]["sample_qd_density"] =\
```

```
            samples_dict[sample_n_str]["sample_n_of_qds"] / \
            samples_dict[sample_n_str]["images_total_area"]
    if _verbose: print("â—  Done loading qds positions.")

def compute_samples_separations_list (samples_dict):
    if _verbose: print("â—‹ Computing samples separations list...")
    for sample_n_str in samples_dict:
        if _verbose: print(_tab + sample_n_str)
        sample_avg_NN_distance = 0
        sample_n_of_QDs = 0
        image_idx = 1
        sample_separation_list = []
        for image_dict in samples_dict[sample_n_str]["images_list"]:
            if _verbose: print(2*_tab + "Image n. " + repr(image_idx))
            compute_image_separations_list(image_dict)
            sample_separation_list = sample_separation_list +
               image_dict["separations_list"]
            for QD_NNd_dict in image_dict["separations_list"]:
                sample_avg_NN_distance += QD_NNd_dict["ref_qd_NN_dist"]
            sample_n_of_QDs += image_dict["n_of_qds"]
            image_idx += 1
        sample_avg_NN_distance = sample_avg_NN_distance / sample_n_of_QDs
        samples_dict[sample_n_str]["sample_avg_NN_distance"] = sample_avg_NN_distance
        samples_dict[sample_n_str]["sample_separation_list"] = sample_separation_list
    if _verbose: print("â—  Done computing samples separations list.")

def compute_image_separations_list (image_dict):
    qds_list = image_dict["qds_list"]
    separations_list = []
    image_n_of_qds = image_dict["n_of_qds"]

    image_avg_NN_distance = 0
    for ref_qd_idx in range(image_n_of_qds):
        ref_qd_NN_dist = -1
        for other_qd_idx in range (ref_qd_idx + 1, image_n_of_qds):
            x_0 = qds_list[ref_qd_idx]["x"]
            y_0 = qds_list[ref_qd_idx]["y"]
            x_1 = qds_list[other_qd_idx]["x"]
            y_1 = qds_list[other_qd_idx]["y"]
            r = sqrt((x_1 - x_0)**2 + (y_1 - y_0)**2)

            if (ref_qd_NN_dist == -1) or (ref_qd_NN_dist > r):
                ref_qd_NN_dist = r

        separations_list.append({"ref_QD_idx": ref_qd_idx,\
                                 "ref_qd_NN_dist": ref_qd_NN_dist})
        image_avg_NN_distance += ref_qd_NN_dist
    image_avg_NN_distance = image_avg_NN_distance / image_n_of_qds
    image_dict["image_avg_NN_distance"] = image_avg_NN_distance
    image_dict["separations_list"] = separations_list

def compute_separation (qds_list, qd_idx_i, qd_idx_j):
    x_0 = qds_list[qd_idx_i]["x"]
    y_0 = qds_list[qd_idx_i]["y"]
    x_1 = qds_list[qd_idx_j]["x"]
```

```
    y_1 = qds_list[qd_idx_j]["y"]
    return sqrt((x_1 - x_0)**2 + (y_1 - y_0)**2)

def compute_image_max_separation (image_dict):
    qds_list = image_dict["qds_list"]
    max_separation = 0
    for center_qd in qds_list:
        x_0 = center_qd["x"]
        y_0 = center_qd["y"]
        for other_qd in qds_list:
            x_1 = other_qd["x"]
            y_1 = other_qd["y"]
            separation  = sqrt((x_1 - x_0)**2 + (y_1 - y_0)**2)
            if separation > max_separation: max_separation = separation
    image_dict["max_separation"] = max_separation

def compute_image_min_separation (image_dict):
    qds_list = image_dict["qds_list"]
    min_separation = image_dict["max_separation"]
    for center_qd in qds_list:
        x_0 = center_qd["x"]
        y_0 = center_qd["y"]
        for other_qd in qds_list:
            if center_qd is not other_qd:
                x_1 = other_qd["x"]
                y_1 = other_qd["y"]
                separation  = sqrt((x_1 - x_0)**2 + (y_1 - y_0)**2)
                if separation < min_separation: min_separation = separation
    image_dict["min_separation"] = min_separation

def compute_sample_max_separation (sample_dict):
    sample_max_separation = 0
    for image_dict in sample_dict["images_list"]:
        image_max_separation = image_dict["max_separation"]
        if image_max_separation > sample_max_separation:
            sample_max_separation = image_max_separation
    sample_dict["sample_max_separation"] = sample_max_separation # nm

def compute_sample_min_separation (sample_dict):
    sample_min_separation = sample_dict["sample_max_separation"]
    for image_dict in sample_dict["images_list"]:
        image_min_separation = image_dict["min_separation"]
        if image_min_separation < sample_min_separation:
            sample_min_separation = image_min_separation
    sample_dict["sample_min_separation"] = sample_min_separation # nm
```

A.2 Local substrate curvature from AFM line-cuts

A.2.1 Introduction

In this appendix we describe the method used to compute the curvature of the AFM line-cuts used for the phase-field simulations in Ch. 3. We introduce the curvature formula and describe the practical implementation of the curvature calculation in the case of a discrete data set, such as for AFM line-cuts, then we present the MATLAB code employed for the calculation of curvatures described in Ch. 3.

A.2.2 Method

This section contains the detailed procedure used for the computation of the curvature of AFM substrate profiles used for the phase-field simulations in Ch. 3. The rationale behind the choice of performing a polynomial fit of the surface profile is explained, then the mathematical steps for the computation of the curvature are described.

We compute the curvature $\kappa_z(x)$ of a curve $z(x)$ as:

$$\kappa_z(x) = \frac{z''(x)}{(1 + z'(x)^2)^{3/2}}, \tag{A.7}$$

where $z'(x)$ and $z''(x)$ are the first and second derivative of the surface profile $z(x)$. Some kind of differentiation of the experimental profile is therefore required.

The AFM line-cuts measuring the surface profiles employed in Ch. 3 both are 1 μm long and comprise 512 data points, corresponding to Δx = 1.95 nm between data points. One may therefore be tempted to perform the differentiation of the profile $z(x_i)$ as:

$$z'(x_i) = \frac{z(x_{i+1}) - z(x_i)}{\Delta x} \tag{A.8}$$

and

$$z''(x_i) = \frac{z'(x_{i+1}) - z'(x_i)}{\Delta x}, \tag{A.9}$$

where i represents the *i*-th data point. We found however this method to lead to excessively noisy results, presumably due to the AFM-related noise in the $z(x_i)$, therefore, we opted to perform a polynomial fit of $z(x_i)$, and algebraic differentiation of the polynomial fit, for the computation of the curvature.

Since a single polynomial fit of the entire L = 1 μm line-cut is not feasible, we perform for each data point i a 4th order polynomial fit of $z(x_i)$ in a "window" $[x_i - d/2, x_i + d/2]$ of width d, centered around x_i. For the value of the window width d, in order to calculate the curvature on a length scale comparable to the QDs which were phase-field-simulated on these line-cuts, we found it natural to use the average diameter of the QDs. For the "beginning" and "end" regions of the line-cut, i.e. those regions where $x_i < d/2$ and $x_i > L - d/2$, respectively, the "window" is simply truncated to the edge of the line-cut, resulting in $[0, x_i + d/2]$ and $[x_i - d/2, L]$, respectively.

Once the polynomial fit is obtained:

$$P_i(x) = a_4^{(i)}x^4 + a_3^{(i)}x^3 + a_2^{(i)}x^2 + a_1^{(i)}x + a_0^{(i)}, \tag{A.10}$$

with $a_j^{(i)}$ as the j-th order polynomial fit coefficients for the fit performed centering on x_i, the derivatives of the polynomial fit are computed:

$$P_i'(x) = 4a_4^{(i)}x^3 + 3a_3^{(i)}x^2 + 2a_2^{(i)}x + a_1^{(i)}, \tag{A.11}$$

and

$$P_i''(x) = 12a_4^{(i)}x^2 + 6a_3^{(i)}x + 2a_2^{(i)}. \tag{A.12}$$

The polynomial fit-derived derivatives z_p' and z_p'' of the AFM line-cut profile z for the x position x_i ($z_p'(x_i)$, $z_p''(x_i)$, and $z(x_i)$, respectively) are consequently computed as:

$$z_p'(x_i) = 4a_4^{(i)}{x_i}^3 + 3a_3^{(i)}{x_i}^2 + 2a_2^{(i)}x_i + a_1^{(i)}, \quad \text{A.13}$$

and

$$z_p''(x_i) = 12a_4^{(i)}{x_i}^2 + 6a_3^{(i)}x_i + 2a_2^{(i)}. \quad \text{A.14}$$

Finally, the curvature κ_z can be computed for each x_i using Eq. A.7:

$$\kappa_z(x_i) = \frac{z_p''(x_i)}{\left(1 + z_p'(x_i)^2\right)^{3/2}}, \quad \text{A.15}$$

We show the result of the curvature computation in Fig. A.1 for both the flat and mounded surfaces discussed in Ch. 3. Fig. A.1(a) and (b) show the calculated curvature for the flat and mounded, respectively, AFM surface line-cuts in Fig. A.1(c) and (d), respectively. The line-cut in Fig. A.1(c) has been chosen to center around a surface mound (~500 nm to ~600 nm). In Fig. A.1(a) and (b) the ranges of curvature values of [-0.004, -0.002] ("high mountains"), (-0.002, 0] ("low mountains"), (0, 0,002] ("shallow valleys"), and (0.002, 0.004] ("deep valleys") are high-lighted with red, yellow, green, and blue bands, respectively. Correspondingly, for the line-cuts in Fig. A.1(c) and (d), the regions with curvature within the ranges of [-0.004, -0.002], (-0.002, 0], (0, 0,002], and (0.002, 0.004] are highlighted in red, yellow, green, and blue, respectively. For the flat surface in Fig. A.1(c), the total curvature range is more limited than with the mounded surface in Fig. A.1(c), resulting in curvatures only within the (-0.002, 0] (low mountains, yellow) and (0, 0,002] (shallow valleys, green). For the mounded surface in Fig. A.1(d), however, the curvature values reach also the ranges of [-0.004, -0.002] (high mountains, red) and (0.002, 0.004] (deep valleys, green). It is interesting to note that one prominent region of large negative curvature (high mountain, red) is revealed to be the top of the mound (~750 nm to ~850 nm), while a prominent

region of large positive curvature (deep valleys, blue) is revealed to be a side of the mound (~600 nm to ~620 nm), as expected following the study in Ch. 3.

A.2.3 MATLAB code

```
clear
close all
clc

%% run parameters

% switches ==============================||
% choose buffer -------------------------|
buffer_id = 'flat\';
% buffer_id = 'mounds\';
% choose order of the polynomial fit -----|
polynomial_order = 4;
% ---------------------------------------|
final_plot = 1;
interim_plots = 0;
plot_fit = 1;
plot_derivatives = 1;
plot_curvature = 1;
% =======================================||

if strcmp(buffer_id, 'flat\')
    window_width = 40; % nm
else
    window_width = 40; % nm
end

%% file paths

data_folder = 'exported_data\';

file_x = [data_folder buffer_id 'x.dat'];
file_buffer_z = [data_folder buffer_id 'buffer_z.dat'];

%% read data

fID = fopen(file_x, 'r');
x = fscanf(fID, '%f');
dx = x(2) - x(1);
fclose(fID);

fID = fopen(file_buffer_z, 'r');
buffer_z = fscanf(fID, '%f');
fclose(fID);

%% Calculate curvatures

[~, window_index_width] = min(abs(x-window_width));
if mod(window_index_width, 2) ==1
```

```
49      window_index_width = window_index_width + 1;
50  end
51  half_window = window_index_width/2;
52
53  der1 = zeros(numel(x), 1);
54  der2 = zeros(numel(x), 1);
55  curvature = zeros(numel(x), 1);
56
57  for i = 1:numel(x)
58      slice_start_index = i-half_window;
59      slice_end_index = i+half_window;
60      if i <= half_window
61          phase = 1;
62          slice_start_index = 1;
63          slice_end_index = 1 + 2*half_window;
64      elseif i >= numel(x)-half_window
65          phase = 2;
66          slice_start_index = numel(x) - 2*half_window;
67          slice_end_index = numel(x);
68      else
69          phase = 3;
70      end
71      x_slice = x(slice_start_index:slice_end_index);
72      buffer_z_slice = buffer_z(slice_start_index:slice_end_index);
73      % polynomial fit
74      p = polyfit(x_slice, buffer_z_slice, polynomial_order);
75      fit = p(1)*x_slice.^4 + p(2)*x_slice.^3 + p(3)*x_slice.^2 + p(4)*x_slice + p(5);
76      fit_der_1 = 4*p(1)*x_slice.^3 + 3*p(2)*x_slice.^2 + 2*p(3)*x_slice + p(4);
77      fit_der_2 = 12*p(1)*x_slice.^2 + 6*p(2)*x_slice + 2*p(3);
78
79      %calculate curvature
80      curvature_fit = fit_der_2./(1 + fit_der_1.^2).^(3/2);
81      curvature_slice = curvature_fit(slice_start_index:slice_end_index);
82      der1(i) = fit_der_1(half_window + 1);
83      der2(i) = fit_der_2(half_window + 1);
84      curvature(i) = curvature_fit(half_window + 1);
85      if interim_plots
86          figure_id = figure;
87          hold on
88          plot(x_slice, buffer_z_slice, 'ko');
89          if plot_fit
90              plot(x_slice, fit_slice, 'r-');
91          end
92          if plot_derivatives
93              plot(x_slice, fit_der_1_slice, 'm-');
94              plot(x_slice, fit_der_2_slice, 'b-');
95          end
96          if plot_curvature
97              plot(x_slice, curvature_slice, 'b.');
98          end
99          waitforbuttonpress;
100         close(figure_id)
101     end
102 end
103
```

```
der_1_diff = diff(buffer_z)/dx;
der_2_diff = diff(der_1_diff)/dx;
curvature_diff = der_2_diff./(1 + der_1_diff(1:numel(der_1_diff)-1).^2).^(3/2);
x_diff = dx + x(1:numel(x)-2);

if final_plot
    figure
    hold on
    plot(x, buffer_z, 'k')
    filter = curvature<=0;
    plot(x(filter),    0.5    +    100*curvature(filter),    'r.',    x(~filter),    0.5    +
                100*curvature(~filter), 'b.')
end

disp("Done.")
```

A.3 Orientation fraction of textured films from coupled XRD spectra

A.3.1 Introduction

This appendix describes the method employed to quantify the preferential orientation of a poly-crystalline film (i.e. "texturing") in Ch. 4.

A.3.2 Method

To quantify and compare the preferential orientations of the layers, we compute the texture coefficient $P(\boldsymbol{h}_i)$ for each detected reflection $\boldsymbol{h}_i = h_i k_i l_i$:

$$P(\boldsymbol{h}_i) = \frac{I(\boldsymbol{h}_i)}{I_p(\boldsymbol{h}_i)} \left[\frac{1}{n} \sum_{i=1}^{n} \frac{I(\boldsymbol{h}_i)}{I_p(\boldsymbol{h}_i)} \right]^{-1}, \tag{A.16}$$

where $I(\boldsymbol{h}_i)$ and $I_p(\boldsymbol{h}_i)$ are the intensity of the measured and reference powder spectra for reflection $\boldsymbol{h}_i$, and n is the number of reflections considered in each spectrum. Thus, $P(\boldsymbol{h}_i) > 1$ indicates a preference for direction $[\boldsymbol{h}_i]$, while $P(\boldsymbol{h}_i) \leq 1$ indicates a lack of preference for direction $[\boldsymbol{h}_i]$.

To evaluate the [1 0 0]-orientation fraction, which is defined as the fraction of vertical [1 0 0]-oriented crystallites,[7] we compute the average $\frac{1}{n}\sum_{i=1}^{n} \eta(\boldsymbol{h}_i)$ for all the reflections $\boldsymbol{h}_i$ of

$$\eta(\boldsymbol{h}_i) = \sqrt{\frac{[1 - r(\boldsymbol{h}_i)]^3}{1 - r(\boldsymbol{h}_i)^3}}, \tag{A.17}$$

where $r(\boldsymbol{h}_i)$ is the parameter[8]

$$r(h_i) = \left[\frac{\sin^2 \alpha(\boldsymbol{h}_i)}{\left(\kappa(\boldsymbol{h}_i) \,/\, \kappa_p(\boldsymbol{h}_i)\right)^{2/3} - \cos^2 \alpha(\boldsymbol{h}_i)} \right]^{\frac{1}{3}}, \tag{A.18}$$

with $\alpha(\boldsymbol{h}_i)$ the angle between the direction $\boldsymbol{h}_i$ and the reference direction [4 0 0], $\kappa(\boldsymbol{h}_i) = I(4\,0\,0) \,/\, I(\boldsymbol{h}_i)$, and $\kappa_p(\boldsymbol{h}_i) = I_p(4\,0\,0) \,/\, I_p(\boldsymbol{h}_i)$.

A.4 Figures

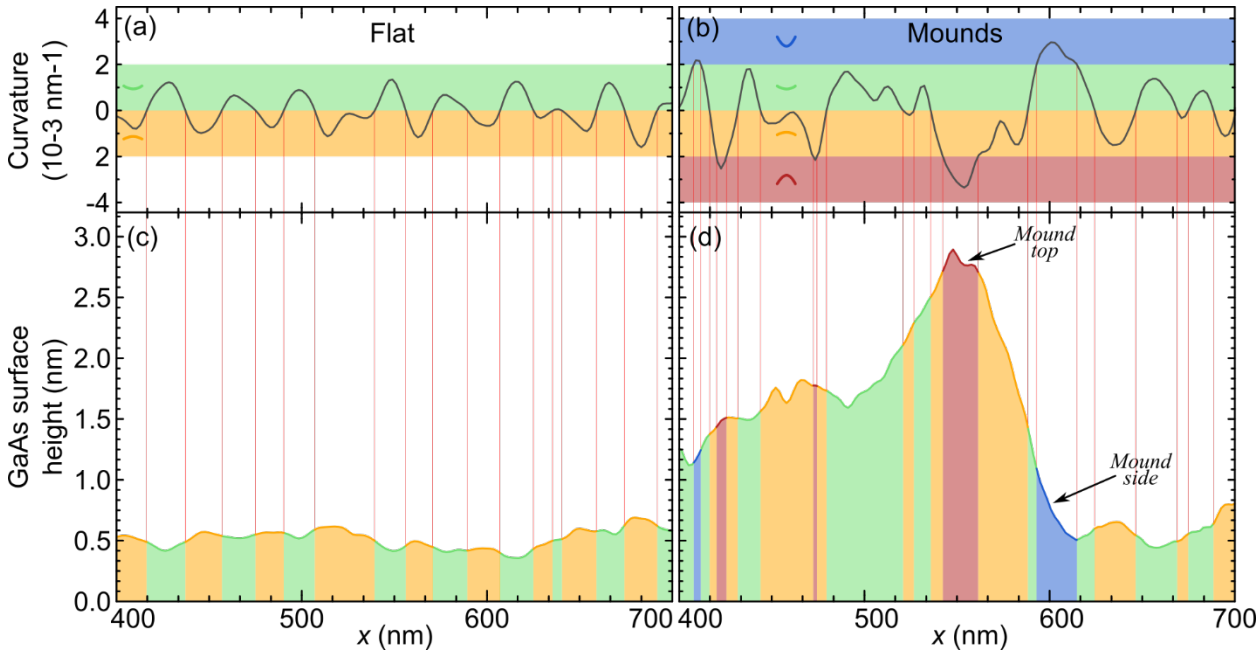

Figure A.1: Surface profile and relative calculated curvature for flat and mounded surfaces. **(a)** Calculated curvature for the flat surface profile in (a), with the positive (negative) curvature values highlighted in green (yellow). **(b)** Calculated curvature for the mound surface profile in (d), with the curvature values in the [-0.004, -0.002], (-0.002, 0], (0, 0,002], and (0.002, 0.004] ranges highlighted in red, yellow, green, and blue, respectively. **(c)** Detail of the flat surface profile used for the phase-field simulation in Ch. 3, with regions of positive (negative) curvature highlighted in green (yellow) **(d)** Detail of the mounded surface profile used for the phase-field simulation in Ch. 3, featuring a mound, with regions of curvature in the [-0.004, -0.002], (-0.002, 0], (0, 0,002], and (0.002, 0.004] ranges highlighted in red, yellow, green, and blue, respectively. It is interesting to note that, as expected, the top of the mound falls in the range of the lowest curvature (high mountain), while the side of the mound falls in the range of the highest curvature (deep valley).

A.5 References

[1] D. Nečas and P. Klapetek, "Gwyddion: an open-source software for SPM data analysis" Open Phys. **10**, 181 (2011).

[2] J. Gleason, "Nanometer-Scale Studies of Point Defect Distributions in Dilute Magnetic Semiconductor Alloys" MSc. dissertation, University of Michigan (2004).

[3] P. Ebert, X. Chen, M. Heinrich, M. Simon, K. Urban, and D. Haarer, "Direct determination of the interaction between vacancies on InP(110) surfaces" Phys. Rev. Lett. 76, 2089 (1996).

[4] K.J. Chao, C.K. Shih, D.W. Gotthold, and B.G. Streetman, "Determination of 2d pair correlations and pair interaction energies of in atoms in molecular beam epitaxially grown InGaAs alloys" Phys. Rev. Lett. 79, 4822 (1997).

[5] We employ here following convention: 0° is in the direction of the positive x axis, and a positive angle increment is in the counter-clockwise direction.

[6] If one is insistent on pursuing this approach, there may be ways of implementing some sort of relaxation mechanism whereby the overlapping QDs may "move apart" until there is no more overlap.

[7] E. Zolotoyabko, "Determination of the degree of preferred orientation within the March-Dollase approach" J. Appl. Crystallogr. 42, 513 (2009).

[8] W.A. Dollase, "Correction of intensities for preferred orientation in powder diffractometry: application of the March model" J. Appl. Crystallogr. **19**, 267 (1986).

Appendix B Single-Nanowire Electronic Transport

B.1 Introduction

This appendix describes the methods developed in the course of this doctoral work to prepare single nanowires (NW) for electronic transport measurements [e.g. current-voltage (I-V) characteristics] and transmission electron microscopy (TEM) measurements, in preparation for the full structural and transport characterization needed to evaluate the usefulness of the NW as active components of a solid-state device.

In the following sections, the preparation of circuits around a NW in a focused-ion beam (FIB) microscope for ex-situ I-V measurements is discussed in Sec. B.2. Next, the technique used in this work for in-situ measuring of the I-V characteristics of a single NW via two nano-manipulators in a FIB is discussed in Sec. B.3.

B.2 Focused-ion beam-deposited circuits of drop-cast nanowires

In this section, the procedure employed to connect a NW to a macroscopic gold circuit deposited on an insulating SiO_2/Si substrate for ex-situ I-V measurements is described. First, the preparation of the SiO_2/Si substrates with the initial patterned gold circuits ("spiders") is described, then the procedure for the transfer of the NW to the Au/SiO_2/Si substrate and the deposition of Pt leads to complete the circuits from the NW to the Au "spiders." Finally, the procedure measuring the I-V characteristics of such-prepared NW in a probe station is described.

B.2.1 Method

For the Au-patterned SiO_2/Si substrates, a set of 6 × 6 = 36 patterns ("spiders") was deposited onto a ~1 × ~1 cm^2 insulating substrate via photolithography. Fig. B.2(a) shows a CAD image of the actual photolithography mask used for the Au deposition on SiO_2. Each of these spiders contained 4 × 2 = 8 (hence "spider") rectangular pads with relative leads. Fig. B.2(b) shows a schematic drawing of one spider. The column and row numbers are lithographed towards the top and the bottom of the spider, respectively, for quick identification in a microscope. The eight 100 × 150 μm pads (named "p1," "p2," "p3," etc.) are organized in four 100 μm-spaced rows, and two columns on the left and right edges of the spider, while the respective leads progressively thin and converge towards the center of the spider. Fig. B.2(c) shows a schematic drawing of the center of a spider, where the eight leads converge in four parallel couples towards the edges of an 8 × 8 μm^2 empty square space, designed to accommodate the NW that will be connected to the Au leads. The final stretch of each Au lead is 9 μm long and 1 μm wide, with each couple of parallel leads separated by 1.5 μm.

After the deposition of the previously described Au leads on the insulating SiO_2 substrate, the NW are transferred onto the Au-patterned SiO_2/Si substrate (henceforth the Au-patterned substrate). The Au-patterned substrate and a 5 × 5 mm sapphire wafer are separately cleaned in trichloroethylene, acetone, then isopropyl alcohol (IPA) in a sonicator for 2 min. each. After using the sapphire wafer to scrape the NW from their growth substrate, the sapphire wafer is dropped in 2.5 ml IPA in continuous sonication to release the NW from the sapphire. After sonicating for 15 min., the NW-IPA suspension is transferred in its entirety, with a 1 ml soft pipette, onto the surface of the Au-patterned substrate. The Au-patterned substrate is heated to 90°C during this process to let the IPA evaporate quickly. This technique is known as "drop-casting."

Once the scraped NW are transferred onto the Au-patterned substrate, the NW are connected to the Au leads with platinum leads deposited in a FIB microscope. After plasma-cleaning the Au-patterned substrate with NW for 10 minutes, the substrate is introduced in a Ga-ion dual FIB-scanning electron microscope equipped with a Trimethyl(methylcylopentadienyl)Platinum(IV) ("Pt precursor") gas injector system (GIS) for Pt deposition. Once a good NW candidate is identified (close to two Au lead ends, $\gtrsim 1$ μm, not touching other NW), Pt contact leads are deposited to connect each end of the NW to one Au leads: the nozzle of the GIS is inserted close to the substrate and the Pt precursor is flowed while the Ga ion beam[1] is scanning over the area intended to be covered by the Pt lead. Fig. B.2(a) shows a scanning electron microscopy (SEM) image of the center portion of the Au spider with four sets of 2 Pt leads connecting four NW to four respective sets of Au leads, while Fig. B.2(b) shows a detail of Fig. B.2(a) showing one set of Pt leads. Here the Pt leads are ~200 nm wide. An additional Pt lead is deposited simply across two Au leads to provide the reference resistivity of the deposited Pt leads.

Once the Pt leads have been deposited, the Au-patterned substrate with the single-NW circuits is transferred to a probe station for I-V measurements. The probe station is equipped with an optical microscope and four probes with three degrees of freedom (forward/backward, side-to-side, and raise/lower movements) and replaceable tungsten needle contacts. As only two leads per NW were prepared, however, the work described here only employs two probes. The probe contacts are be electrically connected via BNC cables to a measurement tool such as a precision voltage and current source and meter. The source and meter tool operation is then automated via a python script that sets the potential difference ΔV across the probes and measures the resulting current I. The Python code[2] used in this work is reported in Sec. B.2.2.

B.2.2 Python code

```
# desc: simple jv scan using Keithley 2420 over GPIB

# output to file and plot simultaneously

### interactive mode breaks running in a shell- run script from python console

import visa
from time import sleep
import matplotlib.pyplot as pt
#from datetime import datetime
import csv

#timestamp = datetime.now().strftime("%Y-%jT%H%M%S")
#filename = timestamp + "_jv2420.csv"
filename = "s52\s52_p78_n34_01"
datafile = open(filename+'.csv', "w")
writer = csv.writer(datafile)

pt.ion()
fig = pt.figure()
ivax = fig.add_subplot(211)
ivax.set_ylim([-1e-6, 1e-6])
ivax.set_autoscalex_on(True)
ivax.set_autoscaley_on(True)
rax = fig.add_subplot(212)
rax.set_autoscalex_on(True)
rax.set_autoscaley_on(True)

ivax.grid(True, which='both')
rax.grid(True, which='both')

ivax.set_ylabel("I (A)", fontsize=16)
rax.set_ylabel(r"$dV/dI$ ($\Omega$)", fontsize=16)
rax.set_xlabel("V (V)", fontsize=16)

fig.suptitle("Keithley 2420 IV, R", fontsize=20)

fig.show()

rm = visa.ResourceManager()

ADDR_2420 = 11

keithley = rm.open_resource('GPIB0::24::INSTR')

max_v = 0.1
min_v = -0.1
N = 100
DELAY = 0.2 # (s) delay between
CURRENT_LIMIT = 0.01*10 # (A)

dv = (max_v - min_v) / N

```

```
# Configuration of 2420/2440 for JV scan

def WriteCommand(command):
 print(command)
 keithley.write(command)

WriteCommand("*RST; :STAT:PRES; *CLS")

sleep(2.0)

WriteCommand(":SOUR:FUNC VOLT")
WriteCommand(":SOUR:VOLT:MODE FIXED")
# vmax = max([abs(max_v), abs(min_v)])
#WriteCommand(":SOUR:VOLT:RANG BEST")

WriteCommand(":SENS:FUNC:CONC OFF")
WriteCommand(":SENS:FUNC \"CURR\"")
WriteCommand(":SENS:CURR:PROT {}".format(CURRENT_LIMIT))
#WriteCommand(":SYST:RSEN ON") #switch to 4 channel mode
WriteCommand(":SYST:RSEN off") #switch to 2 channel mode

WriteCommand(":SOUR:VOLT:LEV {}".format(min_v))
WriteCommand(":OUTP ON")

print("Starting Sweep")

lasti = 0.0
lastv = 0.0
dvdi = 0.0
V=[]
I=[]

for n in range(0, N + 1):
 setpoint = min_v + n * dv

 WriteCommand(":SOUR:VOLT:LEV {}".format(setpoint))

 sleep(DELAY)

 WriteCommand(":READ?")

 read_val = keithley.read().split(",")[1]
 read_val = float(read_val)
 print("{} V, {} A".format(setpoint, read_val))

 writer.writerow([setpoint, read_val])
 V.append(setpoint)
 I.append(read_val)
 if n is 0:
 lastv = setpoint
 lasti = read_val
 else:
 dvdi = (setpoint - lastv)/(read_val - lasti + 1e-9)
 lastv = setpoint
 lasti = read_val
```

```
108   rax.scatter(setpoint, dvdi, color='black')
109
110   ivax.scatter(setpoint, read_val, color='black')
111   tmp = fig.canvas.draw()
112   pt.pause(0.05)
113
114
115 WriteCommand(":OUTP OFF")
116
117 #pt.clf()
118
119 keithley.close()
120
121 datafile.close()
122
123 pt.savefig(filename + '.png', bbox_inches='tight')
124
125 input('Press any key to close figure')
126 pt.close(fig)
127
```

B.3 In-situ dual nano-manipulator single-nanowire *I-V* characteristics measurement

While the technique of drop-casting NW onto a Au-patterned substrate is well suited for repeated electrical transport measurements, it requires destroying (scraping) at least part of the sample, in addition to preventing further microscopy and spectroscopy analysis of the scraped NW. In this section an alternative, non-destructive technique used to perform in-situ *I-V* characteristics measurements of single NW in an SEM equipped with nano-manipulators is described.

The entire NW growth sample is introduced mounted on an SEM sample holder with a drop of silver paint covering a corner of the sample and extending onto the surface of the sample holder to ensure electrical contact between the ITO layer and the ground of the SEM.[3] The mounted sample is loaded into a dual-beam SEM-FIB microscope equipped with two W-needle nano-manipulators. In the case of this work, the dual-beam microscope is equipped with one port-mounted linear nano-manipulator and one sample stage-mounted rotating-arm nano-manipulator (see Fig. B.3 for a schematic of the entire setup).

To ensure ease of contact with the tip of a NW, the tip of the W-needle mounted on the linear nano-manipulator is sharpened via milling with the FIB to a 2-5 μm long, ~500 nm diameter point (see Fig. B.4), while the tip of the W-needle mounted on the rotating-arm nano-manipulator is put into contact with the silver paint on the corner of the sample to provide electrical ground. To realize the measuring section of the electrical circuit, one terminal of the precision voltage and current source and meter is electrically connected to each nano-manipulator via BNC-crocodile clip cables.

To facilitate approaching the linear nano-manipulator needle tip to the chosen NW, both the needle tip and the NW tip are *separately* brought to eucentric height. The position of the linear nano-manipulator needle tip is adjusted until it sits at the center of both the unshifted electron beam and the unshifted focused-ion beam and is recorded. For the NW, after retracting the nano-manipulator, the height of the stage is adjusted until the tip of the NW does not change position with respect to the electron beam. The nano-manipulator is then reintroduced ~100 μm above its recorded eucentric height and then slowly and carefully lowered to touch the tip of the NW. Once the source and meter and NW is completed, the setup is ready for measurement using the same Python code as in Sec. B.2.

B.4 Figures

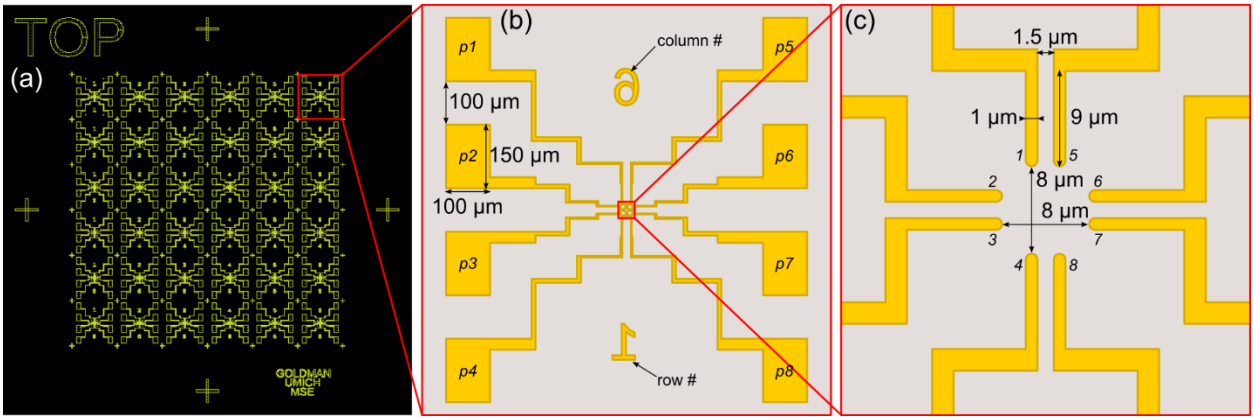

Figure B.1: Schematic representation of the gold-patterned insulating SiO_2 substrates for single-NW circuit manufacturing. **(a)** CAD image of the actual photolithography mask used for the Au deposition on SiO_2. The pattern comprises 6 × 6 = 36 identical "spiders", each containing 4 × 2 = 8 (hence "spider") rectangular pads and relative leads. **(b)** Schematic drawing of one spider, in this case, the row 1, column 6 spider. The column and row numbers are lithographed towards the top and the bottom of the spider, respectively, for quick identification in a microscope. The eight 100 × 150 µm pads (named "p1," "p2," "p3," etc.) are organized in four 100 µm-spaced rows, and two columns on the left and right edges of the spider, while the respective leads progressively thin and converge towards the center of the spider. **(c)** Schematic drawing of the center of a spider, where the eight leads converge in four parallel couples towards the edges of an 8 × 8 μm^2 empty square space, designed to accommodate the NW that will be connected to the Au leads. The final stretch of each Au lead is 9 µm long and 1 µm wide, with each couple of parallel leads separated by 1.5 µm.

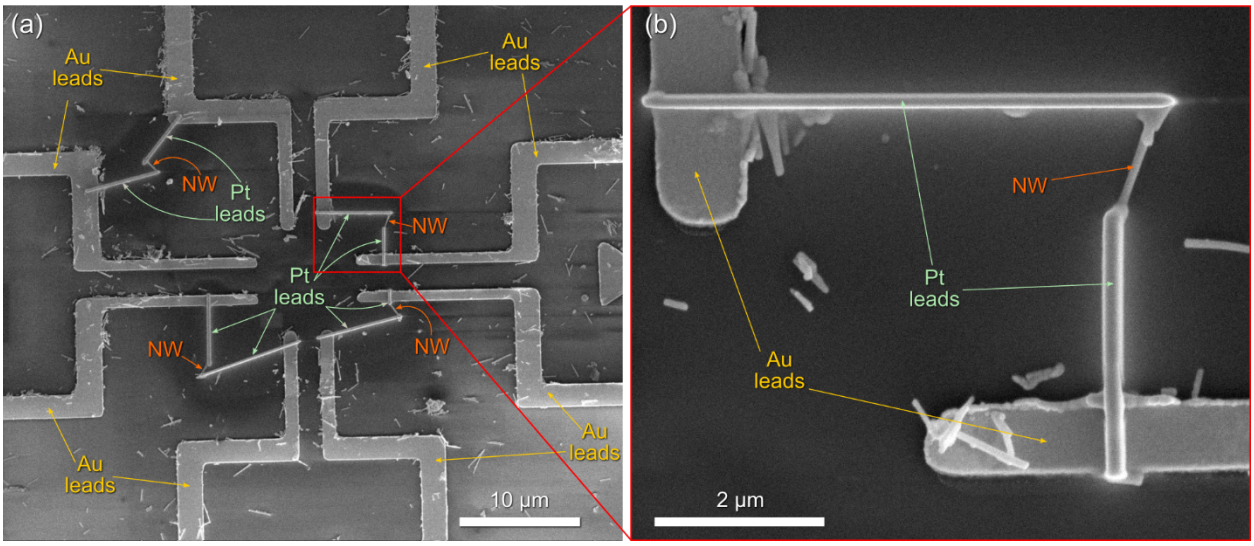

Figure B.2: SEM image of FIB-deposited Pt leads connecting NW photolithography-deposited Au leads. **(a)** SEM image of the center portion of the Au spider with four sets of 2 Pt leads connecting four NW to four respective sets of Au leads. **(b)** Detail of (a) showing one set of Pt leads. Here the Pt leads are ~200 nm wide.

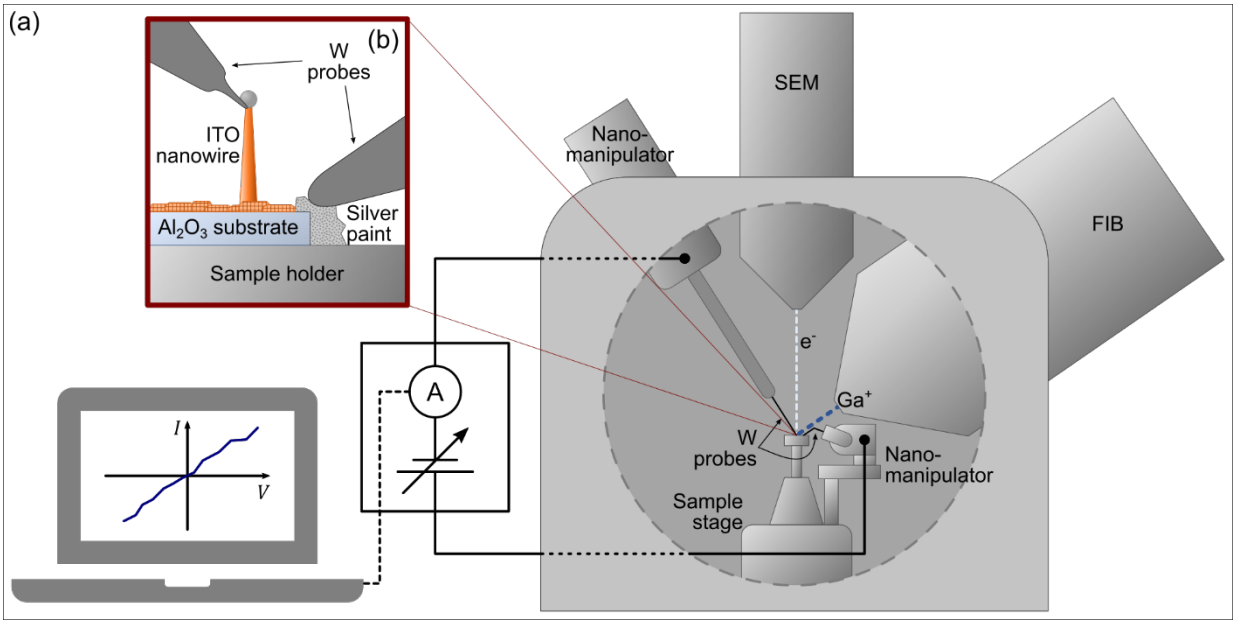

Figure B.3 Schematic drawing of the setup for measuring in-situ single-NW *I*-*V* characteristics in a dual-beam microscope. **(a)** Schematic of the microscope setup with relative measuring circuit: the sample is introduced in a dual-beam SEM and FIB microscope with a port-mounted linear nano-manipulator and a stage-mounted rotating arm nano-manipulator. One terminal of a precision voltage and current source and meter tool is electrically connected to each nano-manipulator, while a laptop control the operation of the source and meter tool and acquires the data. **(b)** Nano-scale detail of the sample, where the surface of the sample is electrically connected to the sample holder with silver paint, one W probe is touching the silver paint (ground), and a sharpened probe is touching the tip of a nanowire.

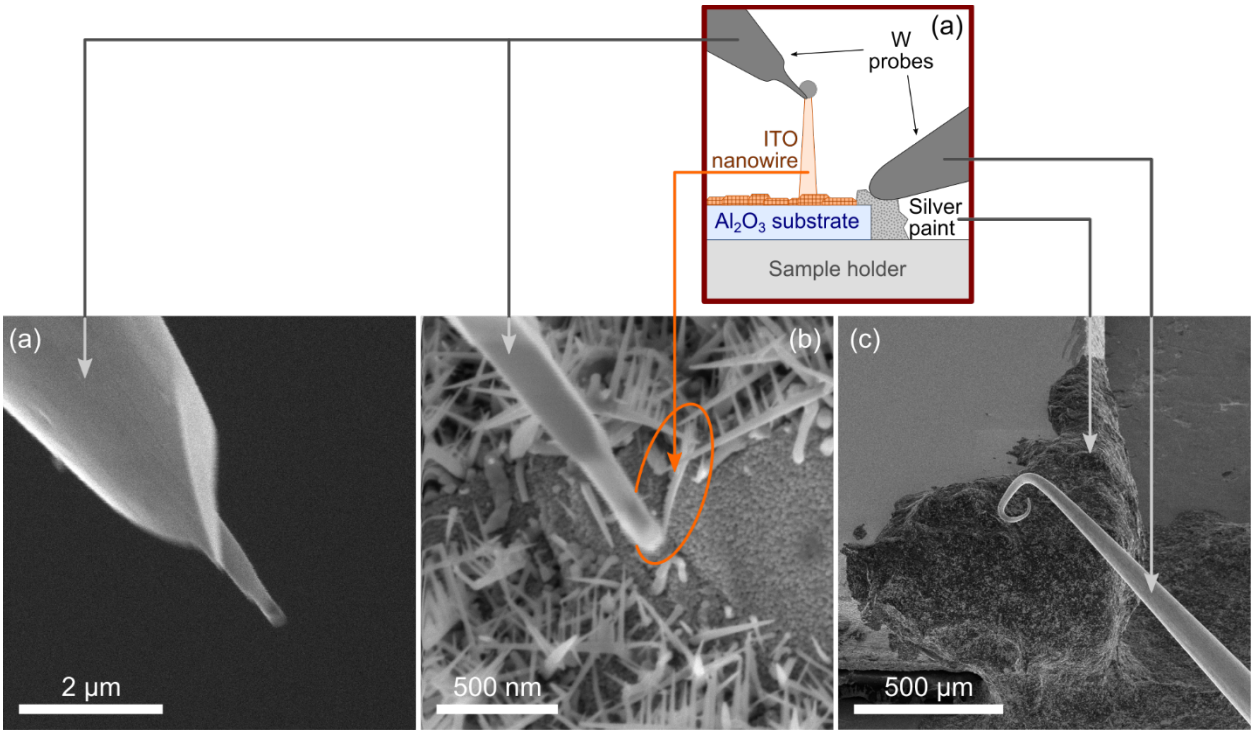

Figure B.4 SEM images of the W nano-probes needle tips after sharpening and approach to the sample.

B.5 References

[1] While Pt deposition with the electron beam does indeed result in a more precise deposition, allowing for thinner leads, we found the resulting leads to yield no detectable conduction, rendering them unsuitable for such work.

[2] This code was originally written by Steve Novakov in Prof. John Heron's group.

[3] The silver paint drop offers easy purchase for the second (ground) nano-manipulator tip, as well as the option of using the electrical ground of the SEM as ground of the measuring circuit, bypassing the need for a second nano-manipulator, albeit with possible increased resistance and risk of bad contacts.

Appendix C Experimental Challenges, Procedures and Observations

In this appendix, the experimental challenges, the procedures followed and the experimental observations made during this dissertation work are described.

Section C.1 focuses on the Veeco GENII molecular beam epitaxy (MBE) tool, with a description of repairing the sample transfer trolley (Sec. C.1.1), designing a mounting bracket for the pyrometer and the pyrometer calibration procedure (Sec. C.1.2), repairing the growth chamber sample manipulator (continuous azimuthal rotation, CAR) (Sec. C.1.3), installing a focused ion beam (FIB) column on the GENII system (Sec. 0), and preparing the Be source material (C.1.4).

Section C.2 focuses on the Riber C21 MBE machine, with a description of the troubleshooting of the failure of the source temperature control modules (Sec. C.2.1), and of diagnosis the failure of the temperature control of the cracking zone (CZ) of the As source (Sec. C.2.2).

Section C.3 focuses on the Neocera pulsed laser deposition (PLD) machine, with a description of the mirror alignment procedure for the laser path (Sec. C.3.1), the laser focusing lens alignment procedure (Sec. C.3.2), the target preparation procedure (Sec. C.3.3), and how it is possible to recognize the formation of nanowires (NW) after ITO deposition simply with the naked eye (Sec. C.3.4).

Section C.4 contains the procedure for solvent-mediated NW transfer from the growth substrate onto a second substrate, also known as “drop-casting.”

C.1 Veeco GENII molecular beam epitaxy

C.1.1 Trolley repair

As described in Sec. 2.2.2.1, the sample blocks are mounted on a trolley, which is used to transport them between the Intro, Buffer and Growth Chambers. The trolleys are able to slide on fixed rails using steel ball-bearing wheels, as shown in Fig. C.1(b). The trolley motion is magnetically guided from outside vacuum via magnetic coupling between the ferromagnetic iron "slugs" on the top of the trolley and the cylindrical magnetized pucks on top of the Intro and Buffer chambers.

During my PhD studies, in May 2014, the magnetic pucks were no longer affectively guiding the trolley. Therefore we replaced them with similar rare-earth magnests from Applied Magnets.[1] Although these new magnets enabled the external guiding of the trolley, the motion was sticky. Therefore we replaced two of the six steel-ball bearing wheels,[2] namely, those in the front left and center positions when looking at the trolley from the block-loading side. The removal of the wheels and hexagonal nuts, shown in Fig. C.1(b), was facilitated by the addition of a few drops of IPA.

C.1.2 Pyrometer mounting and calibration

As discussed in section 2.2.2.2 and shown in Fig. C.2(a), during MBE growth, the blocks are mounted onto the heating receptacle on the continuous azimuthal rotation (CAR) manipulator, where they are radiatively heated from the backside, with temperature monitoring via a thermocouple placed ~1 mm from the block. To quantify the surface temperature, we use an Ircon pyrometer, model 3V-10C02, with spectral sensitivity between 0.91 μm and 0.97 μm, to avoid the transparency window of GaAs,[3] and temperature range between 400 °C and 1000 °C.

In order to mount the pyrometer on the heated window, we designed an aluminum adapter to accommodate the difference in the radii of their respective perforated patterns. The adapter, which consists of three equidistant threaded rods affixed on each face, as shown in Fig. C.7, was fabricated by the University of Michigan Physics Department Machine Shop.

To calibrate the pyrometer, the 3× to 4× reconstruction transition of GaAs in low As over-pressure at 595°C is used.[4] A new GaAs layer is deposited and left at 250°C overnight. The next morning, the substrate temperature is increased until the (2×4) reconstruction (~ 500 °C) and then the (3×1) reconstruction are observed.[4] Immediately after the (3×1) reconstruction is obtained, the substrate temperature is slowly increased until a sharp transition to a 4× reconstruction is observed. At this point, the substrate temperature is kept constant and the emissivity of the pyrometer is adjusted until the pyrometer reads 595°C.

Following this calibration, in subsequent growths the oxide desorption was routinely observed at 580 °C, while the CAR thermocouple readout was in the range of 760 °C – 840 °C.

C.1.3 CAR repair

As discussed in Sec. 2.2.2.2, the samples are transferred from the buffer to the growth chamber via placement onto the substrate manipulator (continuous azimuthal rotation, "CAR") via a linear transfer rod. The substrate is placed on the heating receptacle which consists of a PBN diffuser plate fixed to the heating filaments with retaining tabs, as shown in Fig. C.2. During growth, the samples are typically rotated at 10 rpm. In the summer of 2017, the normally continuous rotation became intermittent, presumably due to broken retainer tabs which were not properly clamping the diffuser plate and the heating filaments, enabling them to impede sample rotation. Thus, a new heat diffuser plate and 3 retaining tabs were spot-welded in proximity of the old

retainer tabs, verifying the stability of the heat diffuser plate during sample rotation [See Fig. C.2(b-c)].[5]

After the repairing of the heating receptacle on the CAR, the CAR was reinstalled on the growth chamber. However, following the bakeout and setup of the hardware for computer rotation, including the ROtating MOtion ("ROMO") housing, shown in Fig. C.3(a), the azimuthal rotation became increasingly sticky. Since the ROMO housing was not removed during the bakeout, the epoxy affixing its internal magnets, shown in Fig. C.3(c), had failed, causing the magnets to stick to the internal shaft shown in Fig. C.3(b) and impede rotation. Therefore, a new ROMO housing was procured from Veeco and installed.[6]

C.1.4 Preparation of Be source material

As described in Sec. 2.2.2.3, the GENII MBE has a side-facing source flange with four upward and four downward facing effusion cells. The upward facing cells house the elements that melt before they sublime, namely Ga, In, Al, and Bi. Due to its high melting temperature, Be sublimes before it melts. Therefore, to prepare for its installation in a downward facing port, the solid Be needs to be melted and fused to the crucible prior to installation.

0.5 g of Be was placed in a new PBN crucible and mounted on an upward facing port on the R32 MBE in the Goldman lab. To ensure complete melting of the Be, the dopant cell was heated to 100 °C above the Be melting temperature, i.e. 1387 °C, followed by slow cooling to room temperature. Subsequently, we removed the cell from the R32 MBE and confirmed that the BE melted and pooled at the bottom of the crucible. Finally, the Be dopant cell was re-installed on the GENII.

C.1.5 MBE-FIB

During my PhD studies, I assisted Dr. Sunyeol Jeon, and later Jim Delaney, in the design and installation of a new channel-detection electron multiplier (CDEM) detector, for ion imaging and ion-induced secondary electron imaging, mounting method to enable in-situ FIB in GENII MBE. It has been suggested that vibrations inherent to MBE can be reduced by ensuring that the sample and CDEM detectors are in mechanical contact so they all vibrate together.

Building upon the design described in the PhD thesis of Dr. Sunyeol Jeon, we modified the mounting "clamp" for the CDEM detector and the mounting flanges for the FIB column. The CDEM detector mounting "clamp" and the CDEM detector are shown in Fig. C.4. The clamp consists of two half-rings, shown in Fig. C.4(a), that are affixed to the FIB column. Three rods with spring-loaded pins for accommodating the Veeco sample holders are attached to the two half-rings, as well as a bracket for mounting the SE detector. Figure C.4(b) shows the affixing of the CDEM detector on the clamp, while Fig. C.4(c) shows a block mounted on the clamp, verifying that the CDEM detector does not touch the block.

To accommodate the block and CDEM detector clamp attached to the FIB column, a custom straight-walled reducer consisting of a 4.5 in flange connected to a 2.37 in inner diameter tube and an 8 in flange connected to a 6 in outer diameter tube, welded together via a circular crown plate, was designed, as shown in Fig. C.5, and the fabrication was commissioned to MDC.

The reducer was connected to the FIB flange, the clamp was installed on the FIB column, together with the SE detector, as shown in Fig. C.6(a), and the FIB, reducer, and clamp were installed onto the vacuum chamber connected to the GENII, as shown in [Fig. C.6(b)].

C.2 Riber C21 molecular beam epitaxy

C.2.1 Failure of Eurotherm Modules

On the Riber C21 MBE machine, the temperature of the source material crucibles is regulated by a series of Eurotherm controllers mounted on the back of the left C21 rack, behind the DC power modules that power the cells heating filaments. A diagram of the Eurotherm modules setup is shown in Fig. C.8. Each Eurotherm input controller[7] has two channels, receiving a signal from two source cell thermocouples, and communicates with its corresponding Eurotherm output controller,[8] which has two channels for setting the appropriate power output on the two DC power modules associated with the two thermocouples.

Although the Eurotherms functioned normally for the first few years of the C21, 5 out of 6 of the Eurotherm output modules failed during the May 2016 – June 2017 time frame. Initially, we purchased a new Eurotherm output module, but when four other output modules failed, we sent one of them to Schneider Electric for fuse replacement. We noticed that the replacement fuse differed from the original fuse, which was an incorrect fuse for the module. Since the use of the incorrect fuses was a manufacturing issue, we requested that all fuses be replaced at no cost (see Fig. C.9).

During the same time period, the ventilation fans on top of the left C21 control rack had been originally installed upside-down, so that they blew ambient air down into the inside of the rack rather than blowing the heated air from the inside of the rack out, as designed. The erroneous installation of these ventilation fans may have exacerbated the fuses failure. The ventilation fans were removed and re-installed right side up.

C.2.2 C21 As source cell diagnosis

As described in Sec. 2.2.2.3, arsenic beams are produced by a valved arsenic cracking cell, which comprises a bulk zone (BZ), a pyrolytic boron nitride needle valve (NV), and a cracking zone (CZ). The BZ is the main As source material container, from which As vapor sublimates. The sublimated As vapor escapes through the NV, whose aperture regulates the As vapor flux. The CZ is a heated nozzle which is responsible for "cracking" the As_4 tetramers into As_2 dimers. The cracking is achieved by tuning the cracker temperature. However, the temperature readout and heating control on the C21 As cell cracking zone are unreliable, with the CZ thermocouple failing to record temperatures exceeding 200 °C. These issues are due to an As leak from the BZ, possibly caused by insufficient sealing of the As BZ, as shown in Fig. C.10. In an attempt to further diagnose the issue and, possibly, devise a plan to repair or replace the thermocouple, in the summer of 2014 the As cell was removed from the C21 and inspected. Unfortunately, the As contamination was so severe that the disassembly of the As cell proved impossible, as shown in Fig. C.11.

Nevertheless, an alternative mode of operation was devised in collaboration with the Riber engineers. The operation of a valved As cell is usually conducted at fixed bulk-zone temperature for evaporation, and cracking-zone temperature for $As_4 \rightarrow As_2$ cracking and/or just to prevent As build-up in the cracker, while the As flux is actually regulated by the needle-valve aperture. Consequently, only two temperatures/power levels are needed to successfully operate the As cell cracking zone. In collaboration with Riber, it was determined that the As cracking zone could be operated in "manual" mode, whereby a fixed output power to the heating filament is set, instead of a PID-regulated temperature setpoint. To achieve As_4 sublimation, we use 36% power, corresponding to 3.2 A current and 12 V. To achieve As_2 sublimation, we use 56% power, corresponding to 5.3 A current and 26 V.

C.3 Neocera pulsed laser deposition

C.3.1 Mirror alignment

While setting up the Neocera PLD system, the optics of the laser path were set up as well. Here is described the procedure for aligning the mirrors in the Neocera PLD system laser path. The laser path consists of seven high damage threshold laser line mirrors and a focusing lens (see Fig. C.1). The mirrors are mounted on kinematic mirror mounts, each featuring two thumbscrew adjusters for adjusting the inclination of the mirrors along the vertical and horizontal axis. The mirror mounts are mounted on optical posts, which are mounted to optical breadboards affixed to the laser table or the Neocera table. The first section of the laser line, mounted on the laser table, contains the "homogenizer" path (see Sec. 2.3.2.3) and is contained in a UV-opaque polycarbonate enclosure with sliding panels. The second section of the laser line, mounted on the Neocera table, contains the focusing lens and the magnet post-mounted removable laser energy meter, and is contained in a UV-opaque PMMA enclosure with sliding panels as well.

The laser is set to emit a single pulse with the push of the push-button at the end of the cord attached to the laser operating panel. UV eye-protection goggles are worn. The physical laser shutter is opened. For each mirror, the two mirror inclination adjusters are adjusted until the laser pulse appears centered on the next mirror (lens) in the laser line. To visualize the laser spot on the next mirror (lens) in the laser line, a 3'' × 5'' paper flash card is placed in front of the next mirror (lens), taking care not to touch or scratch the glass. The procedure is repeated for all seven lenses until the laser beam appears centered through the final focusing lens.

C.3.2 Lens alignment

During the experimental work in this dissertation it has become clear that not only the laser spot fluence (energy per unit surface), but also the laser pulse energy and the laser spot size *separately* have an influence on the resulting plasma plume expansion kinetics, and thus on the growth mode, for VLS NW. The adjustment of the spot size is achieved through adjusting the position of the laser focusing lens.

The laser focusing lens is mounted on a precision mm-scaled rail, which is mounted on a vertical optical breadboard in the Neocera table laser enclosure ("laser lens enclosure"), as shown in Fig. C.13(a). On this precision scaled rail, shown in Fig. C.13(b), the position of the lens along the laser path can be changed, changing the distance between the lens and the in-vacuum source material target, or, equivalently, changing the focus of the laser on the surface of the target. The closer (farther) the focus point of the lens from the surface of the target, the smaller (larger) the resulting laser spot size. Additionally, to adjust the horizontal position of the laser spot on the surface of the target, the lens can be rotated around its vertical axis a few degrees.

Figure C.14 shows the effect of the lens position, and consequently of the laser spot size, on the resulting ITO growth mode. Leaving all the other growth parameters the same, i.e. N_2 gas pressure, substrate temperature, laser pulse frequency, and laser fluence, for the lens positioned at ~ 9 cm on the scaled rail ("target out of focus"), the result is VLS NW, while for the lens positioned at ~ 14 cm on the scaled rail ("target in focus"), the result is a VS film.

Through this experiment, it was determined that the optimal lens position to obtain VLS of NW with the ITO target is ~ 9 cm on the scaled rail, corresponding to ~ 0.05 cm^2 laser spot size on the target surface.

C.3.3 Target preparation

Before introducing the source material targets into the main chamber of the Neocera PLD system, the face of the target that is to be impinged upon by the laser must be polished to ensure a flat surface for optimal laser ablation. For the sintered powder ceramic targets used in this dissertation, the polishing procedure consisted of manually grinding the targets, face down, on grinding paper discs placed face up on a piece of lint-free paper in the fume hood. For each target, the grinding paper used was, in order, 300 grit, then 600 grit, then 1200 grit. For each grinding pass on each grinding paper disc, the target face is kept in full contact with the grinding paper and moved in a ~ 3'' diameter circular movement, taking care of inverting the rotation direction (clockwise vs. counter-clockwise) every ~ 10 rotations, to ensure uniformity of the grid.

The first grinding paper used has a relatively rough grit size of 300, to quickly remove the pits left from the previous laser ablation. The grinding on the 300 grit paper is continued until no pitting is visible. The next grit size used is 600 grit, this time to remove the $\lesssim$ 1 mm natural scratches usually left by the 300 grit paper. The grinding on the 600 grit paper is continued until no scratches are visible. This stage should leave the target with a dull surface that appears flat and smooth to the naked eye. The final grit size used is 1200 grit, to achieve the low surface roughness needed for optimal laser ablation. The grinding on the 1200 grit paper is continued until, ideally, the target achieves a smooth, mirror-like finish. Note that unfortunately not all ceramic targets will achieve a mirror-like finish. For example, while a mirror-like finish is possible with ITO targets, SnO_2 targets will retain an opaque, chalk-like appearance. In this case, polishing is continued until absolutely no scratches or pits or imperfections appear on the surface of the targets, leaving the target to look to the naked eye like a perfectly smooth surface.

C.3.4 Naked-eye ITO samples observations

In the course of this dissertation work, it became apparent that it is possible to recognize whether the formation of NW, vs the formation of a film, was achieved, simply by looking at the substrates after growth. This diagnostic is possible the NW obtained in this work were 500 ~ 1500 nm long, which is the same, or close, to the range of wavelength of the visible light. Additionally, the NW were closely spaced, often with < 100 nm between the stems. Thus, these NW arrays are very strong scatterers of visible light.

As a result of the NW arrays being strong scatterers of visible light, the sapphire substrates bearing NW arrays after growth will appear to have a dull, opaque, grey-black film covering them. On the other hand, sapphire substrates bearing ITO polycrystalline films will appear to have a mirror-like, transparent, orange film covering them. Figure C.15 shows photographs comparing the two cases, with Fig. C.15(a) showing the grey NW film, and Fig. C.15(b) showing the orange polycrystalline film.

The dull and grey vs. mirror-like and transparent for NW vs. films is a very apparent contrast and, in addition to being a quick diagnostic requiring no tools other than the human eye, is also applicable to any material system and growth process that yields NW of the same size.

C.4 Solvent-mediated NW transfer ("drop-casting")

This section describes the procedure for solvent-mediated NW transfer, also known as "drop-casting" of NW. The receiving substrate and a 5 × 5 mm sapphire wafer are separately cleaned in trichloroethylene, acetone, then isopropyl alcohol (IPA) in a sonicator for 2 min. each. After using the sapphire wafer to scrape the NW from their growth substrate, the sapphire wafer is dropped in 2.5 ml IPA in continuous sonication to release the NW from the sapphire. After

sonicating for 15 min., the NW-IPA suspension is transferred in its entirety, with a 1 ml soft pipette, onto the surface of the receiving. The receiving substrate is heated to 90°C during this process to let the IPA evaporate quickly. After this procedure, the receiving substrate may also be plasma-cleaned for 5 min before each microscopy session.

C.5 Figures

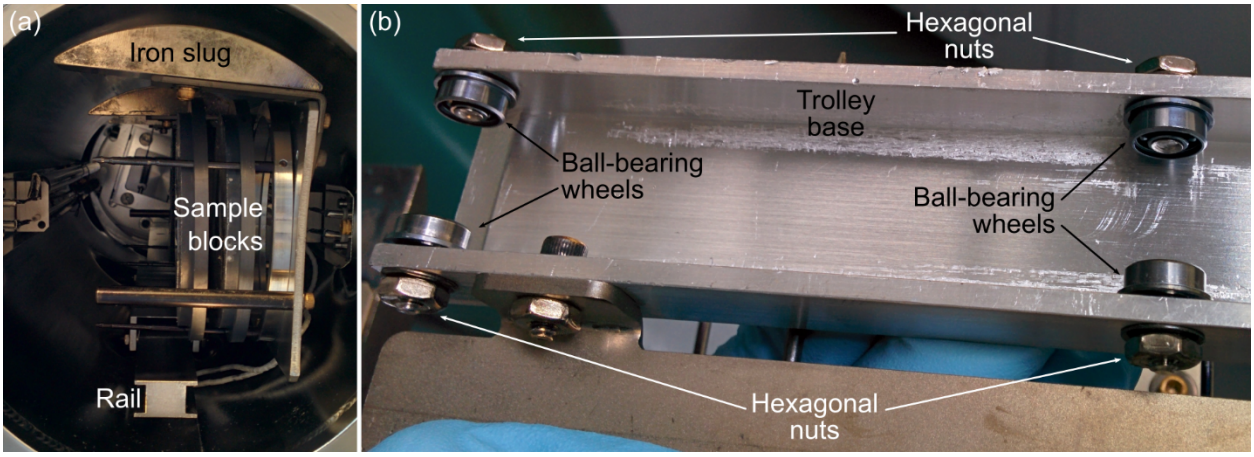

Figure C.1: Photographs of the GENII trolley and its wheel assemblies. **(a)** Side-view of the trolley, highlighting the top magnetic slugs, the sample blocks, and the rail upon which the trolley slides. **(b)** Bottom view of the trolley, highlighting the wheel assemblies and the hexagonal nuts affixing them to the trolley base. There are in total 6 wheels on the trolley.

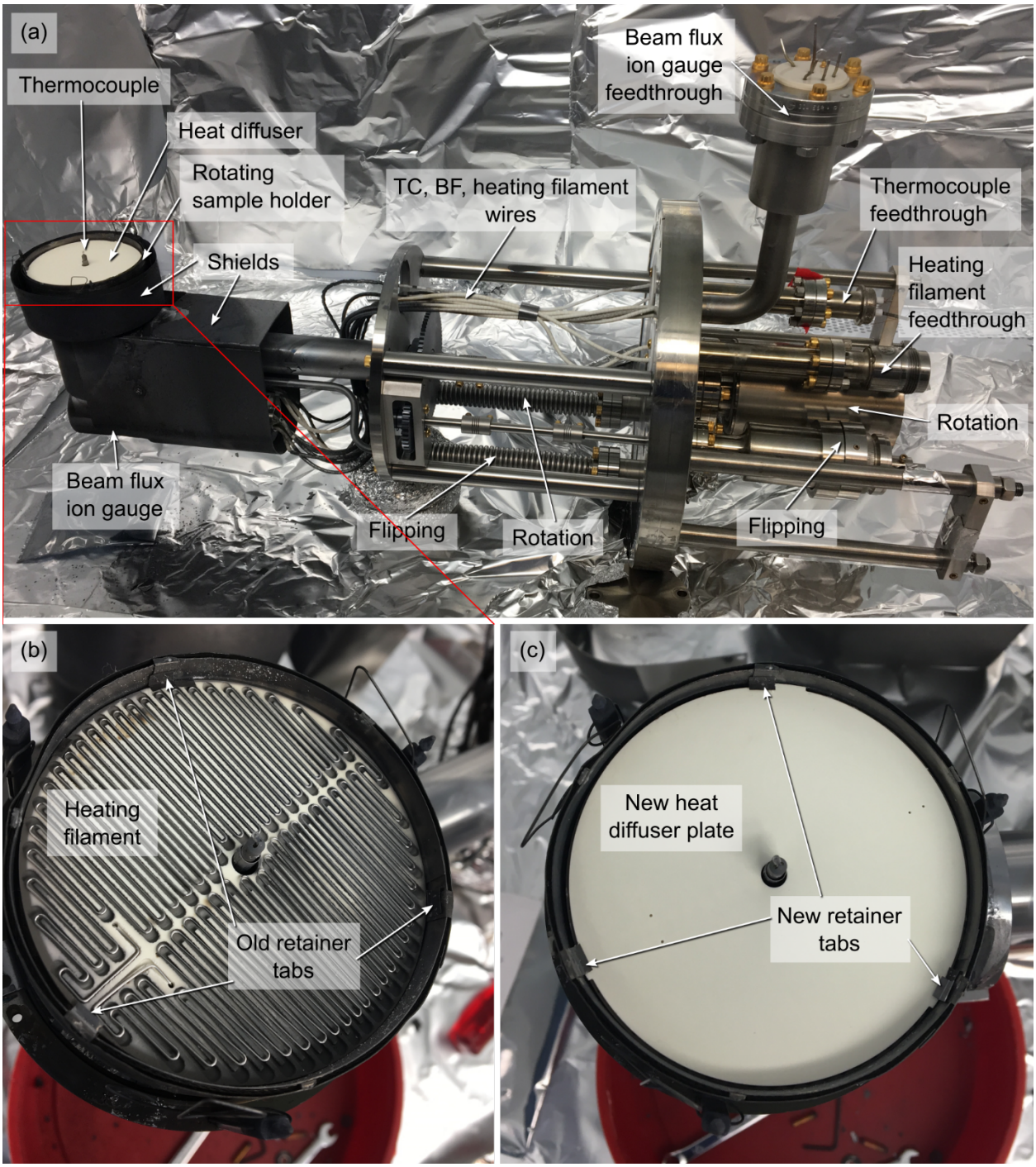

Figure C.2: Photograph of the GENII substrate manipulator, termed continuous azimuthal rotation (CAR), with most components labeled. Close-up views of the substrate heater assembly **(b)** without the heat diffuser plate, showing broken retainer tabs, and **(c)** with new heat diffuser plate and retainer tabs.

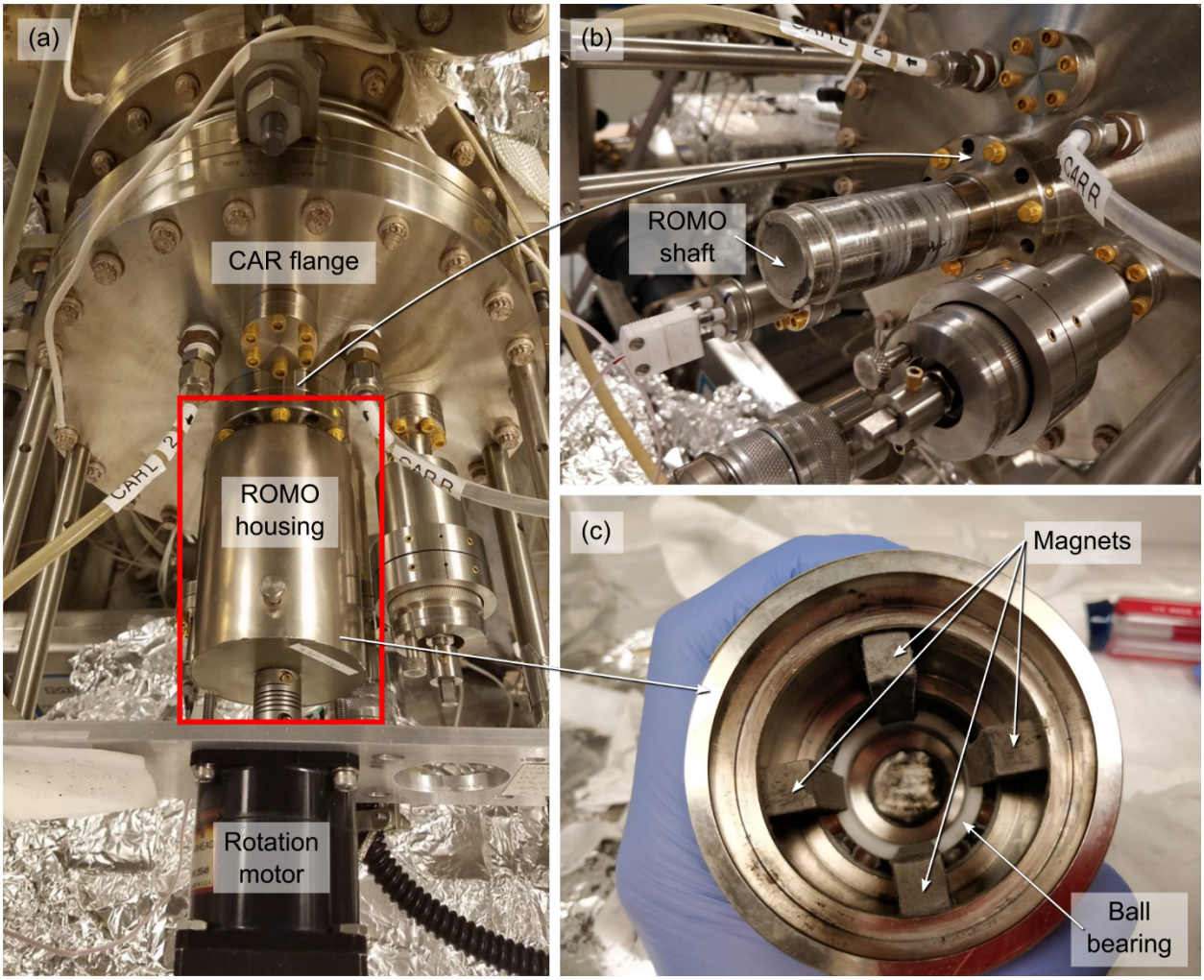

Figure C.3: Photographs of the GENII ROMO housing. **(a)** ROMO housing mounted on its shaft on the CAR flange, with the rotation motor attached. **(b)** ROMO shaft on the CAR flange, after removing the ROMO housing. **(c)** inside of the ROMO housing, showing the magnets and one of the two ball bearings.

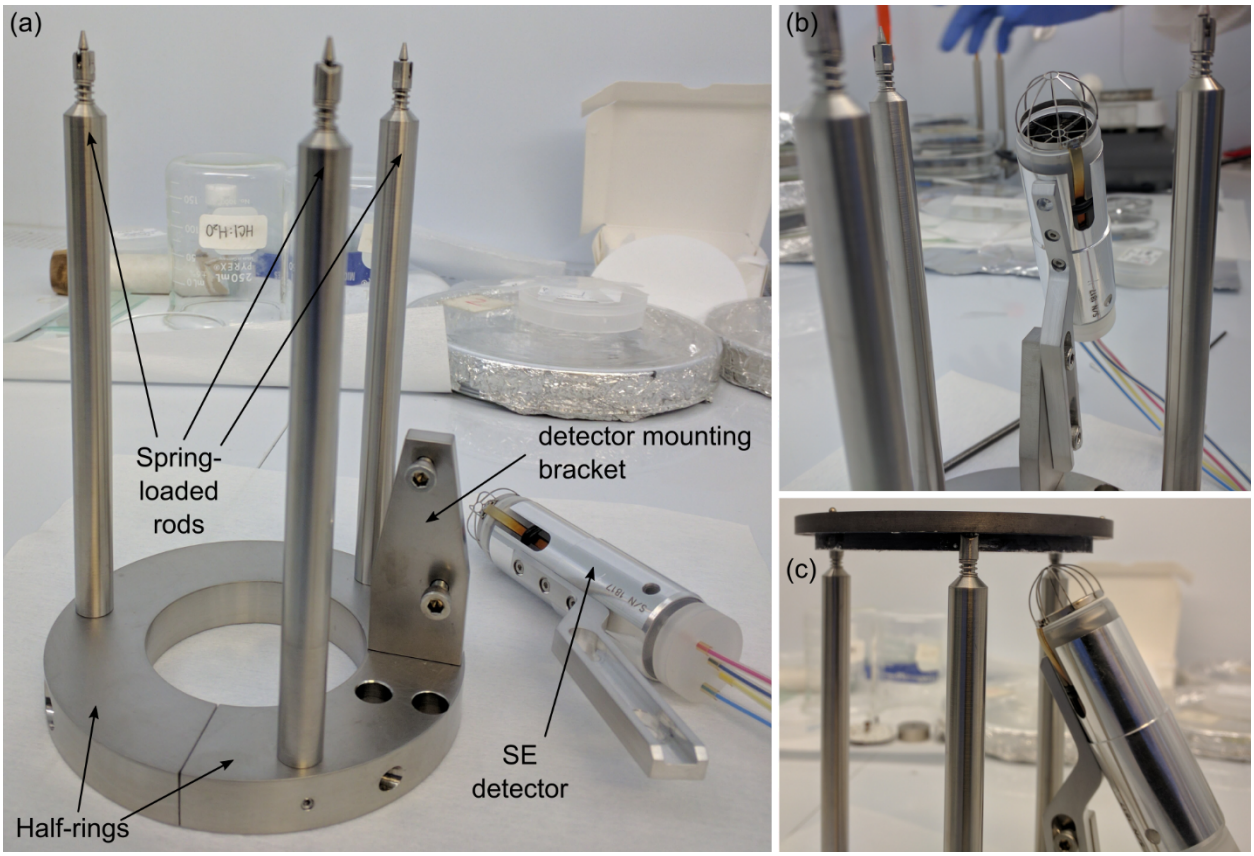

Figure C.4: Photographs of the clamp designed for mounting the substrate holder and the channel detection electron multiplier (CDEM) detector to the focused-ion beam column. **(a)** Photograph of the clamp before installing the CDEM detector. **(b)** Photograph of the clamp after installing the CDEM detector. **(c)** Photograph demonstrating the mounting of the sample holder.

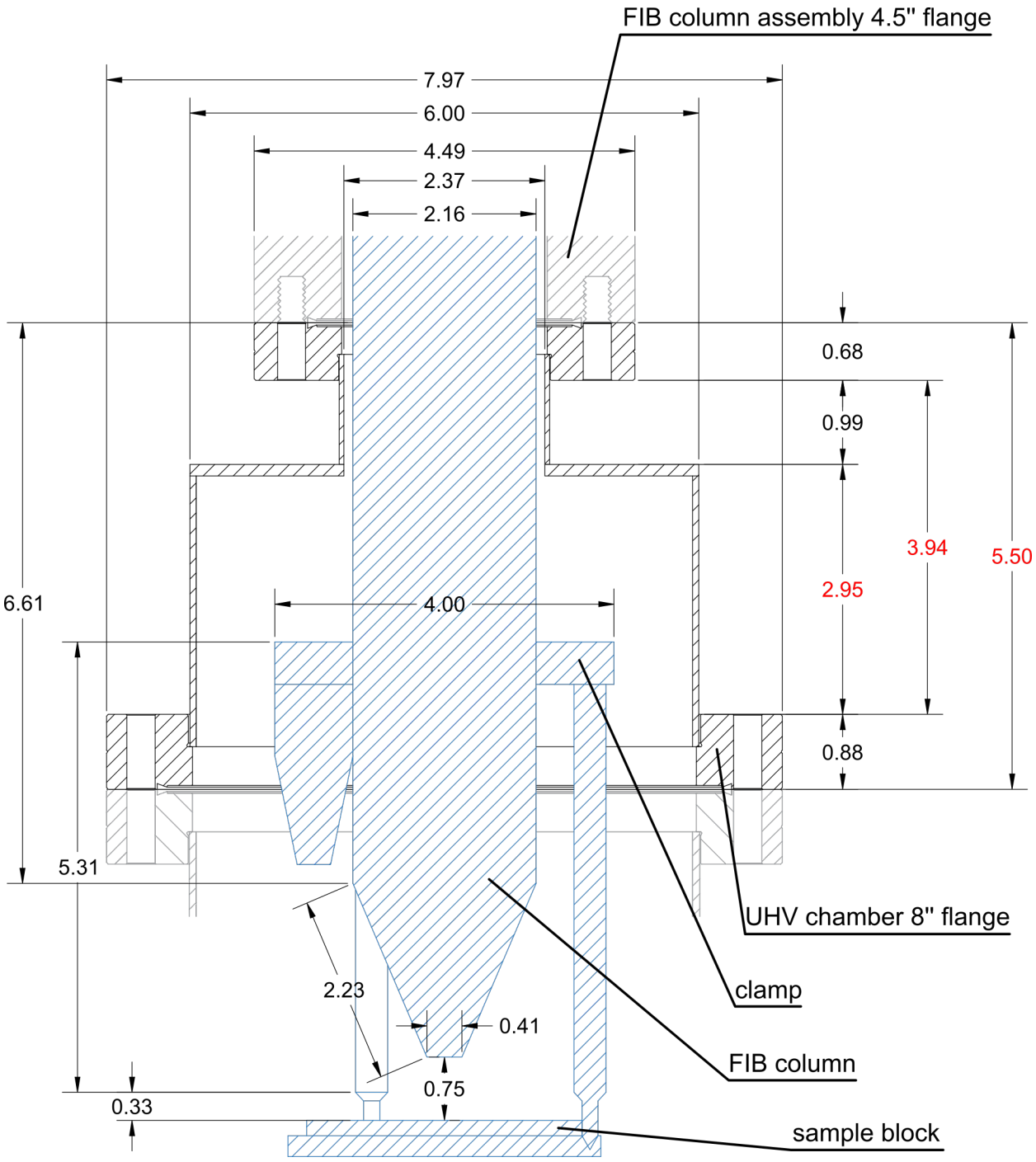

Figure C.5: Machine diagram of the custom straight-walled nipple for mounting the focused-ion beam column to the vacuum chamber. All dimensions in inches.

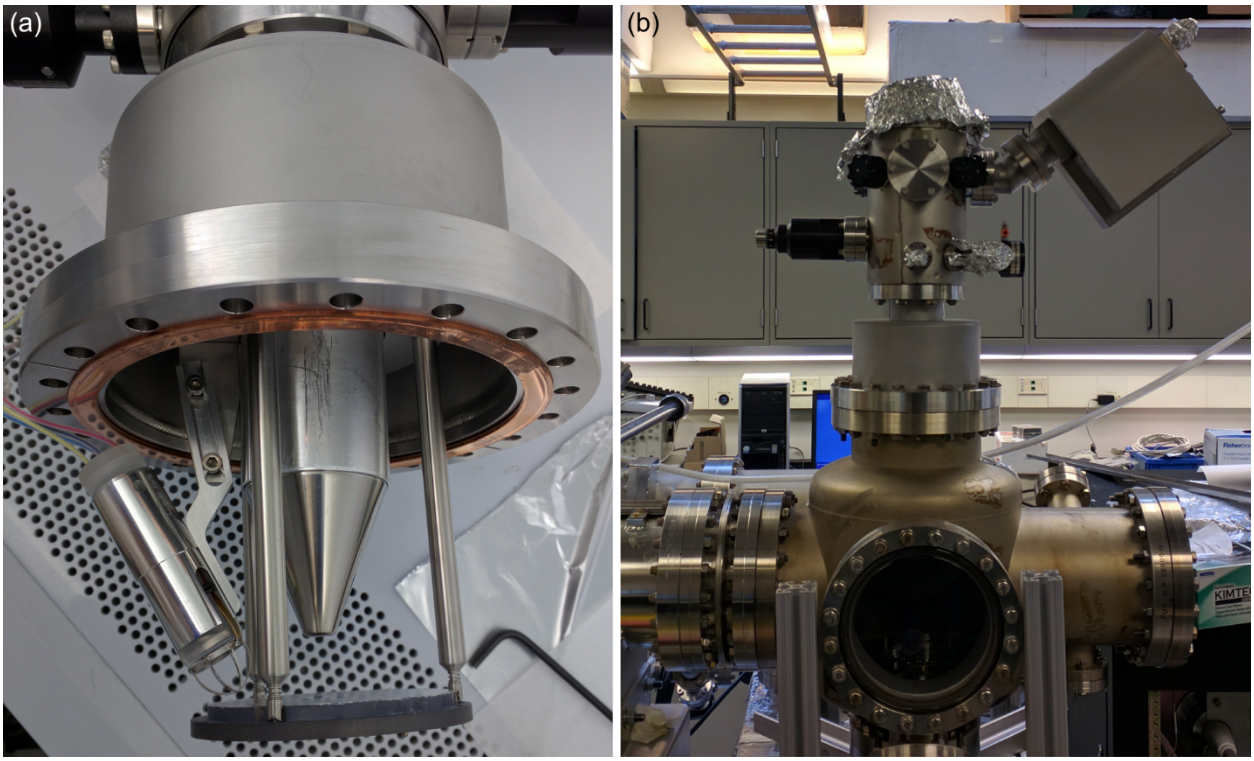

Figure C.6: Photographs of the installation of the focused-ion beam (FIB) column on the GENII vacuum system. **(a)** Photograph of the straight-walled reducer installed on the FIB column, together with the detector and sample holder clamp. **(b)** Photograph of the FIB column installed on the vacuum chamber with the straight-walled reducer.

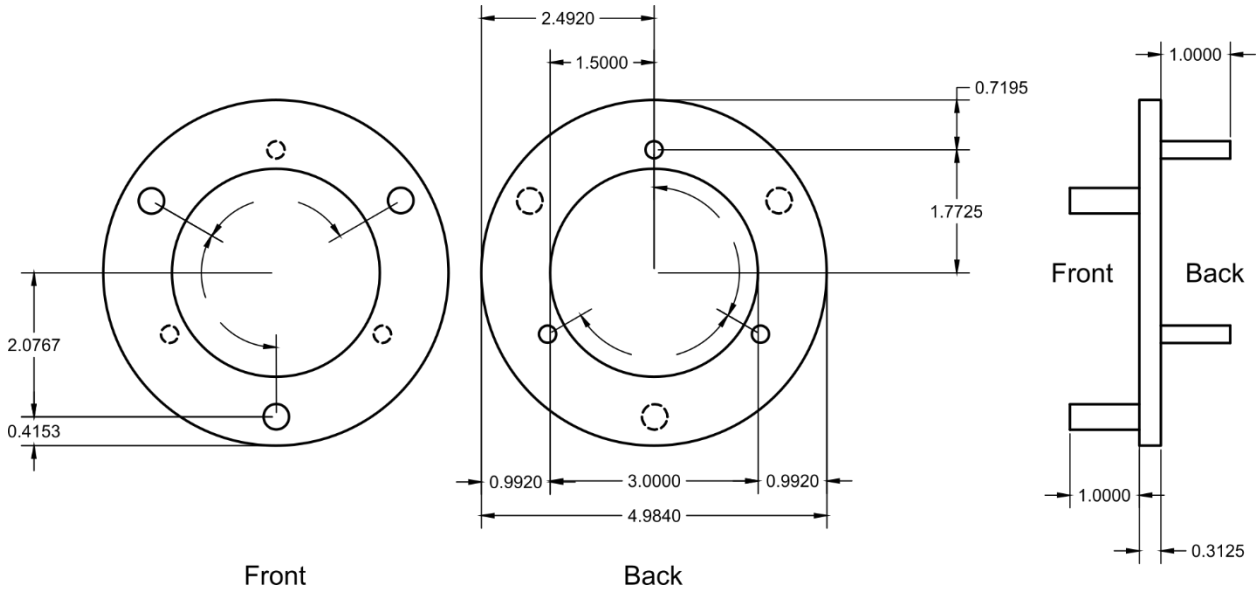

Figure C.7: Machine drawing of the GENII heated window – pyrometer mounting adapter. All dimensions in inches.

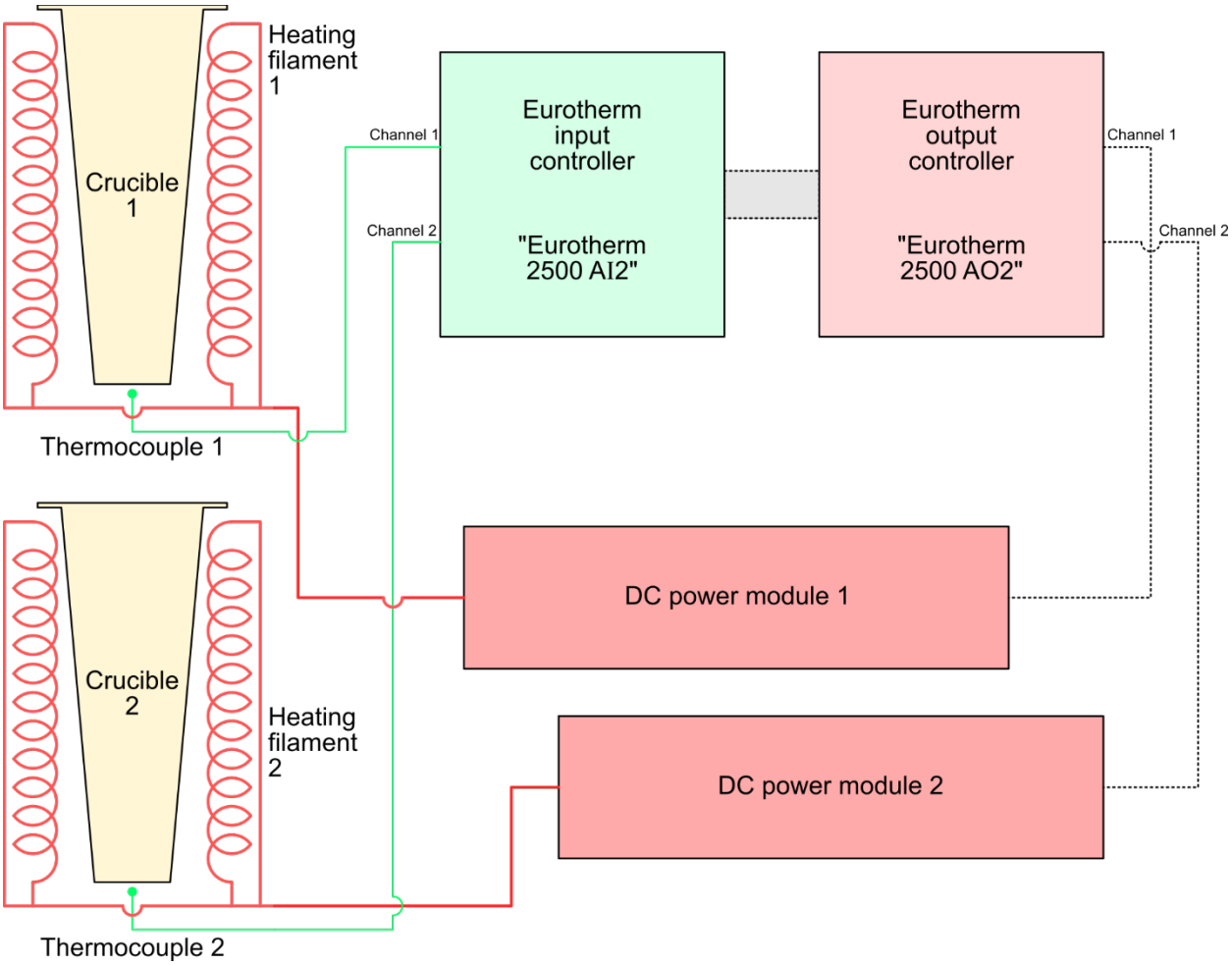

Figure C.8: Diagram of the C21 MBE Eurotherm modules setup.

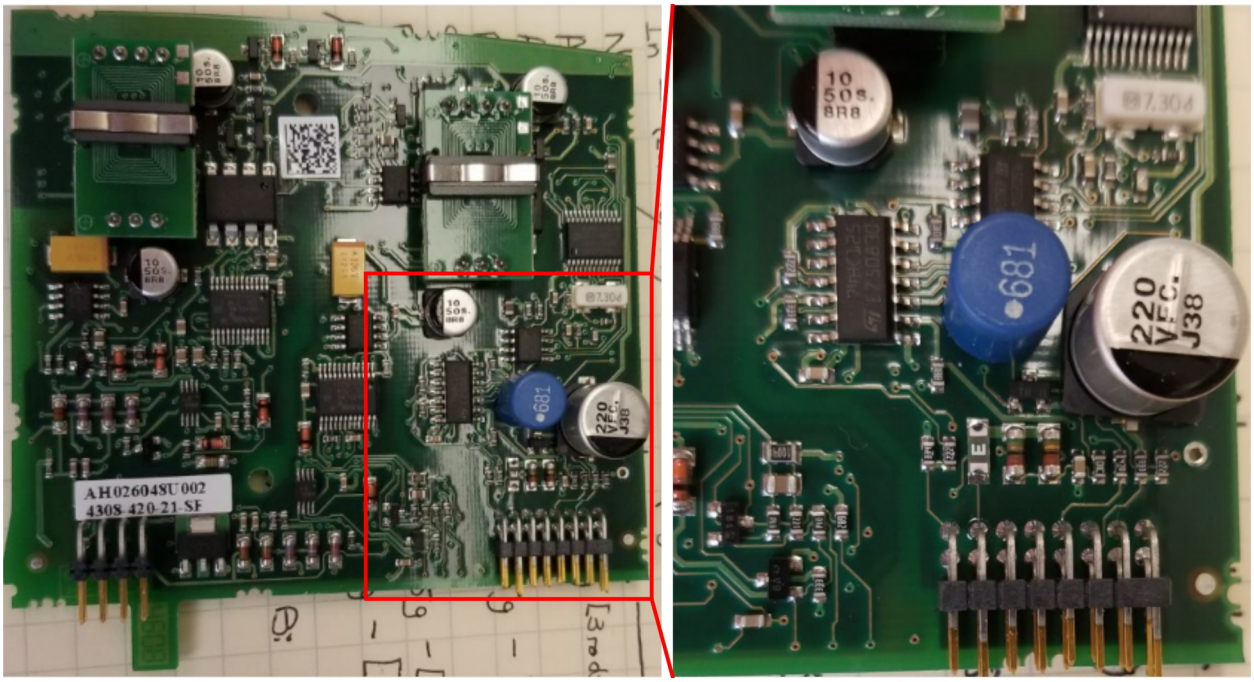

Figure C.9: Photograph of the C21 output power controller module internal circuit board, with detail of the faulty fuse.

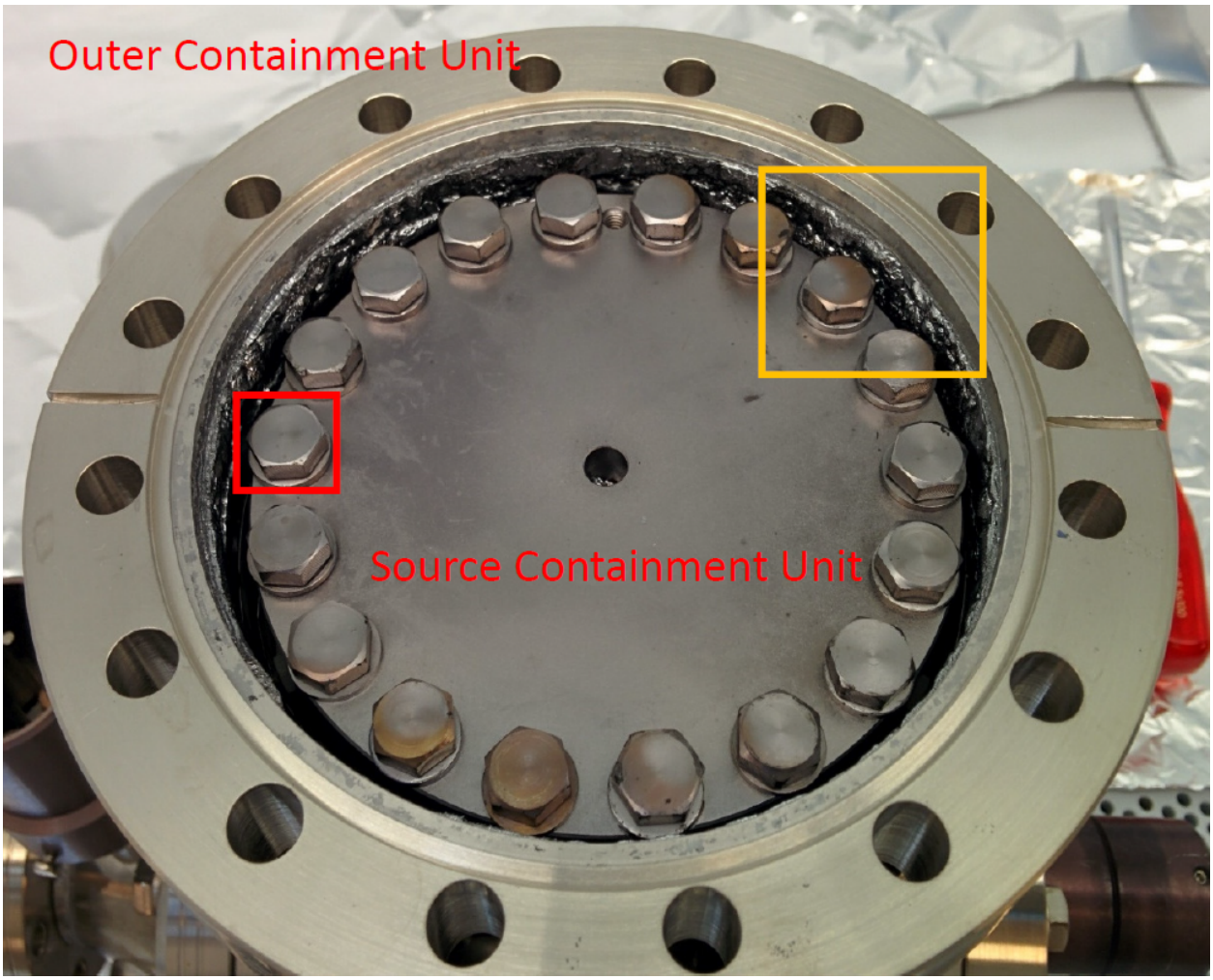

Figure C.10: Photograph of the Riber C21 As reservoir (bulk zone). The screws highlighted by the smaller red rectangle hold the cover of the As containment within the bulk zone. The larger yellow rectangle highlights the excess As deposition in the inner wall of the bulk zone caused by the As leak. From Dr. Timothy Jen's PhD thesis.

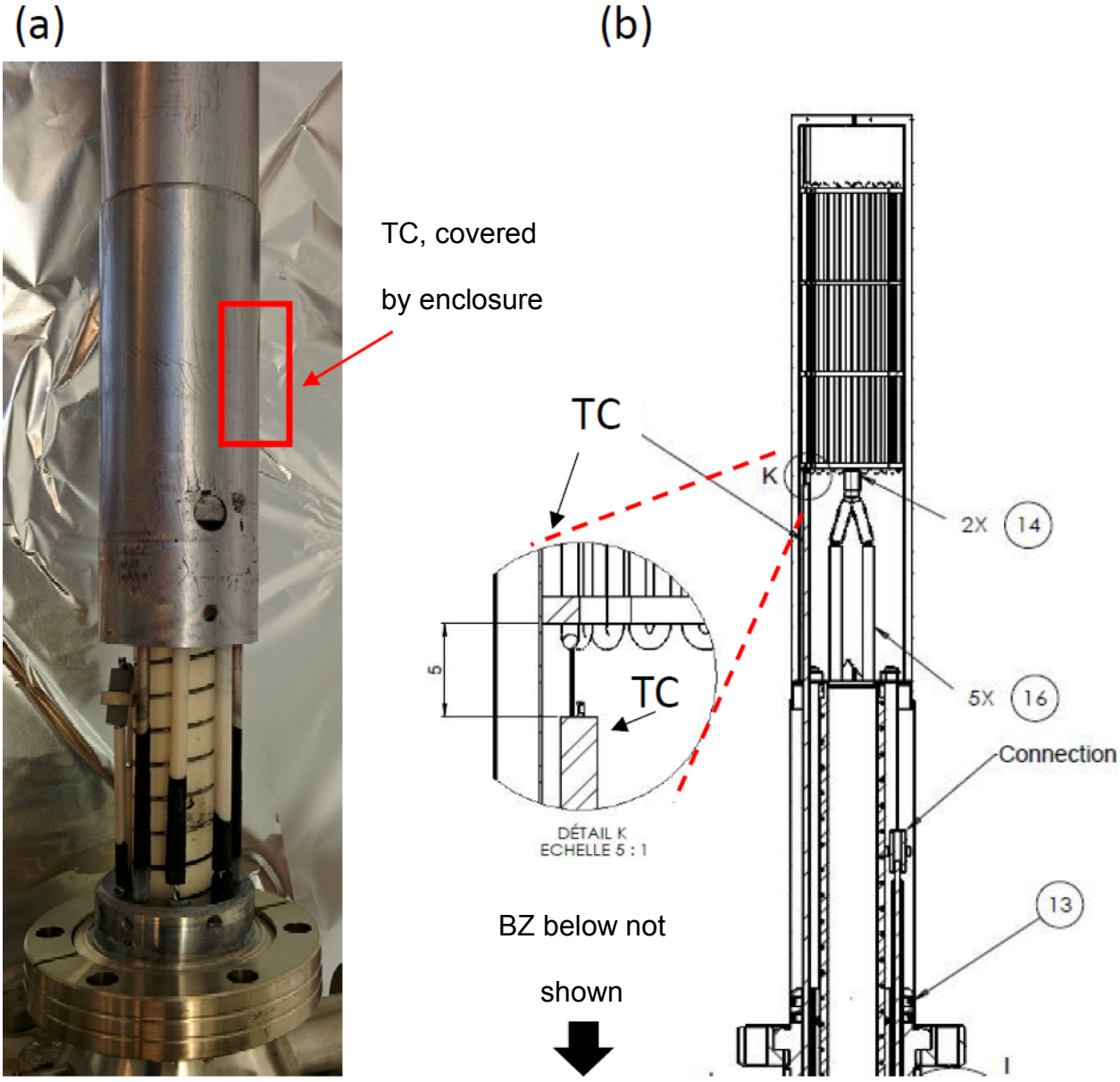

Figure C.11: Photograph and schematic of the Riber C21 As cell cracking zone. **(a)** photograph of the cracking zone (CZ) module: the thermocouple used to record the CZ temperature is inside the enclosure. Removing this enclosure was unsuccessful, possibly due to excess arsenic coating. Note also the blackening of the pyrolytic boron nitride elements, likely caused by the As leak. **(b)** schematic of the CZ, showing the position of the thermocouple inside the enclosure. Adapted from Dr. Timothy Jen's PhD thesis.

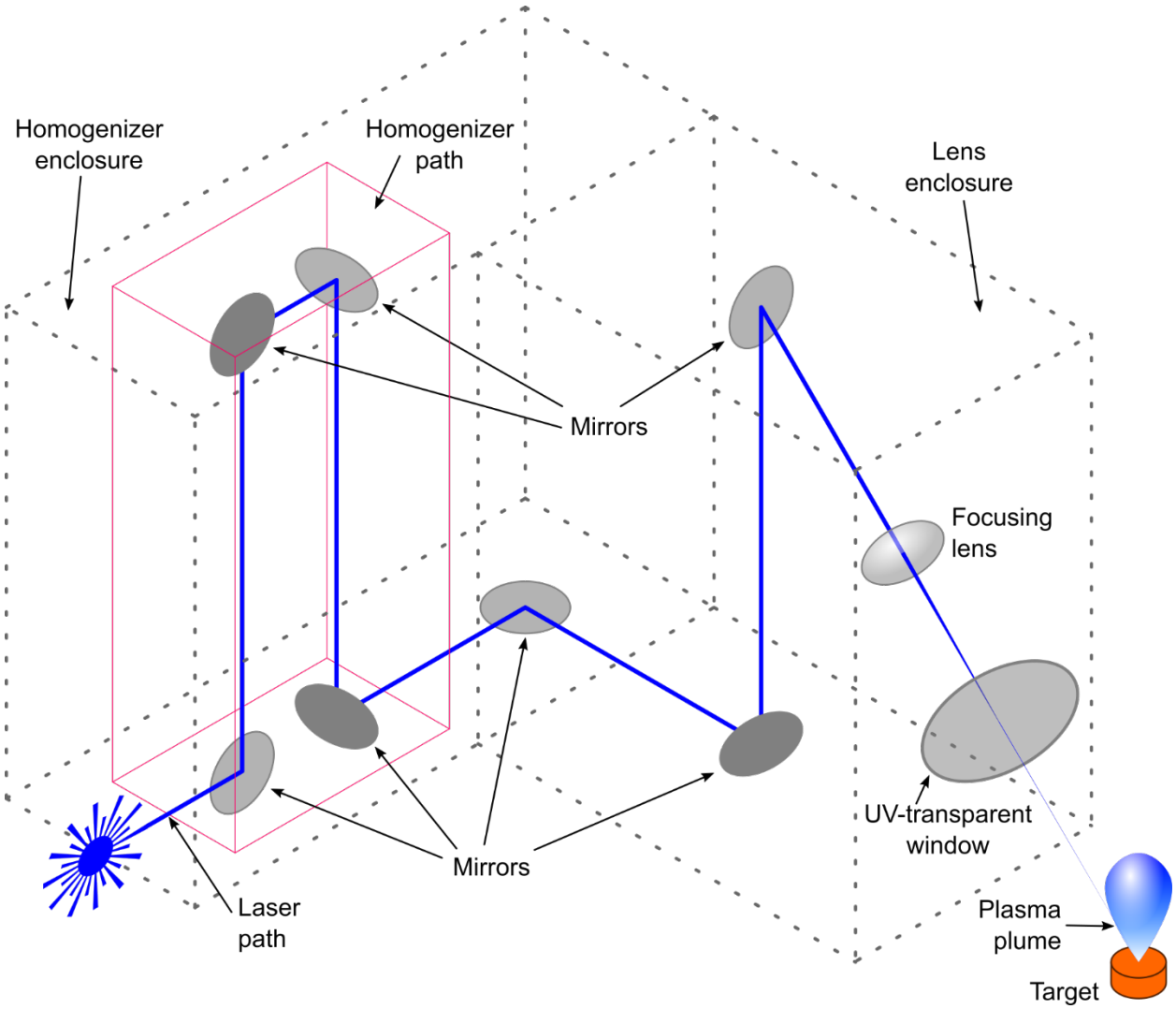

Figure C.12: Schematic diagram of the laser path for the Neocera PLD system.

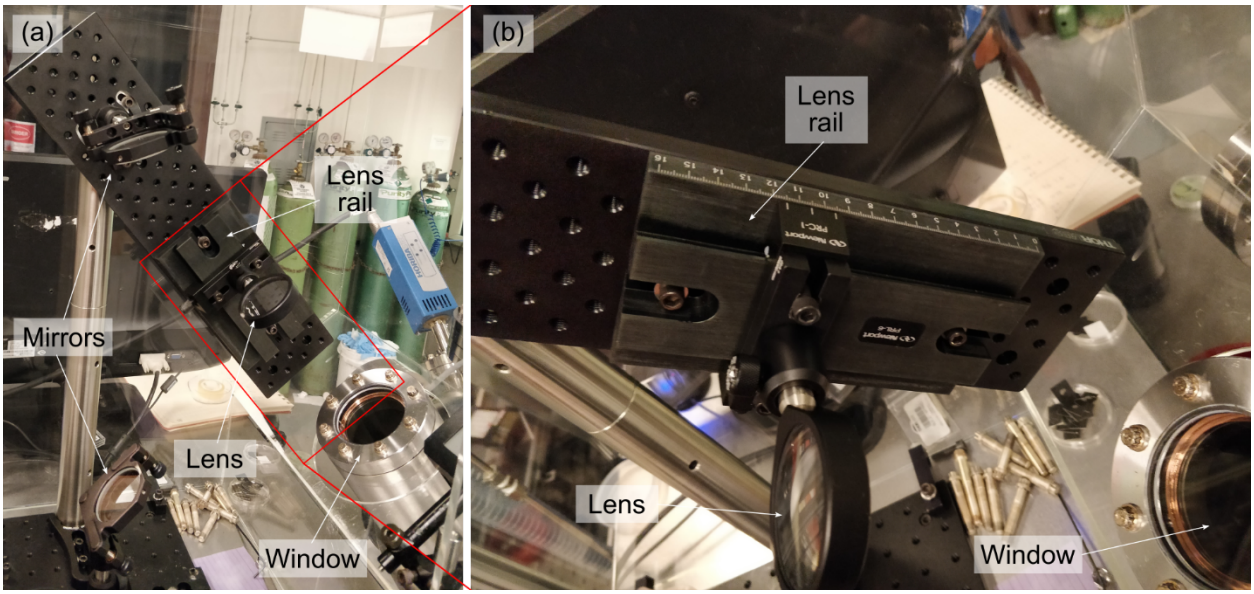

Figure C.13: photographs of the Neocera PLD lens setup. (a) Photograph of the lens setup, showing the mirrors, the lens, the lens rail, and the UV-transparent window on the Neocera main chamber. (b) Detail of (a) showing the mm-scale on the lens rail. The lens rail has an extension from 0 mm (closest to window) to 16 mm (farthest from window).

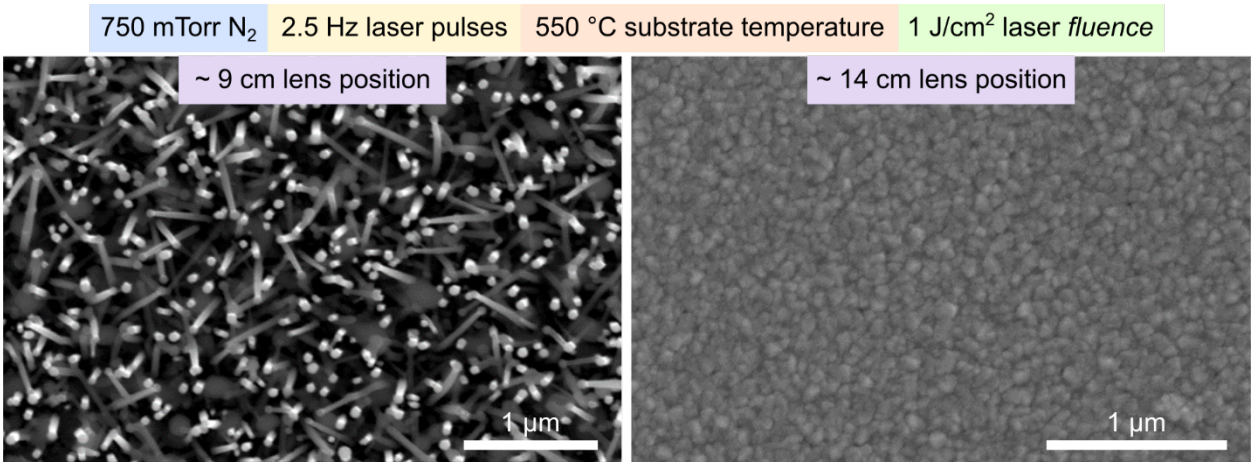

Figure C.14: Scanning-electron microscopy images of ITO layers demonstrating the effect of lens position, and consequently laser spot size, on the growth mode of ITO.

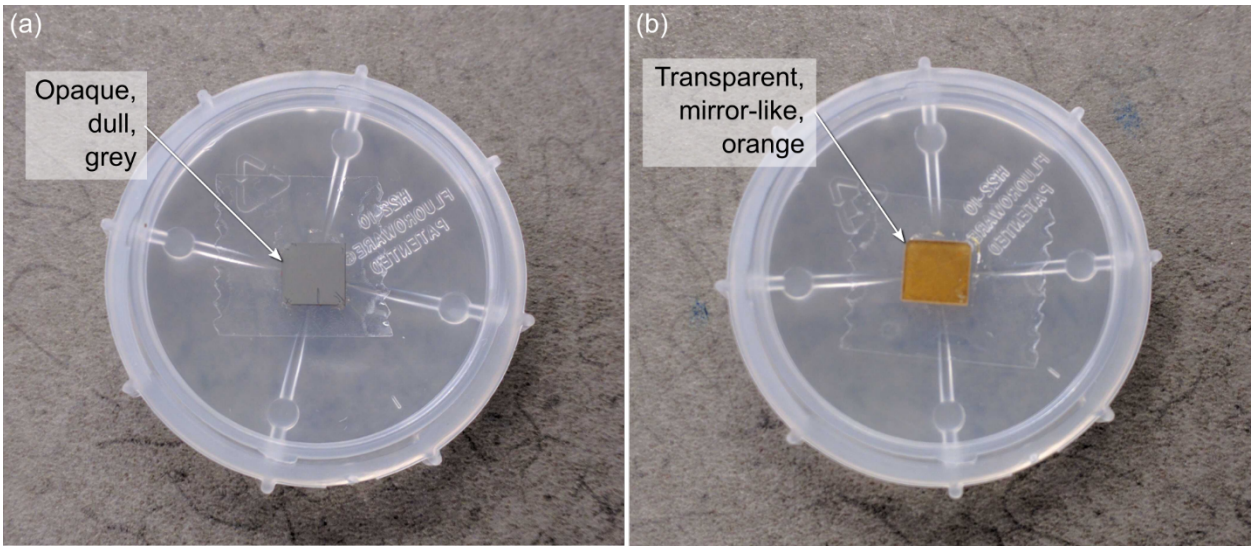

Figure C.15: Photographs demonstrating the surface finish effect of the presence of ITO NW vs. a polycrystalline ITO film on the substrate after growth. **(a)** For NW, the surface of the as-grown sample is dull, opaque, and grey. **(b)** For a polycrystalline film, the surface is mirror-like, transparent, and orange.

C.6 References

[1] Applied Magnets, "Rare Earth Magnets 1.5 in x 1/4 in Neodymium Disc" (p.n. ND066), "Rare Earth Magnets 1.5 in x 3/8 in N42 Neodymium Disc" (p.n. ND067-1).

[2] Veeco, "Wheel assembly" (p.n. 300340), each composed of a "bearing (wheel) axle" (p.n. 0067286600) and a "bearing (wheel)" (p.n. 0067323200)

[3] R.A. Kubiak, S.M. Newstead, and P. Sullivan, "The Technology and Design of Molecular Beam Epitaxy Systems", in *Molecular Beam Epitaxy: Applications to Key Materials*, edited by R.F.C. Farrow, (Noyes, Park Ridge, New Jersey, 1995), pp. 72–74.

[4] I. Kamiya, D.E. Aspnes, L.T. Florez, and J.P. Harbison, "Reflectance-difference spectroscopy of (001) GaAs surfaces in ultrahigh vacuum" Phys. Rev. B **46**, 15894 (1992).

[5] Veeco, "Disk, 3" substrate heater, cover, PBN" (p.n. 207259), "Assy, bracket, small" (p.n. 0067277500).

[6] Veeco, "Assembly, magnet housing" (p.n. 208206).

[7] Eurotherm 2500 AI2.

[8] Eurotherm 2500 AO2.

Appendix D Tabulated Data

D.1 (InAs /) AlGaAs MBE samples

D.1.1 Growth substrate temperatures

Sample n.	Sample manipulator block	Oxide desorption		GaAs buffer		AlGaAs layer		Annealing		InAs layer	
		T_m*	T_s†	T_m	T_s	T_m	T_s	T_m	T_s	T_m	T_s
		°C	°C	°C	°C	°C	°C	°C	°C	°C	°C
CMBE 73	C1	560	580	560	580	600	620	600	620		
CMBE 74	C2	545	580	545	580	545	580	545	580		
CMBE 75	C3	495	580	495	580	460	545	460	545		
CMBE 80	C2	535	580	535	580	535	580	535	580	500	545
CMBE 81	C3	495	580	495	580	495	580	495	580	460	545
CMBE 87	C3	480	580	480	580	480	580	480	580	445	545
CMBE 88	C1	560	580	560	580	560	580	560	580	525	545
CMBE 90	C2	515	580	515	580	515	580	515	580	480	545
CMBE 91	C1	580	580	580	580	580	580	580	580	500	500
CMBE 98	C2	525	580	525	580	525	580	525	580		
CMBE 99	C3	460	580	460	580	460	580	460	580		
CMBE 101	C2	540	580	540	580	540	580	540	580		
CMBE 102	C1	575	580	575	580	575	580	575	580		
RMBE 1154	G20	775	600	755	580	755	580	675	500		
RMBE 1155	G23	830	600	810	580	810	580	730	500		
RMBE 1156	G3	820	600	800	580	800	580	720	500		
RMBE 1172	G3	840	600	820	580	820	580	740	500		
RMBE 1173	G2	820	600	800	580	800	580	720	500		
RMBE 1174	G23	805	600	785	580	785	580	705	500		
RMBE 1175	G20	800	600	780	580	780	580	700	500		
RMBE 1181	G2	800	600	760	560	760	560	700	500		
RMBE 1182	G3	830	600	770	540	770	540	700	500		
RMBE 1198	G3	765	580	765	580	765	580	765	580		
RMBE 1199	G20	790	580	770	570	770	570	770	570		
RMBE 1200	G23	800	580	755	560	755	560	755	560		

Table D.I. Substrate temperatures during the MBE deposition of the InAs/AlGaAs and AlGaAs samples.

* T_m: substrate manipulator thermocouple temperature.
† T_s: substrate temperature.

D.1.2 Mounds statistics

Sample n.	Mound height nm	Mound width nm	Mound length nm	Lateral slope (from fit) deg	Projected area (rectangle) 10^3 nm^2	Volume (isosceles trapezoid prism) 10^3 nm^3
CMBE 73	2.1	736	1485	0.4	1093	1125
CMBE 74	5.1	172	302	4.8	52	131
CMBE 75	1.7	54	96	4.0	5	4
CMBE 80	3.5	145	489	5.2	71	148
CMBE 81	2.1	108	318	3.3	34	36
CMBE 87	1.1	86	124	3.1	11	6
CMBE 88	1.4	108	139	2.5	15	12
CMBE 90						
CMBE 91						
CMBE 97						
CMBE 98	1.6	88	129	2.9	11	9
CMBE 99	0.7	70	104	1.7	7	3
CMBE 101	7.1	217	271	5.2	59	207
CMBE 102	5.9	251	327	4.7	82	239
RMBE 1154	0.9	403	677	0.4	273	121
RMBE 1155	1.1	376	799	0.5	300	164
RMBE 1156	1.3	94	313	2.2	29	19
RMBE 1172	1.1	176	518	0.9	91	51
RMBE 1173	1.0	164	464	1.1	76	45
RMBE 1174	0.8	156	436	1.2	68	31
RMBE 1175	0.6	84	175	2.2	15	5
RMBE 1181	0.3	53	77	1.5	4	1
RMBE 1182	0.6	61	68	1.3	4	1
RMBE 1198	0.8	56	64	2.7	4	1
RMBE 1199						
RMBE 1200	0.7	44	58	3.8	3	1

Table D.II. Mounds statistics for the InAs/AlGaAs and AlGaAs samples.

D.1.3 Morphology identifiers

Sample n.	Morphology identifier
CMBE 73	0.4° mounds
CMBE 74	4.8° mounds
CMBE 75	4° mounds
CMBE 80	InAs QDS on 5.2° mounds
CMBE 81	InAs QDs on 3.3° mounds
CMBE 87	InAs QDs on 3.1° mounds
CMBE 88	2.5° mounds
CMBE 90	InAs QDs on flat surface
CMBE 91	InAs QDs on flat surface
CMBE 98	2.9° mounds
CMBE 99	1.7° mounds
CMBE 101	5.2° mounds
CMBE 102	4.7° mounds
RMBE 1154	0.4° mounds
RMBE 1155	0.5° mounds
RMBE 1156	2.2° mounds
RMBE 1172	0.9° mounds
RMBE 1173	1.1° mounds
RMBE 1174	1.2° mounds
RMBE 1175	2.2° mounds
RMBE 1181	1.5° mounds
RMBE 1182	1.3° mounds
RMBE 1198	2.7° mounds
RMBE 1199	Flat surface
RMBE 1200	3.8° mounds

Table D.III. Table of morphology identifiers for InAs/AlGaAs and AlGaAs samples.

D.2 ITO, hyper-eutectic ITO, and eutectic InSn on sapphire PLD samples

D.2.1 ITO PLD samples

Sample n.	Laser energy mJ	Laser spot size cm^2	Laser fluence J/cm^2	Substrate temperature °C	N_2 pressure mTorr	Pulse frequency Hz	Number of pulses 10^3
NPLD-16-06-14-S-ITO	81	0.07	1.16	550	740	10	12
NPLD-16-06-15-S-ITO	81	0.13	0.62	550	356	10	12
NPLD-16-06-16-S-ITO	80	0.13	0.62	550	75.4	10	12
NPLD-16-06-20-S-ITO	80	0.13	0.62	550	201	10	12
NPLD-16-06-21-S-ITO	80	0.13	0.62	550	7.2	10	12
NPLD-16-06-27-S-ITO	29	0.046	0.63	550	76.1	5	12
NPLD-16-06-30-S-ITO	29	0.046	0.63	550	76.9	2.5	12
NPLD-16-07-06-S-ITO	46	0.046	1.00	550	76.6	2.5	12
NPLD-16-07-11-S-ITO	46	0.046	1.00	550	7.57	2.5	12
NPLD-16-07-14-S-ITO	46	0.12	0.38	600	76.5	2.5	12
NPLD-16-07-19-S-ITO	55	0.055	1.00	600	75.8	2.5	12
NPLD-16-07-20-S-ITO	55	0.055	1.00	550	77.3	2.5	12
NPLD-16-07-21-S-ITO	55	0.055	1.00	550	76.6	2.5	12
NPLD-16-07-26-S-ITO	54	0.055	0.98	550	7.9	2.5	12
NPLD-16-07-28-S-ITO	61	0.029	2.10	550	0.78	2.5	12
NPLD-16-07-31-S-ITO	40	0.04	1.00	550	77.3	2.5	12
NPLD-16-08-02-S-ITO	63	0.096	0.66	550	77	2.5	12
NPLD-16-08-05-S-ITO	30	0.051	0.59	550	77	2.5	12
NPLD-16-08-08-S-ITO	35	0.068	0.51	550	76.8	2.5	24
NPLD-17-10-20a-S-ITO	114			550	78.8	2.5	12
NPLD-17-10-20b-S-ITO	99			550	76.9	2.5	12
NPLD-17-10-20c-S-ITO	84			550	67.6	2.5	12
NPLD-17-10-20d-S-ITO	69			550	57.4	2.5	12
NPLD-17-10-20e-S-ITO	54			550	47.7	2.5	12
NPLD-17-10-26a(1,2)-S-ITO	114	0.112	1.01	550	77.1	2.5	12
NPLD-17-10-26b(1,2)-S-ITO	114			550	67.2	2.5	12
NPLD-17-10-26c2-S-ITO	114			550	57	2.5	12
NPLD-17-10-26d(1,2)-S-ITO	114			550	47.2	2.5	12
NPLD-19-04-28a-(l,r)-S-ITO	55	0.098	0.56	550	77	2.5	12
NPLD-19-04-28b-(l,r)-S-ITO	54	0.09	0.60	550	77	2.5	12
NPLD-19-04-29a-(l,r)-S-ITO	55	0.07	0.79	550	77	2.5	12

Table D.IV. Growth parameters for the PLD of ITO layers.

D.2.2 ITO PLD samples morphology identifiers

Sample n.	Morphology identifier
NPLD-16-06-14-S-ITO	VS film
NPLD-16-06-15-S-ITO	VS film
NPLD-16-06-16-S-ITO	Tapered VLS + VS NW
NPLD-16-06-20-S-ITO	VS film
NPLD-16-06-21-S-ITO	Tapered VLS + VS NW
NPLD-16-06-27-S-ITO	VLS NW
NPLD-16-06-30-S-ITO	VLS NW
NPLD-16-07-06-S-ITO	VLS NW
NPLD-16-07-11-S-ITO	Sparse NW, lenticular nanostructures
NPLD-16-07-14-S-ITO	VLS NW
NPLD-16-07-19-S-ITO	VS film
NPLD-16-07-20-S-ITO	VS film
NPLD-16-07-21-S-ITO	VS film
NPLD-16-07-26-S-ITO	VS film
NPLD-16-07-28-S-ITO	VS film
NPLD-16-07-31-S-ITO	VS film, rare VLS + VS NW
NPLD-16-08-02-S-ITO	VLS NW
NPLD-16-08-05-S-ITO	VLS NW
NPLD-16-08-08-S-ITO	VLS NW
NPLD-17-10-20a-S-ITO	VS film, rare VLS + VS NW
NPLD-17-10-20b-S-ITO	VLS NW
NPLD-17-10-20c-S-ITO	VLS NW
NPLD-17-10-20d-S-ITO	VLS NW
NPLD-17-10-20e-S-ITO	Branched VLS NW
NPLD-17-10-26a(1,2)-S-ITO	Branched VLS NW
NPLD-17-10-26b(1,2)-S-ITO	Branched VLS NW
NPLD-17-10-26c2-S-ITO	Branched VLS NW
NPLD-17-10-26d(1,2)-S-ITO	Branched VLS NW
NPLD-19-04-28a-(l,r)-S-ITO	VLS NW
NPLD-19-04-28b-(l,r)-S-ITO	VLS NW

Table D.V. Table of morphology identifiers for the ITO layers.

D.2.3 Hyper-eutectoid ITO PLD samples

Sample n.	Laser energy	Laser spot size	Laser fluence	Substrate temperature	N_2 pressure	Shot frequency	Number of pulses
	mJ	cm^2	J/cm^2	°C	mTorr	Hz	
NPLD-16-08-09-S-heITO	40	0.068	0.58	550	78	2.5	12000
NPLD-16-08-14-S-heITO	38	0.07	0.54	550	78	1.3	12000
NPLD-16-09-08-S-heITO	36	0.051	0.71	500	78	2.5	12000
NPLD-16-09-17-S-heITO	46	0.075	0.61	600	77	2.5	12000
NPLD-16-10-02-a-S-heITO	47	0.075	0.63	600	80	2.5	10
NPLD-16-10-02-b-S-heITO	47	0.075	0.63	600	80	2.5	100
NPLD-16-10-02-c-S-heITO	47	0.075	0.63	600	80	2.5	1000
NPLD-16-10-20-S-heITO	71	0.11	0.64	600	78	1	12000
NPLD-16-10-28-a-S-heITO	24	0.043	0.56	600	79	1	1
NPLD-16-10-28-b-S-heITO	24	0.043	0.56	600	79	2.5	100
NPLD-16-10-28-c-S-heITO	24	0.043	0.56	600	80	2.5	5000
NPLD-16-11-20-a-S-heITO	61	0.069	0.88	550	78	1.3	12000
NPLD-16-11-20-b-S-heITO	56	0.069	0.81	550	78	2.5	12000
NPLD-16-12-10-S-heITO	63	0.069	0.92	550	78	2.5	24000
NPLD-16-12-17-S-heITO	61	0.067	0.91	550	78	1.3	24000
NPLD-17-01-11-a-S-heITO	71	0.062	1.14	550	8	2.5	12000
NPLD-17-01-11-b-S-heITO	71	0.062	1.14	550	8	1.3	12000
NPLD-17-01-30-a-S-heITO	97	0.04	2.42	600	78	2.5	24000
NPLD-17-01-30-b-S-heITO	201	0.059	3.41	450	8	2.5	12000
NPLD-17-01-31-S-heITO	77	0.099	0.78	550	78	2.5	24000

Table D.VI. Growth parameters for the PLD of hyper-eutectoid ITO layers.

D.2.4 Eutectic InSn PLD samples

Sample	Laser energy	Laser spot size	Laser fluence	Process gas	Substrate temperature	Deposition pressure		Pulse frequency	Number of pulses
	mJ	cm^2	J/cm^2		°C	Torr	mTorr	Hz	
NPLD-17-04-30a-S-eInSn	154	0.048	3.21	-	500	1.50E-05		10	1
NPLD-17-04-30a-Si-eInSn	154	0.048	3.21	-	500	1.50E-05		10	1
NPLD-17-04-30b-S-eInSn	154	0.048	3.21	-	500	6.30E-06		10	10
NPLD-17-04-30c-S-eInSn	154	0.048	3.21	-	500	6.30E-06		10	100
NPLD-17-04-30c-Si-eInSn	154	0.048	3.21	-	500	6.30E-06		10	100
NPLD-17-05-27a-S-eInSn	154	0.05	3.08	O_2	500		1.03	10	12000
NPLD-17-05-27b-S-eInSn	154	0.05	3.08	O_2	500		10.2	10	12000
NPLD-17-05-27c-S-eInSn	154	0.05	3.08	O_2	500		100	10	12000
NPLD-17-06-15a-S-eInSn	154	0.05	3.08	O_2	500		0.5	10	12000
NPLD-17-06-15b-S-eInSn	154	0.05	3.08	O_2	500		0.11	10	12000
NPLD-17-06-16a-S-eInSn	154	0.05	3.08	O_2	500		1.05	2.5	12000
NPLD-17-06-16b-S-eInSn	154	0.05	3.08	O_2	500		1.05	5	12000
NPLD-17-07-29-S-eInSn	154	0.06	2.57	O_2	450		1.01	10	12000
NPLD-17-07-30a-S-eInSn	154	0.06	2.56	O_2	400		1.03	10	12000
NPLD-17-07-30b-S-eInSn	144	0.05	2.88	O_2	350		1.04	10	12000
NPLD-17-07-31a-S-eInSn	154	0.05	3.07	O_2	500		1.08	5	12000
NPLD-17-07-31b-S-eInSn	145	0.04	3.63	O_2	500		1.07	2.5	12000
NPLD-17-07-31c-S-eInSn	137	0.04	3.42	O_2	500		1.08	1.3	12000
NPLD-18-11-16a-S-eInSn	154	0.05	3.08	O_2	500		0.36	10	12000
NPLD-18-11-16b-S-eInSn	153	0.05	3.06	O_2	450		0.45	10	12000
NPLD-18-11-16c-S-eInSn	152	0.05	3.03	O_2	475		0.42	10	12000
NPLD-18-11-16d-S-eInSn	151	0.05	3.01	O_2	488		0.59	10	12000

Table D.VII. Growth parameters for the reactive PLD of eutectic InSn.